



OKLAHOMA TRANSPORTATION CENTER

ECONOMIC ENHANCEMENT THROUGH INFRASTRUCTURE STEWARDSHIP

RELIEF OF REINFORCING CONGESTION IN BEAMS AND BENT CAPS OF CONCRETE BRIDGES

THOMAS H.-K. KANG, PH.D., P.E.
WOOSUK KIM, PH.D.
KAH MUN LAM
RANDY D. MARTIN
KYU KIM
YU HUANG, PH.D.
LISA HOLLIDAY, PH.D., P.E.

OTCREOS9.1-27-F

Oklahoma Transportation Center
2601 Liberty Parkway, Suite 110
Midwest City, Oklahoma 73110

Phone: 405.732.6580
Fax: 405.732.6586
www.oktc.org

DISCLAIMER

The contents of this report reflect the views of the authors, who are responsible for the facts and accuracy of the information presented herein. This document is disseminated under the sponsorship of the Department of Transportation University Transportation Centers Program, in the interest of information exchange. The U.S. Government assumes no liability for the contents or use thereof.

TECHNICAL REPORT DOCUMENTATION PAGE

1. REPORT NO. OTCREOS9.1-27-F	2. GOVERNMENT ACCESSION NO.	3. RECIPIENTS CATALOG NO.	
4. TITLE AND SUBTITLE Relief of Reinforcing Congestion in Beams and Bent Caps of Concrete Bridges		5. REPORT DATE June 30, 2012	
		6. PERFORMING ORGANIZATION CODE	
7. AUTHOR(S) Thomas H.-K. Kang, Woosuk Kim, Kah Mun Lam, Randy D. Martin, Kyu Kim, Yu Huang, Lisa Holliday		8. PERFORMING ORGANIZATION REPORT	
9. PERFORMING ORGANIZATION NAME AND ADDRESS The University of Oklahoma School of Civil Engineering & Environmental Science 202 W. Boyd St. Rm 334, Norman, OK 73019		10. WORK UNIT NO.	
		11. CONTRACT OR GRANT NO. DTRT06-G-0016	
12. SPONSORING AGENCY NAME AND ADDRESS Oklahoma Transportation Center (Fiscal) 201 ATRC Stillwater, OK 74078 (Technical) 2601 Liberty Parkway, Suite 110, Midwest City, OK 73110		13. TYPE OF REPORT AND PERIOD COVERED Final Report: June. 2009 - June 2012	
		14. SPONSORING AGENCY CODE	
15. SUPPLEMENTARY NOTES University Transportation Center			
16. ABSTRACT <p>In order to determine how to resolve the issues involving steel congestion in reinforced concrete (RC) structures, three potential solutions to this problem were researched. In the first method, reinforced concrete (RC) was mixed with steel fibers. The use of steel fibers instead of shear reinforcement stirrups resulted in the reduction of steel congestion in a manner which was both effective in reducing the effects of congestion and which was practical to implement. In the second method, steel congestion in reinforced concrete (RC) was effectively reduced by the use of self-consolidating concrete (SCC), which does not require the use of vibrators in its casting. In the final method, steel congestion was effectively reduced by the use of headed bars instead of traditional hooked bars. This first and third approach is emerging as a research topic of special interest in the American Concrete Institute.</p> <p>In evaluating these three approaches, and in combining them in this study, varied types of concrete were used. Shear testing was conducted using a lightweight concrete mix. Flexural testing of lightweight prestressed concrete (PC) beams was conducted using self-consolidating concrete (SCC). Seismic testing of headed bars in RC beam-column connections was conducted using a normal weight concrete mix. These three experiments were the subject matter of this study. In these studies the experimental results were compared with the ACI 318-08 provisions and with existing modeling equations proposed by many researchers. New models were proposed which better correlated with the test results were proposed.</p> <p>Therefore, although other studies in the world may have dealt with the relief of steel congestion in RC and/or PC structures, in researching these three unique methods for the relief of steel congestion it was discovered that several variations and combinations of such methods can provide effective solutions for diverse conditions. Most of all, this study should prove important in providing the basis for additional research since the guidelines and codes regarding the relief of steel congestion are shown to be based upon previously limited data.</p>			
17. KEY WORDS Self-consolidating, concrete, steel fibers, prestressed		18. DISTRIBUTION STATEMENT No restrictions. This publication is available at www.oktc.org and at the NTIS: National Technical Information Service Springfield, Virginia 22161 http://www.ntis.gov	
19. SECURITY CLASSIF. (OF THIS REPORT) Unclassified	20. SECURITY CLASSIF. (OF THIS PAGE) Unclassified	21. NO. OF PAGES 158 + covers	22. PRICE

SI (METRIC) CONVERSION FACTORS

Approximate Conversions to SI Units				
Symbol	When you know	Multiply by	To Find	Symbol
LENGTH				
in	inches	25.40	millimeters	mm
ft	feet	0.3048	meters	m
yd	yards	0.9144	meters	m
mi	miles	1.609	kilometers	km
AREA				
in ²	square inches	645.2	square millimeters	mm ²
ft ²	square feet	0.0929	square meters	m ²
yd ²	square yards	0.8361	square meters	m ²
ac	acres	0.4047	hectares	ha
mi ²	square miles	2.590	square kilometers	km ²
VOLUME				
fl oz	fluid ounces	29.57	milliliters	mL
gal	gallons	3.785	liters	L
ft ³	cubic feet	0.0283	cubic meters	m ³
yd ³	cubic yards	0.7645	cubic meters	m ³
MASS				
oz	ounces	28.35	grams	g
lb	pounds	0.4536	kilograms	kg
T	short tons (2000 lb)	0.907	megagrams	Mg
TEMPERATURE (exact)				
°F	degrees Fahrenheit	(°F-32)/1.8	degrees Celsius	°C
FORCE and PRESSURE or STRESS				
lbf	poundforce	4.448	Newtons	N
lbf/in ²	poundforce per square inch	6.895	kilopascals	kPa

Approximate Conversions from SI Units				
Symbol	When you know	Multiply by	To Find	Symbol
LENGTH				
mm	millimeters	0.0394	inches	in
m	meters	3.281	feet	ft
m	meters	1.094	yards	yd
km	kilometers	0.6214	miles	mi
AREA				
mm ²	square millimeters	0.00155	square inches	in ²
m ²	square meters	10.764	square feet	ft ²
m ²	square meters	1.196	square yards	yd ²
ha	hectares	2.471	acres	ac
km ²	square kilometers	0.3861	square miles	mi ²
VOLUME				
mL	milliliters	0.0338	fluid ounces	fl oz
L	liters	0.2642	gallons	gal
m ³	cubic meters	35.315	cubic feet	ft ³
m ³	cubic meters	1.308	cubic yards	yd ³
MASS				
g	grams	0.0353	ounces	oz
kg	kilograms	2.205	pounds	lb
Mg	megagrams	1.1023	short tons (2000 lb)	T
TEMPERATURE (exact)				
°C	degrees Celsius	9/5+32	degrees Fahrenheit	°F
FORCE and PRESSURE or STRESS				
N	Newtons	0.2248	poundforce	lbf
kPa	kilopascals	0.1450	poundforce per square inch	lbf/in ²

ACKNOWLEDGMENTS

The authors would like to express their appreciation to the following REU students and collaborators, who assisted the execution of the laboratory work and/or data analysis.

John Paul Badasci, Undergraduate student from Austin Peay State University;

Saagar Patel, Undergraduate student from Illinois Institute of Technology;

Michael Van Zandt, Undergraduate student from The University of Oklahoma;

Jean-Luc D'Abreau, Undergraduate student from California Poly State University at San Luis Obispo;

Jenny Bergen, Undergraduate student from The University of Oklahoma;

Kate Turner, Undergraduate student from Massachusetts Institute of Technology;

Sung-Gul Hong, Ph.D., Professor at Seoul National University;

Yeun-Keun Kwak, Ph.D., Professor at Kumoh National Institute of Technology;

Myoungsu Shin, Ph.D., Assistant Professor at Ulsan National Institute of Science & Technology;

Chris Ramseyer, Ph.D., Assistant Professor at The University of Oklahoma.

RELIEF OF REINFORCING CONGESTION IN BEAMS AND BENT CAPS OF CONCRETE BRIDGES

Final Report

June, 2012

Thomas H.-K. Kang, Ph.D., P.E.

**Assistant Professor, Department of Architecture & Architectural Engineering,
Seoul National University, Korea**

and

**Adjunct Professor, School of Civil Engineering & Environmental Science,
The University of Oklahoma**

Woosuk Kim, Ph.D., Kah Mun Lam, Randy D. Martin, Kyu Kim, Yu Huang, Ph.D.

**Research Assistants, School of Civil Engineering & Environmental Science,
The University of Oklahoma**

Lisa Holliday, Ph.D., P.E.

**Assistant Professor, Division of Construction Science
The University of Oklahoma**

**Oklahoma Transportation Center
2601 Liberty Parkway, Suite 110
Midwest City, OK 73110**

TABLE OF CONTENTS

1. INTRODUCTION	1
1.1 BACKGROUND	1
1.2 GOAL AND NEED FOR THIS STUDY.....	4
2. LITERATURE REVIEW	5
2.1 STEEL FIBERS IN REINFORCED LIGHTWEIGHT CONCRETE BEAMS	5
2.1.1 Part I: Review of Previous Experimental Research for Large-Scale Structural Testing.....	8
2.1.2 Part II: Review of Previous Experimental Research for Small-Scale Material Testing	9
2.2 REINFORCED CONCRETE BEAM-COLUMN CONNECTIONS WITH HEADED BARS.....	12
2.2.1 Part I: Summary of ACI Standards and Recommendations.....	12
2.2.2 Part II: Summary of Experimental Research.....	19
3. HYPOTHESES AND OBJECTIVES.....	23
4. LARGE SCALE TESTING AND ANALYSIS OF STEEL FIBER-REINFORCED LIGHTWEIGHT CONCRETE BEAMS	27
4.1 INTRODUCTION	27
4.2 EXPERIMENTAL PROGRAM.....	28
4.2.1 Design of Test Specimens	28
4.2.2 Material Properties.....	33
4.2.3 Testing and Instrumentation	40
4.3 OBSERVATIONS AND TEST RESULTS	40
4.3.1 Crack Patterns and Failure Modes	40
4.3.2 Load-Deflection Relations and Strain Gauge Measurements	45

4.3.3	Effects of Steel Fiber Volume Fraction and Shear Span-to-Depth Ratio	52
4.4	DESIGN SHEAR STRENGTH OF SFRLC BEAMS WITHOUT STIRRUPS	55
4.5	SUMMARY.....	69
5.	LARGE SCALE TESTING AND ANALYSIS OF PRESTRESSED SELF-CONSOLIDATING CONCRETE BEAMS.....	71
5.1	INTRODUCTION	71
5.2	EXPERIMENTAL PROGRAM AND RESULTS.....	72
5.2.1	Test Specimen Design.....	72
5.2.2	Material and Mixture Properties.....	75
5.2.3	Fabrication of Test Specimens	86
5.2.4	Testing, Test Setup and Instrumentation	87
5.2.5	Observations and Overall Test Results.....	89
5.3	COMPARISON WITH NUMERICAL ANALYSIS RESULTS	93
5.3.1	Comparison between Numerical and Experimental Results	95
5.4	SUMMARY.....	99
6.	LARGE SCALE TESTING AND ANALYSIS OF REINFORCED CONCRETE CONNECTIONS WITH HEADED BARS UNDER SEISMIC LOADS	101
6.1	INTRODUCTION	101
6.2	EXPERIMENTAL PROGRAM.....	101
6.2.1	Design of Test Specimens	101
6.2.2	Construction and Material Properties.....	109
6.2.3	Test Setup and Loading Sequence.....	115
6.3	ANALYSIS OF TEST RESULTS.....	118
6.3.1	Load-Displacement Response.....	118
6.3.2	Beam Plastic Hinge Development	124

6.3.3 Limited Joint Shear Deformation.....	129
6.3.4 Performance Evaluation per ACI 374.1-05	130
6.4 SUMMARY.....	134
7. CONCLUSION.....	137
REFERENCES.....	139

LIST OF FIGURES

Figure 1.1.	L-Joint of Bent Cap of I-35 Overpass in Oklahoma City, OK and T-Joint of I-35 Substructure.....	2
Figure 1.2.	Collapse Due to Outrigger Knee Joint Failure during 1989 Loma Prieta Earthquake (Wikipedia, fn. USGS)	3
Figure 2.1.	Modulus of Rupture Test (per ASTM C1609) of Concrete Prisms.....	6
Figure 2.2.	Compressive Strength Tests of SFRLC Cylinders per ASTM C496, with Two Strain Gauges Attached to Measure STRAINS	7
Figure 2.3.	Schematic of Shear Specimens (Adapted from Balaguru and Dipsia [12]).....	7
Figure 2.4.	Elevation and Section of Test Beam (Adapted from Swamy et al. [10]; Conversion: 1 mm = 0.039 in.).....	9
Figure 2.5.	Details of Test Slab Specimen (Adapted from Theodorakopoulos and Swamy [11]; Conversion: 1 mm = 0.039 in.).....	9
Figure 2.6.	Flexural Toughness Test Setup	11
Figure 2.7.	Direct Shear Test Setup (Adapted from Higashiyama and Banthia [15]).....	11
Figure 2.8.	Headed Deformed Reinforcing Bar Requirements for Bearing of Deformation (Reproduced; ACI 318-08 [17])	13
Figure 2.9.	Failure Modes for Headed Anchors (Reproduced; ACI 318-08 [17]).....	14
Figure 2.10.	Shallow Embedment Pullout Test Setup	15
Figure 2.11.	Comparison of Embedment Depth h_d and Bonded Length l_b in Concrete (Adapted from DeVries et al. [19]).....	16
Figure 2.12.	Edge Distance and Head Parameters (Adapted from DeVries et al. [19]).....	16
Figure 2.13.	Pullout Cone Failure.....	17
Figure 2.14.	Schematic of Test Specimen and Setup	17
Figure 2.15.	Location of Headed and Hooked Bars (Reproduced from ACI 352-02 [23]).....	18
Figure 2.16.	Schematic Diagrams of Investigated Beam-Column Connections	20

Figure 3.1.	Potential Solutions to Relieving Steel Congestion in Concrete Structures	23
Figure 3.2.	Headed Bars, Steel Fibers, and Self-Consolidating Concrete.....	25
Figure 4.1.	Test Setup and Test Beams (Conversion: 1 mm = 0.039 in.).....	31
Figure 4.2.	Concrete Compressive Stress-Strain Curve for All Specimens.....	38
Figure 4.3.	MOR Test.....	38
Figure 4.4.	Tensile Strength Testing of Longitudinal Deformed Bar.....	39
Figure 4.5.	Details for Hooked Steel Fibers Used In This Study and Various Steel Fibers Shapes (Conversion: 1 Mm = 0.039 In.)	39
Figure 4.6.	Schematics of Sequential Crack Patterns (Numbers along the Beam: Distance from The Mid-Span [Mm]; Numbers On The Beam: Load [Tons]; Conversion: 1 Ton = 9.8 Kn = 2.24 Kips).....	44
Figure 4.7.	Load-Deflection Relationships for SFRLC and SFRC	48
Figure 4.8.	Comparison of Load-Deflection Relationships between SFRC and SFRLC with $V_f = 0.5\%$ (Conversion: 1 Kn = 0.2248 Kips; 1 Mm = 0.039 In.).....	48
Figure 4.9.	Load-Bar Strain Relationship for SFRLC and SFRC.....	50
Figure 4.10.	Comparison of Load-Bar Strain Relationships	51
Figure 4.11.	Measured Shear Strengths versus Shear Span-to-Depth Ratio (A/D)	53
Figure 4.12.	Measured Moment at Peak versus Steel Fiber Volume Fraction (V_f).....	53
Figure 4.13.	Measured Shear Strength (v_u) / Calculated Shear Strength (v_n) versus Main Parameters (Conversion: 1 MPa = 145 psi; 1 mm = 0.039 in.)	68
Figure 5.1.	Details of Prestressed SCC Member Sections (Conversion: 1 mm = 0.039 in.).....	74
Figure 5.2.	Elevations of the Prestressed Members (Conversion: 1 mm = 0.039 in.).....	75
Figure 5.3.	Slump Flow Test	76
Figure 5.4.	Concrete Stress-Strain Curves for $R1$ and $I1$ (Conversion: 1 MPa = 145 psi).....	79
Figure 5.5.	Concrete Compressive Stress-Strain Curves for $R2$ and $I2$	80

Figure 5.6.	Tensile Normal Stress at Mid-Span Bottom versus Prism Displacement Relationships for <i>R1</i> and <i>I1</i>	81
Figure 5.7.	Tensile Normal Stress at the Mid-Span Bottom versus Prism Displacement Relationships for <i>R2</i> and <i>I2</i>	83
Figure 5.8.	Stress-Strain Relationships for Longitudinal Deformed Bars.....	84
Figure 5.9.	Stress-Strain Relationships for Prestressing Steel Strands.....	85
Figure 5.10.	Prestressing of 13 mm (½ in.) Diameter Low Relaxation Strands with a Hydraulic Jack at CORESLAB Structures, Inc., Oklahoma City, Oklahoma	87
Figure 5.11.	Test Setup at the Donald G. Fears Engineering Laboratory in OU	89
Figure 5.12.	Beam Failures and Cracking Patterns at Mid-Span	92
Figure 5.13.	Load-Deflection at Mid-Span Relationship	93
Figure 5.14.	Load-Deflection at Mid-Span Relationship between Experimental and Numerical Results (Conversion: 1 kN = 0.2248 kips; 1 mm = 0.039 in.)..	99
Figure 6.1.	Dimensions and Details for JH-R1 & JH-R2 (Conversion: 1 mm = 0.039 in.).....	103
Figure 6.2.	Heads and Threaded Connections (Conversion: 1 mm = 0.039 in.).....	104
Figure 6.3.	Progress of Fabricating Specimens	110
Figure 6.4.	Stress vs. Strain Curve for Concrete Compressive Strength Tests.....	112
Figure 6.5.	Tensile Normal Stress at Mid-Span Bottom versus Displacement Relationship for MOR Tests.....	113
Figure 6.6.	Stress-Strain Relationship for D19 (No. 6) Longitudinal Deformed Bars (Conversion: 1MPa = 145 psi)	114
Figure 6.7.	Test Setup and Dimensions for Instrumentation	116
Figure 6.8.	Overview of JH-R2 Test Specimen and Setup	117
Figure 6.9.	Loading History	117
Figure 6.10.	Moment vs. Drift Ratio Relationships for JH-R1	121
Figure 6.11.	Moment vs. Drift Ratio Relationships for JH-R2	123
Figure 6.12.	Backbone Envelopes of Lateral Load-Drift Relations	123
Figure 6.13.	Beam Moment vs. Beam Rotation Relationships for JH-R1 and JH-R2 Specimens (Conversion: 1 mm = 0.039 in.).....	127

Figure 6.14. Normalized Joint Shear vs. Joint Shear Distortion Relationships..... 128
Figure 6.15. Crack Patterns at the End of Seismic Testing 134

LIST OF TABLES

Table 4.1.	Descriptions of Test Specimens	32
Table 4.2.	Relations between Steel Fiber Dosage Rate and Volume Fraction (V_f)	33
Table 4.3.	Physical Characteristics of Type I Portland Cement.....	34
Table 4.4.	Physical Properties of Coarse and Fine Aggregates	34
Table 4.5.	Chemical Compositions of Expanded Clay Aggregate	35
Table 4.6.	Physical Properties of High-Range Water Reducing Admixture	35
Table 4.7.	Physical Characteristics of SFRLC and SFRC Mixtures.....	35
Table 4.8.	Measured Material Properties of SFRLC and SFRC	37
Table 4.9.	Physical Properties of Flexural Reinforcing Bars.....	37
Table 4.10.	Physical Properties of Steel Fiber	37
Table 4.11.	Test Results and Failure Modes of Specimens	42
Table 4.12.	Comparisons of Measured Peak Shear Strengths and Shear Strength Capacities Calculated Based on The Available SFRC Shear Strength Models Except for the Replacement of f'_c by $\lambda^2 f'_c$ for SFRLC Beams	63
Table 4.13.	Steepness (Slope) of the Linear Regression Line for the Ratio of Measured Peak Shear Strength (v_u) to Calculated Shear Strength (v_n), with the Consideration of Lightweight Concrete Factor ($\lambda =$ 0.75).....	66
Table 5.1.	SCC Mixture Proportions.....	77
Table 5.2.	Fresh and Hardened Concrete Properties for SCC Mixtures.....	78
Table 5.3.	Experimental Results of Prestressed SCC Members	90
Table 5.4.	Material Parameters Used 2D Modeling.....	94
Table 5.5.	Summary of Experimental and Numerical Simulation Results.....	96
Table 6.1.	Dimensions for Heads and Headed Bars	104
Table 6.2.	Connection Design Parameters.....	106
Table 6.3.	Provided and Required Development Lengths for Headed Beam Bars Used for Connection Subassemblies	108

Table 6.4.	Fresh and Hardened Concrete Properties.....	111
Table 6.5.	Measured steel Material Properties.....	111
Table 6.6.	Instrumentation List.....	118
Table 6.7.	Summary of Seismic Test Results of Moment and Drift.....	124
Table 6.8.	Comparisons between Test Results and ACI 374.1-05 Acceptance Criteria.....	132
Table 6.9.	Comparison of Maximum Joint Shear Demands and Nominal Joint Shear Strengths.....	133

EXECUTIVE SUMMARY

The authors aimed to conduct research into methods of reducing steel congestion of reinforced and prestressed concrete infrastructures without affecting overall strength. The first aspect of the research focused on relief of reinforcing congestion by utilizing headed bars. Closely spaced headed bars (with clear bar spacing less than $4d_b$) are not permitted by the current ACI 318-08 provisions. This research results can be used to assist updating ACI 318 provisions and 352 recommendations. The second aspect of the investigations involved use of self-consolidating concrete and steel fibers for reinforced and prestressed concrete members to relieve steel congestion. The project helped determine a better minimum steel fiber volume ratio resulting in a mix that is both workable and durable. The current ACI 318-08 minimum ratio has been deemed unsatisfactory by practical engineers. The research required specialized equipment, personnel, and facilities to conduct large-scale monotonic and reversed cyclic testing. In this project, a number of large-scale beams, girders, and cap beam-bridge column joints were tested. Analytical investigations were also performed to help evaluate behavior of steel fiber-reinforced concrete and self-consolidating concrete. Overall, this project attempted to address one of the major concerns of OTC and ODOT: congestion due to reinforcing details. Some bridge reinforcing details (e.g., joint region or overlay bridge deck where adequate shear resistance is also necessary) have not been produced within the tolerance limits in the field or have caused problems with concrete placement and quality. Requirements for bar anchorage and development have been frequently neglected in actual construction simply because there was no space for re-bars at the joint and connection region. The current minimum required dosage rate of steel fibers (ACI 318-08, §5.6.6.2) might cause even more concrete workability problems, which in fact would not help in concrete placement. The results and outcomes of this project will impact the quality control of cast-in-place bridge construction. More specifically, the optimal use of steel fibers and headed bars corresponding to well-detailed guidelines that can be developed based on the proposed research will improve all new bridge construction and rehabilitation projects in the nation

1. INTRODUCTION

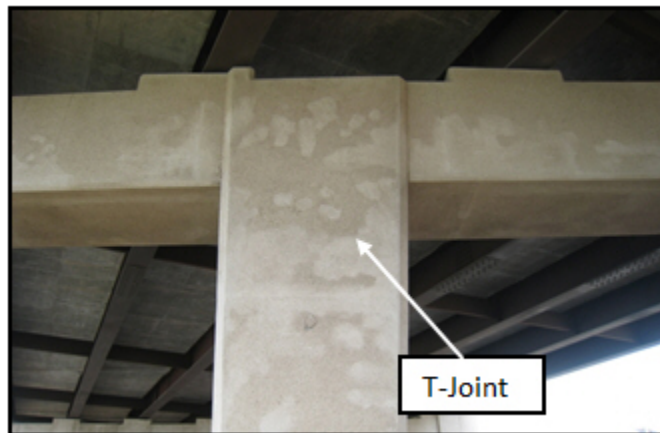
1.1 BACKGROUND

Over the last half-century, the reinforced and prestressed concrete structure industry has struggled with problems associated with reinforcement congestion and a lack of bar anchorage space. Continuous design code changes to accommodate resistance to heavy traffic (e.g., moving truck loads) or extreme hazards (such as earthquake actions) led to the increased use of large diameter reinforcing bars (e.g., D32, D36 or D43 [No. 10, 11 or 14]) for reinforced and prestressed concrete structures. As the size of the reinforcement increased, its development length also increased, intensifying the congestion problem.

It is well known that required development length is a function of the bar diameter. As such, the use of 90-degree standard hooks has been inevitable to ensure sufficient development length at the region where large diameter reinforcing bars terminate (Figure 1.1). It is recognized that straight bar termination with insufficient embedment from the critical section is extremely dangerous. Anchorage failure does not only preclude the development of the design moments and shear forces of the members, but also may result in catastrophic collapse due to the lack of structural integrity (Figure 1.2). This also can happen in the case of hooked bar anchorage as a result of misdetermination of the required development length of reinforcement. It is generally required either that the depth of the bent cap be greater than that needed to fully develop the yield stress of straight column longitudinal reinforcement, or that hooked bars with sufficient development length be used. Similar requirements should apply to bent beam bars (Thompson et al. [1]) or at bridge pier-footing joints (Lehman et al. [2]). This important issue has been overlooked so that the bent cap joint or pier-foundation joint lacked room for large-diameter hooked bars.



(a) L-joint of Bent Cap of I-35 Overpass in Oklahoma City, OK



(b) T-Joint of I-35 Substructure

Figure 1.1. L-Joint of Bent Cap of I-35 Overpass in Oklahoma City, OK and T-Joint of I-35 Substructure



Figure 1.2. Collapse Due to Outrigger Knee Joint Failure during 1989 Loma Prieta Earthquake (Wikipedia, fn. USGS)

Past earthquakes have allowed researchers to identify the aforementioned problems. The collapse of an 18-span viaduct during the 1995 Kobe earthquake in Japan (Yashinsky and Karshenas [3]) was due to insufficient development length of the longitudinal welded bars. A number of knee joint shear failures, accelerated by improper bar development, occurred during the 1989 Loma Prieta earthquakes (Figure 1.2). Such designs have clearly proven inadequate, and must be prevented from recurring in future design and construction.

It is also essential to ensure the quality of cast-in-place concrete in steel-congested beam ends and beam-column connections such that the beams and connections of concrete structures are able to withstand natural and man-made hazards (e.g., earthquakes or blasts). As such, relief of reinforcing steel congestion without sacrificing structural performance is targeted this study.

1.2 GOAL AND NEED FOR THIS STUDY

The primary goals of this study are to experimentally investigate both existing and new means to achieve steel congestion relief without sacrificing structural performance and to analytically develop pertinent design guidelines through data analysis. Three methods toward relieving the potential steel congestion in reinforced and prestressed concrete structures are proposed: use of headed bars, use of steel fibers in conjunction with lightweight aggregates, and use of self-consolidating concrete (SCC). These materials are becoming preferred choices in recent cast-in-place and precast construction. A new code development effort regarding the performance of the concrete in conjunction with these materials has been initiated and is still in its infant stage. The current research will contribute to the code development.

This final report consists of seven chapters as follows:

- Chapter 1 is the introduction.
- Chapter 2 provides a review of previous literatures in the area.
- Chapter 3 presents the hypotheses and objectives of each study used.
- Chapter 4 shows the shear testing and analysis of steel fiber-reinforced lightweight concrete beams.
- Chapter 5 presents the experimental and analytical studies of prestressed self-consolidating concrete beams.
- Chapter 6 shows the seismic testing of exterior beam-column connections with closely-spaced headed bars.
- Chapter 7 provides the summary and conclusions of this study.

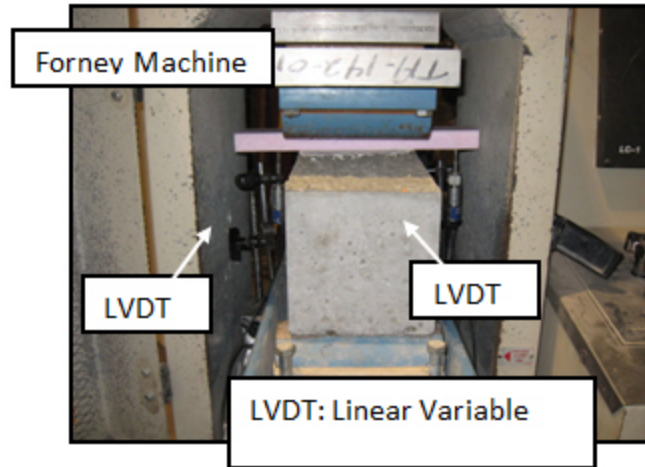
2. LITERATURE REVIEW

This chapter reviews the previous literature. Among several potential solutions to steel congestion in reinforced and prestressed concrete structures, this study examines three ways to achieve steel congestion relief: use of steel fiber-reinforced lightweight concrete (SFRLC), use of self-consolidating concrete (SCC), and use of headed bars. As there is little available research as to SCC, the literature review of SCC is excluded from this chapter. This literature review chapter focuses on the use of steel fibers in lightweight concrete beams and headed bars in reinforced concrete beam-column connections.

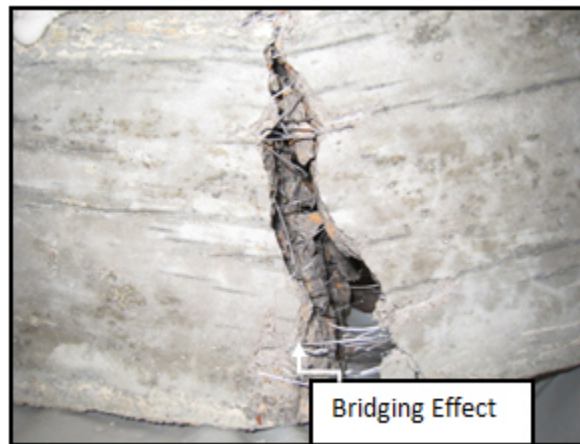
2.1 STEEL FIBERS IN REINFORCED LIGHTWEIGHT CONCRETE

BEAMS

To date, studies on the use of steel fibers in lightweight concrete have been sparse. Most previous tests of SFRLC materials were performed using $100 \times 100 \times 360$ mm ($4 \times 4 \times 14$ in., appx.) prisms, 150×300 mm (6×12 in.) cylinders, and/or small-scale shear specimens (e.g., $80 \times 80 \times 155$ mm; $3 \times 3 \times 6$ in.) (Balaguru et al. [4], [5], [6], Swamy and Jojagha [7], [8], Kayali et al. [9]) (refer to Figures 2.1 to 2.3). Only two large-scale structural testing programs of SFRLC members were previously undertaken, one by Swamy et al. [10] and the other by Theodorakopoulos and Swamy [11]. The following subsections provide a summary of prior experimental research on both large-scale structural testing and small-scale material testing of SFRLC.



(a) Before Test

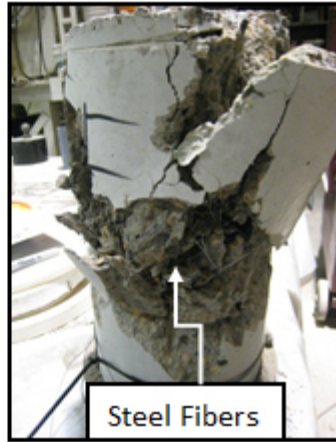


(b) After Test

Figure 2.1. Modulus of Rupture Test (per ASTM C1609) of Concrete Prisms (Using Forney Machine in Fears Lab at the University of Oklahoma [OU])

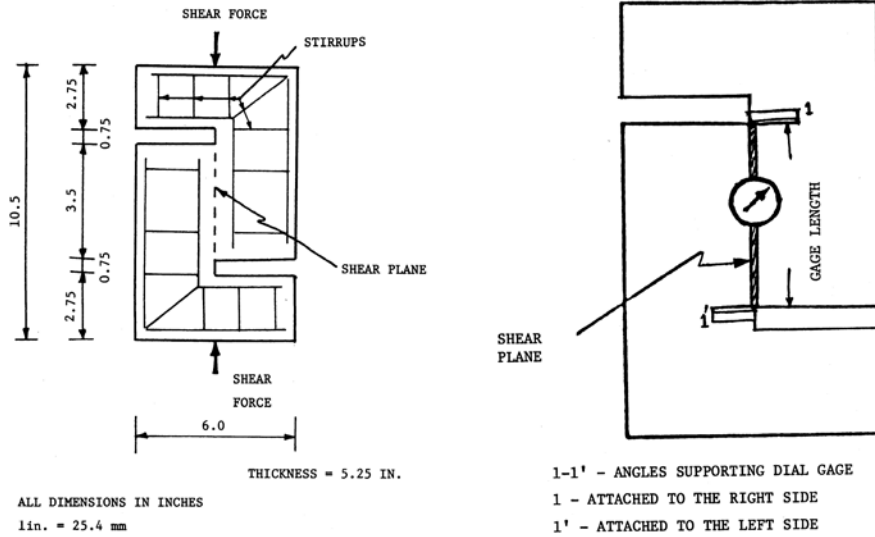


(a) Before test



(b) After test

Figure 2.2. Compressive Strength Tests of SFRLC Cylinders per ASTM C496, with Two Strain Gauges Attached to Measure STRAINS (Using Forney Machine in Fears Lab at the OU)



(a) Dimensions of Double-L Shear Specimen (b) Shear Specimens: Location of Dial Gauge

Figure 2.3. Schematic of Shear Specimens (Adapted from Balaguru and Dipsia [12])

2.1.1 Part I: Review of Previous Experimental Research for Large-Scale Structural Testing

Swamy et al. [10] tested eighteen large-scale specimens of SFRLC I-section beams with a span length of 3 m (118 in.) (Figure 2.4). The main variables studied were the shear span-to-depth ratio ($a/d = 2, 3.4, \text{ and } 4.9$), steel fiber volume fraction ($V_f = 0$ and 1%), and reinforcing ratio of bottom bars ($\rho = 1.6, 2.8, \text{ and } 4.3\%$). The test results indicated that the ultimate shear strength was dependent upon a/d and ρ , and that SFRLC with $V_f = 1\%$ showed significantly greater shear strength (by 60 to 210%) than equivalent beams without steel fibers. A shear strength design equation was developed based on the truss model and test data of their nine and others' previous 24 SFRC specimens (Swamy et al. [10]). This equation, which will be used for analysis in this prospectus, was also shown to correspond well to their seven SFRLC specimens (mean ratio of tested to predicted strength = 0.95; standard deviation = 0.11).

Theodorakopoulos and Swamy [11] investigated the punching shear behavior and strength of SFRLC slab-column connections (Figure 2.5). Twenty connection specimens were tested for variables of steel fiber types (crimped, rectangular sectional, hooked, and paddle types), V_f (0.5 and 1%), reinforcing ratios of tension and compression slab steel (0.32 and 0.57%), column size (100, 150 and 200 mm; 4, 6 and 8 in.), and concrete compressive strength ($f'_c = 17.8$ to 58.6 MPa; 2.6 to 8.5 ksi). Overall, the addition of steel fibers in SFRLC slab-column connections increased the gravity load at first cracking (by 33 to 50%), at yielding (by 12 to 80%), and at punching (by 30 to 100%). Usage of paddle steel fibers with $V_f = 1\%$ resulted in the greatest punching shear strength.

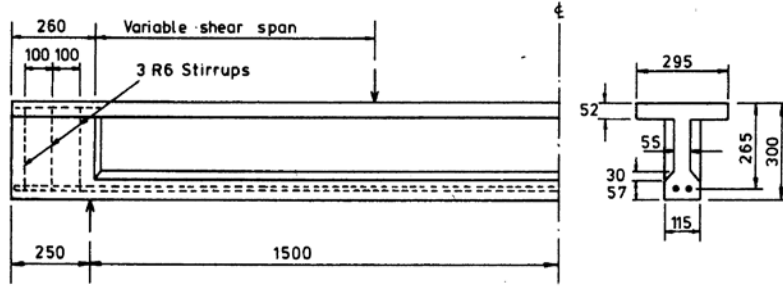


Figure 2.4. Elevation and Section of Test Beam (Adapted from Swamy et al. [10]; Conversion: 1 mm = 0.039 in.)

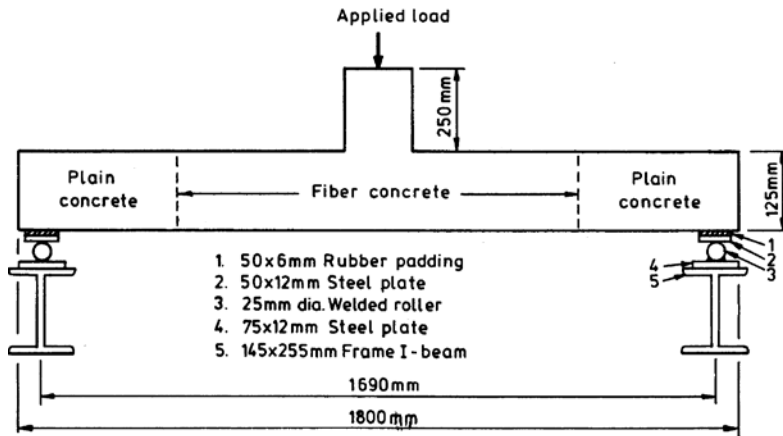


Figure 2.5. Details of Test Slab Specimen (Adapted from Theodorakopoulos and Swamy [11]; Conversion: 1 mm = 0.039 in.)

2.1.2 Part II: Review of Previous Experimental Research for Small-Scale Material Testing

Experimental studies were conducted by Balaguru et al. [5], [6] to assess the applicability of discrete steel fibers for improving the mechanical properties of normal-strength (42 MPa; 6 ksi) and high-strength (62.1 MPa; 9 ksi) lightweight concrete. The experimental programs consisted of three-point loading tests of prisms per ASTM

(American Standard for Testing and Materials) C1018 [13], splitting tensile and compressive strength tests of cylinders per ASTM C496/496M [14], and direct shear tests. In their experimental studies, it was found that the addition of steel fibers to lightweight concrete increased the compressive strength (f'_c) by 7 to 70%, splitting tensile strength (f_{ct}) by 10 to 170%, and modulus of elasticity (E_c) by up to 65%. Also, SFRLC exhibited excellent flexural ductility and shear strength. These improved mechanical properties were observed for all combinations of the fiber aspect ratios (60, 75, and 100) and steel fiber volume fractions (0.55, 0.75, 0.9 and 1.1%).

Higashiyama and Banthia [15] evaluated relationships between shear and flexural toughness for both SFRC and SFRLC. Materials used for their research consisted of two types of lightweight coarse aggregates (pumice and expansive shale), and two different lengths (38 and 63.5 mm; 1.5 and 9.2 in.) of crimped steel fibers with 1 mm (0.039 in.) diameter. Two fiber volume fractions ($V_f = 0.5$ and 1%) were selected for four-point loading tests in accordance with ASTM C1609 [14] (Figure 2.6) and for direct shear tests (Figure 2.7). The test results indicated that there was a linear relationship between shear and flexural strength for both SFRC and SFRLC, and that for a given fiber type and volume fraction, SFRC exhibited better shear and flexural toughness properties than SFRLC.

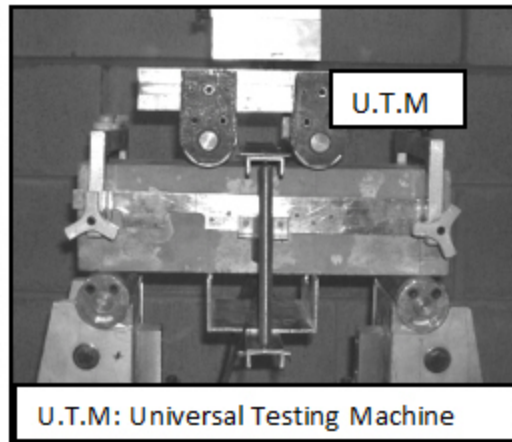
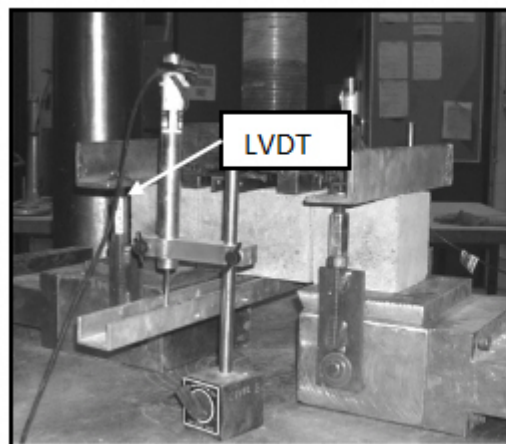
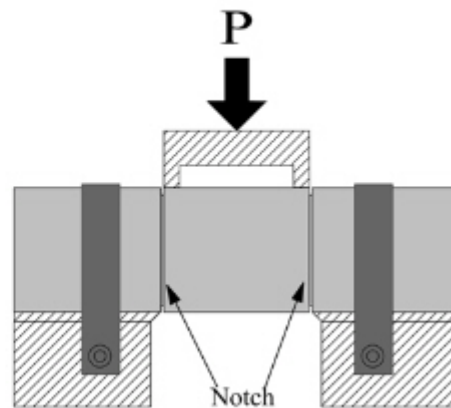


Figure 2.6. Flexural Toughness Test Setup
(Adapted from Higashiyama and Banthia [15])



(a) Direct Shear Test



(b) Schematic of Direct Shear Test

Figure 2.7. Direct Shear Test Setup (Adapted from Higashiyama and Banthia [15])

Swamy and Jojagha [7] performed a variety of workability tests for both SFRC and SFRLC in the fresh state, including inverted slump cone tests, standard slump and flow table tests, and vibrator-based remolding (VB) tests. Four different types of steel fibers (plain, paddle, hooked, and crimped) and four (length-to-diameter) aspect ratios of steel

fiber ranging between 50 and 100 were tested. Both SFRC and SFRLC with $V_f = 1.0\%$ showed relatively poor workability, and it was concluded that pulverized fuel ash (PFA) and water-reducing-plasticizing admixture should be added to release inter-locking friction between fibers and aggregates. From the similar tests of Balaguru and Ramakrishnan [4], it was concluded that toughness and energy absorption for SFRLC were equivalent to those for SFRC.

Swamy and Jojagha [8] experimentally assessed material characteristics of SFRC and SFRLC under impact loads by means of drop hammer and drop ball tests in accordance with ACI 544R-78 [16]. Three and four mixes were tested for normal weight and lightweight concrete, respectively. Both SFRC and SFRLC with $V_f = 1\%$ had greater impact resistance than those without steel fibers by a substantial degree, up to a factor of 10. The effects of steel fiber shape and geometry were evident by the fact that the number of shocks needed to fail was 536 and 793 for paddle and hooked shapes, respectively, but much less (124 and 192) for crimped and plain shapes.

2.2 REINFORCED CONCRETE BEAM-COLUMN CONNECTIONS WITH HEADED BARS

This section briefly describes the existing literature of experimental tests of reinforced concrete beam-column connections with headed bars, and a review of ACI standards and recommendations. The literature review of the anchorage details is also included to emphasize the behavior of heads used to transmit structural loads by bearing. This section consists of two parts: Part I summarizes ACI standards and recommendations, and Part II summarizes experimental research programs.

2.2.1 Part I: Summary of ACI Standards and Recommendations

In 2008, new provisions for headed bars were added to ACI 318. Sections 12.6.1 and 12.6.2 detail the development of headed bars and the limiting conditions for use of headed bars. ACI 318-08 [17] also introduces new provisions (Section 3.5.9) for

obstructions or interruptions of the bar deformations, which should not extend more than $2d_b$ from the bearing face of the head (Figure 2.8). ASTM A970/A970M-07 [18] “Standard Specification for Headed Steel Bars for Concrete Reinforcement,” should also be satisfied by the requirements of Section 3.5.9.

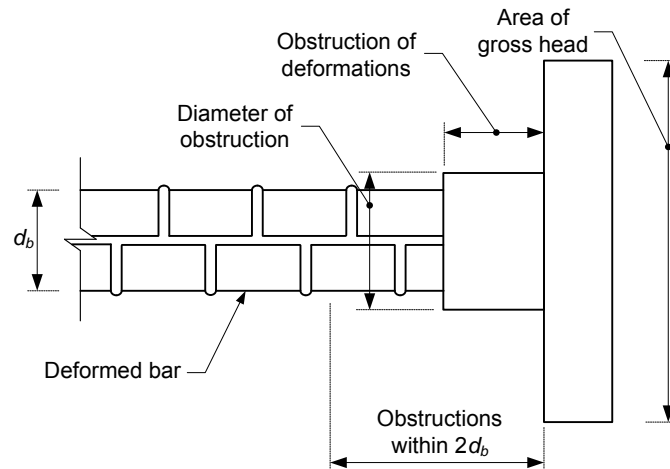


Figure 2.8. Headed Deformed Reinforcing Bar Requirements for Bearing of Deformation (Reproduced; ACI 318-08 [17])

ACI 318-08 [17] Appendix D provides guidelines for the design of plain headed bars and headed anchors, bolts, or headed anchors in concrete. In ACI 318-08 [17] Appendix D, the concrete capacity design (CCD) methodology is used to determine the anchorage capacity of headed anchors installed in mass plain concrete. In the CCD method, no bond stress is assumed along the length of a bar, and the concrete is assumed to be unconfined. ACI 318-08, Appendix D also describes the typical failure modes for steel elements with anchors under tensile and shear loading. Figure 2.9 shows the typical failure modes of steel anchors in tension.

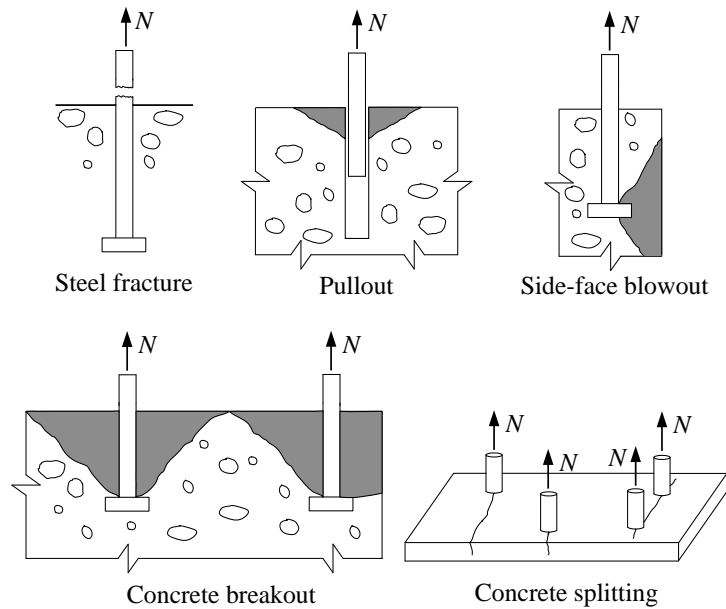


Figure 2.9. Failure Modes for Headed Anchors (Reproduced; ACI 318-08 [17])

Design guidelines for headed bars in beam-column connections were incorporated into the 2002 edition of the ACI 352R report on the basis of both monotonic (DeVries et al. [19]; Bashandy [20]; Wright and McCabe [21]) (or repeated (Bashandy [20])) and reversed cyclic tests (Wallace et al. [22]; Bashandy [20]). To summarize briefly some of their experiments, Devries et al. [19] reported experimental test results on the anchorage capacity behavior based on several factors. These factors include the embedment depth, clear cover to the bar, orientation of the bar, the head geometry and dimension, and the anchorage region details (see Figures 2.10 to 2.12). A total of 150 headed bar pullout tests were performed with varying embedment-to-depth ratio, edge distance, head size and bar diameter, transverse reinforcement details, development length, and concrete compressive strength. Figure 2.13 shows one of the typical pullout failures of a shallow embedded headed reinforcing bar.

Wright and McCabe [21] conducted 70 beam-end specimens test at the University of Kansas to investigate the performance of headed reinforcement. Three main types of

reinforcement were used for test configuration which included straight bars, 180-degree hooked bars, and headed bars to better make comparisons and show the efficiency of using headed bar. These studies recommend the development length for headed bars along with some other specifics such as the location of heads and the amount of head-restraining reinforcement required to prevent prying action of headed bars placed near the concrete-free surface. Figure 2.14 represents the schematic of test apparatus.

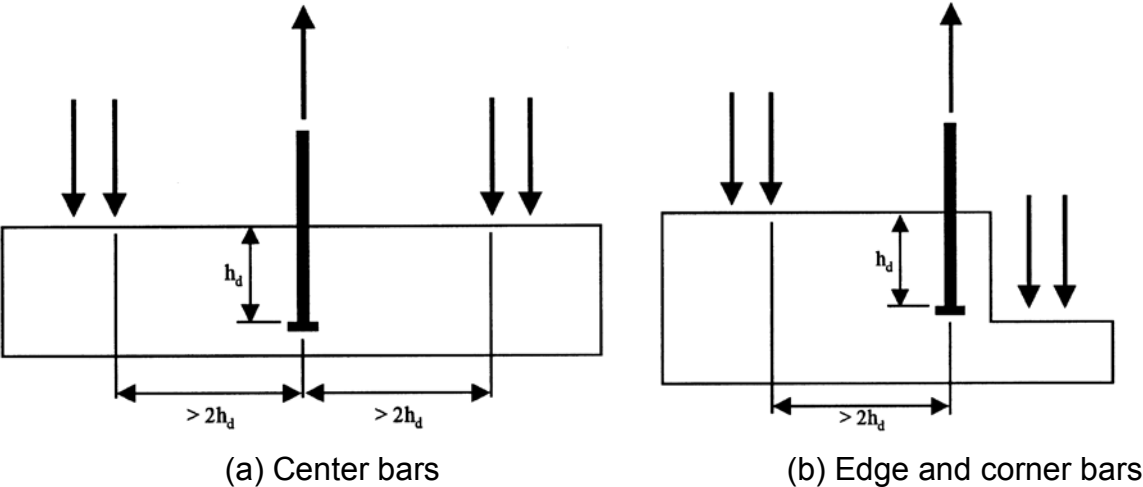


Figure 2.10. Shallow Embedment Pullout Test Setup

(Adapted from DeVries et al. [19])

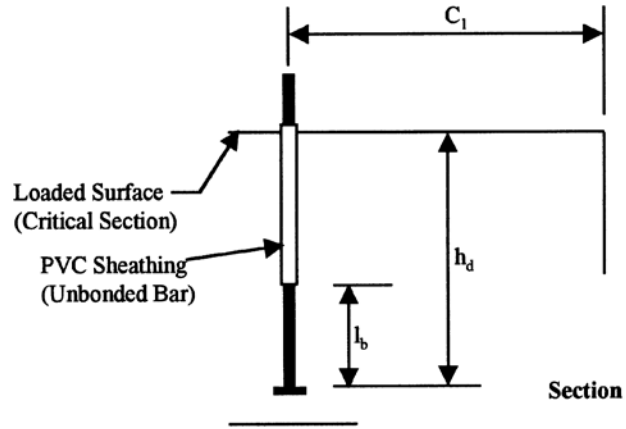


Figure 2.11. Comparison of Embedment Depth h_d and Bonded Length l_b in Concrete (Adapted from DeVries et al. [19])

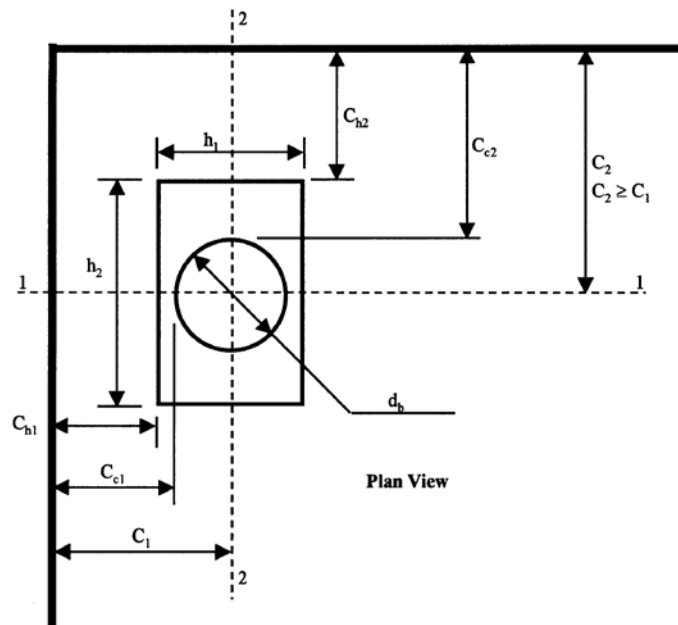


Figure 2.12. Edge Distance and Head Parameters (Adapted from DeVries et al. [19])

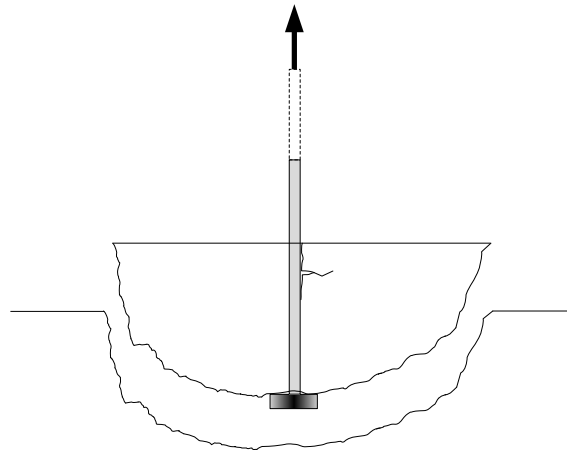


Figure 2.13. Pullout Cone Failure

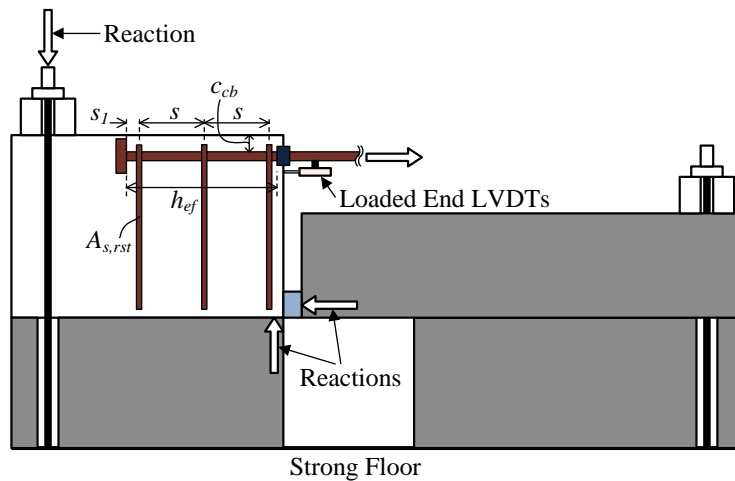


Figure 2.14. Schematic of Test Specimen and Setup
(Reproduced; Wright and McCabe [21])

ACI 352R-02 [23] defines two different development lengths of headed bars as functions of $(f_y d_b \sqrt{f'_c})$ for Type 1 and Type 2 beam-column connections. A Type 2 connection is defined to have sustained strength under deformation reversals into the inelastic range, whereas a Type 1 connection is defined as a connection designed with no consideration of significant inelastic deformation. The critical section for Type 2

connections is defined to be located at the outer edge of joint transverse reinforcement, and at the joint-member interface for Type 1 connections. Furthermore, as the concrete bearing capacity is substantially higher in the diagonal compressive strut, ACI 352R-02 [23] (Section 4.5.3.2 and Figure 4.9) recommends that a head be located within 50 mm (2 in.) from the back of the joint core (see Figure 2.15). For details of the head, ACI 352R-02 [23] refers to ASTM A970/A970M-98 [24], where the net bearing area A_{brg} was recommended to be greater than $9A_b$. The current version of ASTM A970/A970M [18] no longer specifies a minimum A_{brg} .

To provide the state-of-the-art information on headed reinforcement, ACI Committee 408, Development and Splicing of Deformed Bars, and ACI Committee 439, Steel Reinforcement, are jointly preparing a new report on Headed Ends for Anchorage and Development of Reinforcing Bars. In this report, a broad overview of mechanical anchorage and headed bars is provided, including definitions, historical development, and descriptions of various types of headed end devices, as well as previous research and applications. This report refers to ACI 352R-02 [23] for the use of headed bars in beam-column connections.

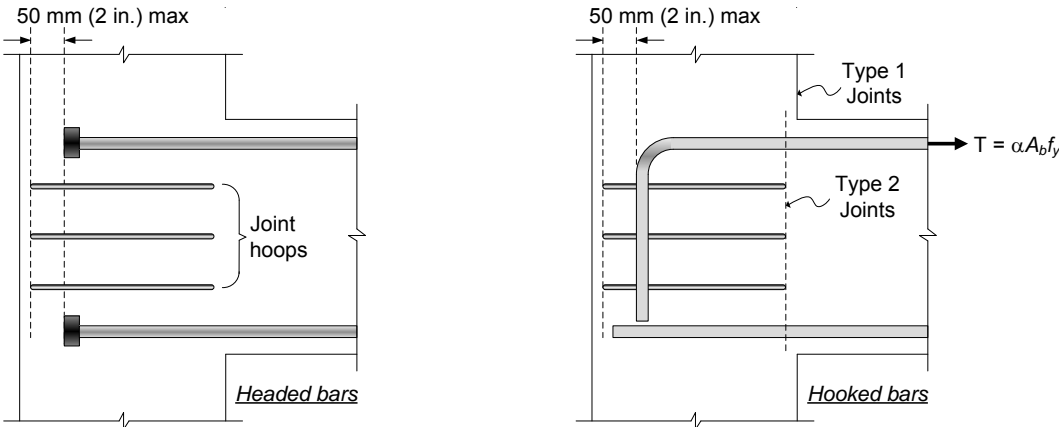


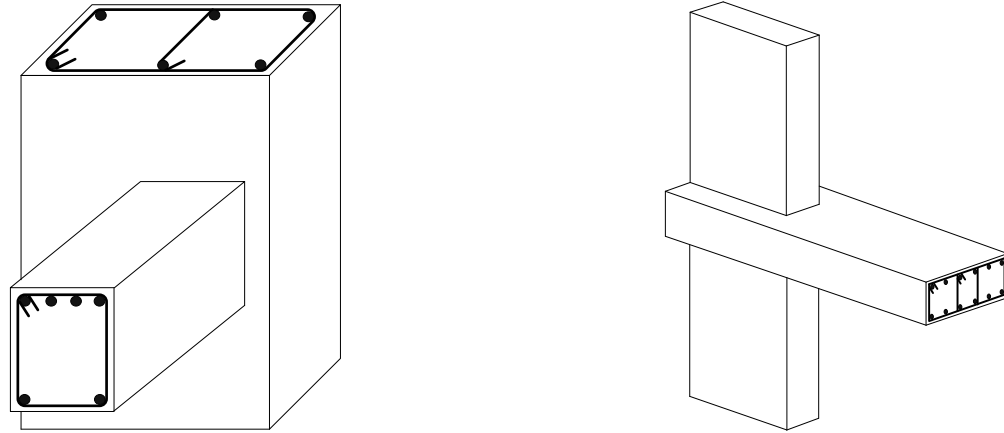
Figure 2.15. Location of Headed and Hooked Bars (Reproduced from ACI 352-02 [23])

2.2.2 Part II: Summary of Experimental Research

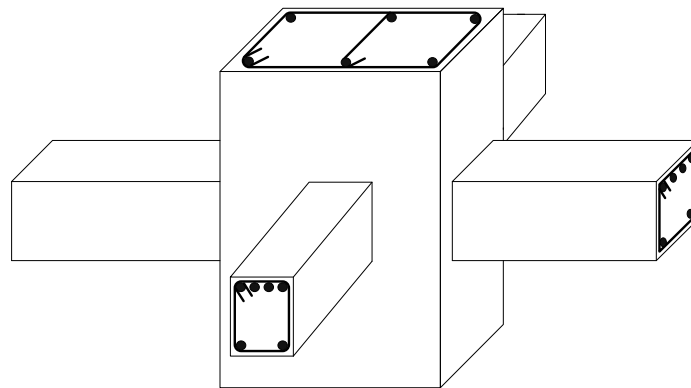
The previous tests, 77 of which are Japanese publications written in Japanese, included 69 interstory exterior connections, 17 (T-shaped) roof-interior connections, and 7 knee connections (Kang et al. [25]). There are only a few available reports on these seismic tests published in English (Bashandy [20]; Wallace et al. [22]; Chun et al. [26]; Lee and Yu [27]; Kang et al. [28]).

For the exterior connections, headed bars were employed for top and bottom beam reinforcement while they were used for the column reinforcement in the roof-interior connections. Most of the subassemblies were planar without any transverse beam or slab; only a small number of the exterior connections included one or two transverse beam(s) framing perpendicular to the main beam into the column. Two of the exterior connections (Matsushima et al. [29]) had one beam at each of the two principal directions of the rectangular-shaped column, and they were loaded in a combination of the two directions. Of the exterior connection studies, one (Ishida et al. [30]) investigated the performance of headed bars used in a wide beam-column connection in which some of the headed bars were anchored in a transverse beam outside the connection. One (Lee and Yu [27]) was an eccentric exterior connection. Figure 2.16 represents the schematic diagrams of the investigated beam-column connections. Almost half of the specimens had multiple layers of headed bars in the beam(s) or the column.

The main test variables included the development length for headed bars, clear cover to headed bars, type of anchoring devices, and head size, as well as the compressive strength of concrete and joint failure mode. The development length provided for headed bars ranged widely from $6d_b$ to $23.7d_b$, when measured from the joint-member interface. In most specimens, the net head bearing area A_{brg} was 2.6 to 8 times the reinforcing bar area A_b .



(a) Eccentric Exterior Beam-Column Connection (b) Wide Beam-Column Connection



(c) Interior Beam-Column Connection

Figure 2.16. Schematic Diagrams of Investigated Beam-Column Connections

The tested compressive strength of concrete ranged approximately from 24 to 138 MPa (3.5 to 20 ksi), and it was higher than 69 MPa (10 ksi) in approximately 1/4 of the specimens. The tested clear bar spacing c_s in a layer varied from $1.2d_b$ to $7.6d_b$, which was typically not treated as a variable among the specimens in each program.

The performance of headed bars used for beams and/or columns, terminated in the joint cores, was investigated for all types of joint failure modes including beam or column hinging, joint shear failure, and bar bond-slip. Other investigated design variables

included the number of beam and/or column bars, the amount of joint transverse reinforcement, the type of reinforcing steel, and the level of column compression. The tested yield strength of steel ranged from 297 to 1,020 MPa (43 to 148 ksi), and was higher than 690 MPa (100 ksi) in approximately 1/3 of the specimens. Approximately 1/2 of all specimens were tested with large-diameter headed bars (No. 8 to 11; $d_b = 25$ to 36 mm). The pre-applied column compression varied from 0 to 12% of the column gross section area times the measured concrete compressive strength ($f'_{c,meas}$).

The literature review reveals the following findings: 1) the ACI 352 development length for headed bars in beam-column connections is appropriate and thus can be included in §21.7.5 of ACI 318-08; 2) a minimum net bearing area of $3A_b$ and minimum clear bar spacing of $2d_b$ could be suggested for both ACI 352R-02 and ACI 318-08, Chapter 21; and 3) ACI 318-08 requirements of the minimum side clear covers to the head and to the bar can be applied to headed bars in beam-column connections. The previous data and findings will be used as a foundation for the analysis in this study.

This Page Is Intentionally Blank

3. HYPOTHESES AND OBJECTIVES

Reinforcing congestion due to convergence of multiple 90-degree hooks is always a concern, often hindering concrete placement and vibration during casting. As a result, honeycombs (voids) can be produced, which are found after the forms are stripped and voids are exposed on the surface of the concrete. The congestion problem gets worse with a relatively large amount of transverse reinforcement, and the industry is in need of a solution. Thus, headed reinforcement is quickly becoming a preferred means for anchorage and development, and the use of steel fibers is gaining increased attention as a method for shear resistance and confinement.

It is hypothesized that potential solutions to strengthening steel-congested concrete structures and improving constructability include (refer to Figure 3.1):

- (1) use of headed deformed bars in lieu of hooked bars (Figure 3.2(a)),
 - (2) use of steel fibers to reduce the amount of transverse reinforcement (Figure 3.2(b)),
- and
- (3) use of self-consolidating concrete (SCC) (Figure 3.2(c)).

It is also hypothesized that simplified reinforcing eventually could lead to reduced construction time with substantial savings in costs.

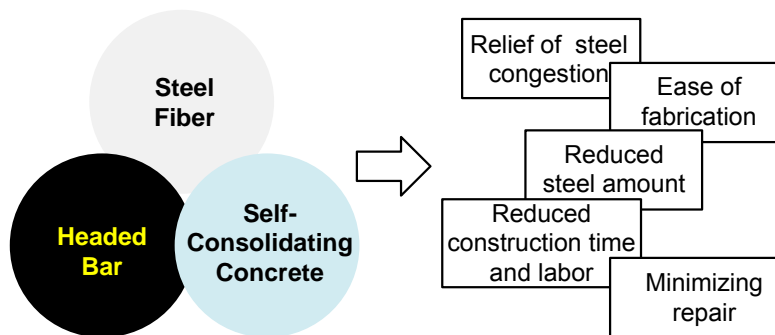
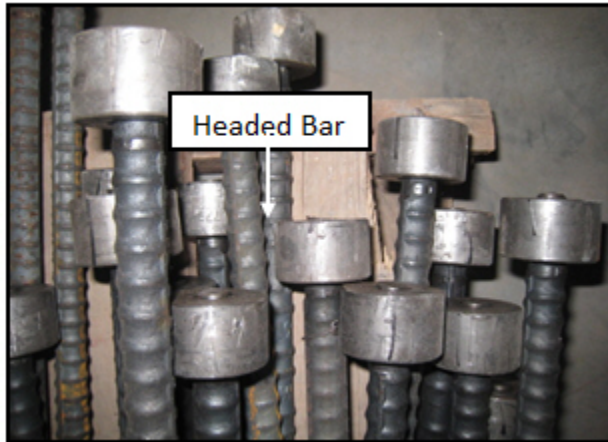
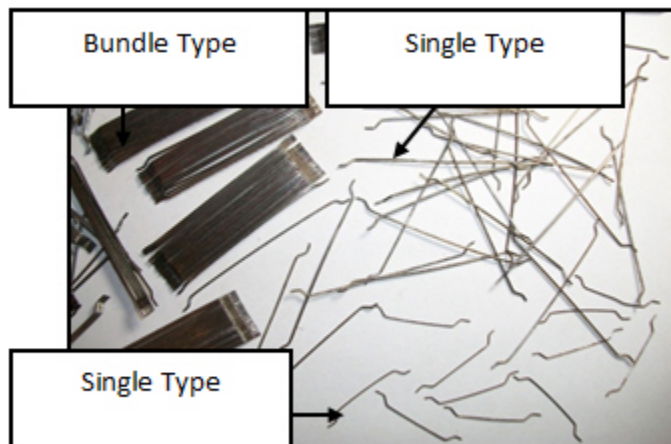


Figure 3.1. Potential Solutions to Relieving Steel Congestion in Concrete Structures



(a) Headed Bars



(b) Steel Fibers



(c) Self-Consolidating Concrete (SCC)

Figure 3.2. Headed Bars, Steel Fibers, and Self-Consolidating Concrete
(Conversion: 1 mm = 0.039 in.)

The objectives of this study are (1) to assess the shear behavior of steel fiber-reinforced lightweight concrete (SFRLC) beams, (2) to analyze the effectiveness of steel fibers in lightweight concrete beams, (3) to develop design shear strength equations for SFRLC, (4) to investigate the flexural behavior of prestressed SCC members subjected to nonlinear deformations, and (5) to assess the seismic performance of exterior beam-column connections with closely-spaced headed bars.

The following chapters describe the methodology regarding this study. This discussion of the methodology is divided into three chapters: (1) Chapter 4 covers the shear testing and analysis of steel fiber-reinforced concrete beams; (2) Chapter 5 presents the experimental and analytical studies of prestressed SCC beams; and (3) Chapter 6 deals with the seismic testing of exterior beam-column connections with closely-spaced headed bars.

This Page Is Intentionally Blank

4. LARGE SCALE TESTING AND ANALYSIS OF STEEL FIBER-REINFORCED LIGHTWEIGHT CONCRETE BEAMS

4.1 INTRODUCTION

Use of steel fiber-reinforced concrete (SFRC) is increasingly popular in the U.S. and other countries, as it improves mechanical properties and structural performance relative to not only plain concrete but even to conventionally reinforced concrete (with the same volume fraction). The addition of steel fibers to a reinforced concrete (RC, hereafter) beam is known to increase shear and flexural strengths and ensure ductile behavior (e.g., Narayanan and Darwish [31]; Kwak et al. [32]). The increased strength and ductility of SFRC members are associated with the post-cracking tensile strength of SFRC (e.g., Khuntia et al. [33]); thus, the use of SFRC helps in reducing the degree and width of cracking. The use of steel fibers also tends to increase the compressive ductility of brittle high-strength concrete (e.g., Shin et al. [34]; Imam et al. [35]). Along with these advantages, one of the most useful applications of SFRC is to relieve steel congestion by reducing the amount of shear or confining transverse reinforcement without sacrificing structural performance.

A similar improvement may be anticipated in steel fiber-reinforced lightweight concrete (SFRLC); although, the application of minimum steel fiber volume fraction to lightweight concrete is questionable. To answer this question, mechanical properties of SFRLC need to be first identified, and then structural performance should be verified through large-scale testing. Finally, a database needs to be compiled and studied for development or support of design models and code provisions. In this study, these procedures were conducted using previous and current research on SFRLC materials and structural members. Available studies on the structural behavior for large-scale steel fiber-reinforced members with lightweight concrete are scarce, although a large number of studies on SFRC structural members with normalweight concrete have been conducted by many investigators over the past decades (e.g., Narayanan and Darwish [31]; Ashour et al. [36]; Swamy et al. [10]; Kwak et al. [32]; Choi et al. [37]). Given this

gap, an experimental study on the shear behavior of SFRLC beams without stirrups was carried out. An assessment of the shear behavior of SFRLC beams “*with*” stirrups is not within the scope of the study, and no direct comparisons between SFRLC beams with and without stirrups are provided. Thus, a conclusion is not drawn as to whether a certain amount of steel fibers can replace all the shear reinforcement, or whether minimum shear reinforcement requirements can be waived for SFRLC beams, as is done for SFRC beams as per Section 11.4.6.1(f) of ACI 318-08. In general, shear strength of reinforced concrete beams without stirrups is dependent upon the compressive strength of the concrete, longitudinal reinforcing ratio, shear span-to-depth ratio, and member dimension (ACI 318-08, §11.2). Main parameters selected in this experimental study include the shear span-to-depth ratio, steel fiber volume fraction and concrete density (normalweight versus lightweight). A relatively high-strength concrete is used, as there is a growing need in the use of high-strength concrete.

4.2 EXPERIMENTAL PROGRAM

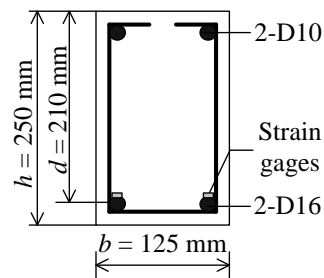
In Chapter 2, most of the available previous experimental research on SFRLC was summarized. This section describes current experimental studies of twelve concrete beams (six SFRLC, three SFRC, and three RC beams). These beams were simple-supported and loaded with two equal concentrated loads using a spreader steel beam (Figure 4.1). All beams were tested until failure to evaluate the influence of the shear span-to-depth ratio (a/d), steel fiber volume fraction (V_f), and concrete density on the shear strength of SFRLC and SFRC, as summarized in Table 4.1. The following subsections detail the design, construction, and instrumentation of the test specimens, as well as descriptions of the materials utilized.

4.2.1 Design of Test Specimens

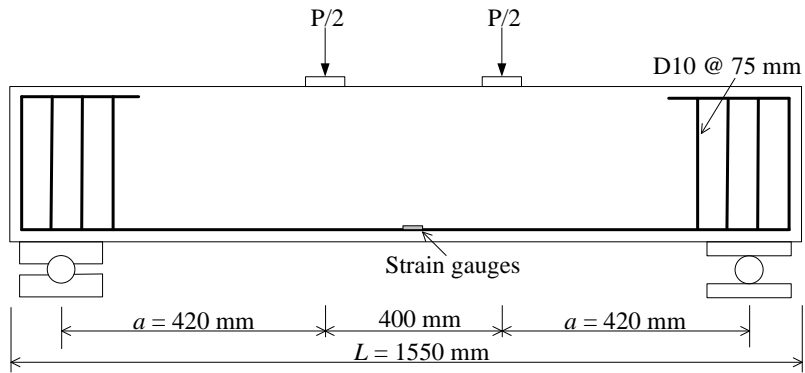
All beams were singly reinforced. The beams had the same cross-sectional dimension (125 by 250 mm; 4.9 by 9.8 in.) with an effective depth of 212 mm (8.3 in.); however, different total beam lengths (L) of 1.55, 1.97, and 2.40 m (61, 78 and 95 in.) were used for $a/d = 2, 3, \text{ and } 4$, respectively (Figure 4.1 and Table 4.1). When the shear span-to-

depth ratio (a/d) is less than 2, the beam end outside the loading points is considered the D-region (ACI 318-08, Appendix A). For this reason, all specimens had (a/d) greater than 2 to ensure applicability of beam theory. To investigate the effect of the dosage rate of steel fibers on shear strength, three kinds of steel fiber volume fractions (0, 0.5, and 0.75%) were selected. According to the new provision of ACI 318-08 (§5.6.6.2(a)), steel fiber-reinforced concrete should be considered acceptable for shear resistance when the dosage rate of deformed steel fibers is not less than 60 kg/m^3 (100 lb/yd^3). This rate is equivalent to a mix with $V_f = 0.75\%$ (see Table 4.2). All specimens were built before the inclusion of §5.6.6.2 in the ACI 318 code series. Of the twelve specimens, four (FLB-0.75 series and FNB-0.75-2 with $V_f = 0.75\%$) satisfied this minimum requirement for dosage rate (60 kg/m^3 ; 100 lb/yd^3).

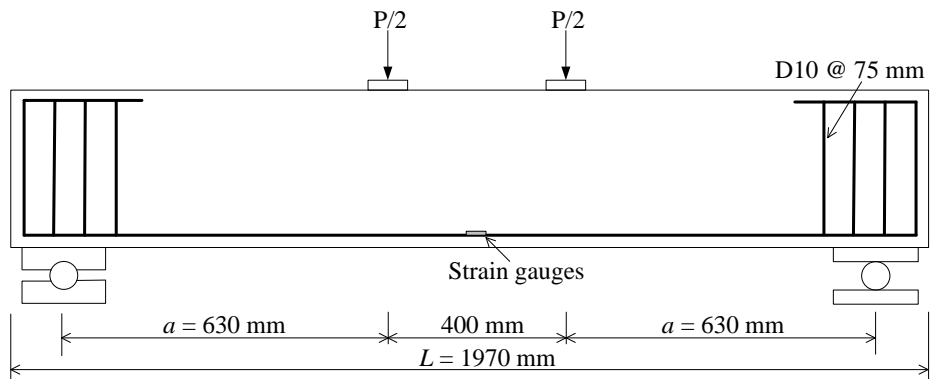
All specimens were designed such that shear failure would occur with the absence of shear reinforcement between the support and loading point.



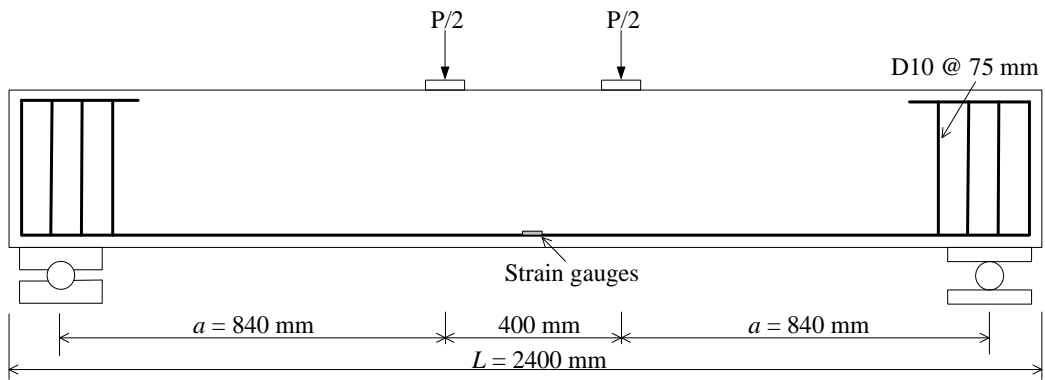
(a) Beam Section for All Specimens



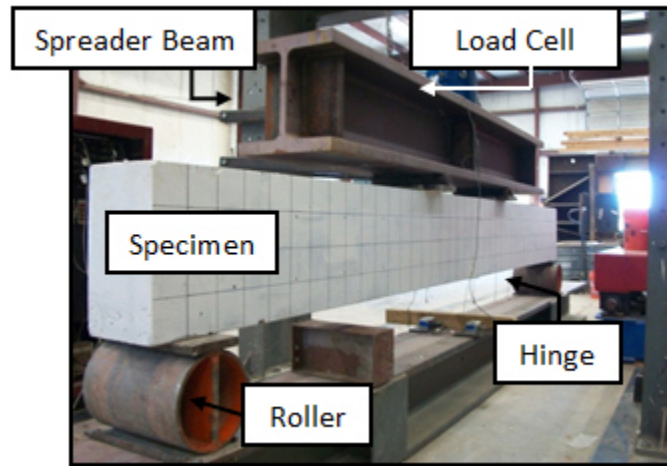
(b) Beam Specimen with $(a/d) = 2$



(c) Beam Specimen with $(a/d) = 3$



(d) Beam Specimen with $(a/d) = 4$



(e) Test Setup

Figure 4.1. Test Setup and Test Beams (Conversion: 1 mm = 0.039 in.)

Table 4.1. Descriptions of Test Specimens

Specimen	Beam sectional dimension (mm)		Shear span-to-depth ratio (a/d)	Flexural reinforcement ($\rho = 1.5\%$)	Steel fiber volume fraction, V_f (%)	Beam length (mm)
	Width (b_w)	Depth (h)				
LB-0-2	125	250	2	2-D16	0	1550
FLB-0.5-2	125	250	2	2-D16	0.5	1550
FLB-0.75-2	125	250	2	2-D16	0.75	1550
LB-0-3	125	250	3	2-D16	0	1970
FLB-0.5-3	125	250	3	2-D16	0.5	1970
FLB-0.75-3	125	250	3	2-D16	0.75	1970
LB-0-4	125	250	4	2-D16	0	2400
FLB-0.5-4	125	250	4	2-D16	0.5	2400
FLB-0.75-4	125	250	4	2-D16	0.75	2400
FNB-0.5-2	125	250	2	2-D16	0.5	1550
FNB-0.5-3	125	250	3	2-D16	0.5	1970
FNB-0.5-4	125	250	4	2-D16	0.5	2400

F L(N) B – 0.5 – 2

Shear span-to-depth ratio (2 → $a/d = 2$, 3 → $a/d = 3$, 4 → $a/d = 4$)

Fiber-volume fraction (0 → $V_f = 0\%$, 0.5 → $V_f = 0.5\%$, 0.75 → $V_f = 0.75\%$)

B → Beam

L → lightweight concrete; N → normal weight concrete

F → Fiber

Conversion: 1 mm = 0.039 in.

Concrete shear strength (average $V_c = 24.1$ kN or 5.2 kips for lightweight, and 32.4 kN or 7.1 kips for normalweight) at any point between the support and loading point was designed to be smaller than the shear applied ($V @ M_n = 31.54$ to 54.88 kN; 7.1 to 12.3

kips) when the moment capacity of the beam would be reached. Simple supports were located at positions 150 mm (6 in.) from the beam ends (i.e., span length = 1.25, 1.67, and 2.10 m or 50, 65 and 83 in., respectively, for $a/d = 2, 3,$ and 4). Only at the supports, were shear stirrups ($A_v = 2 \times 71 = 143 \text{ mm}^2; 0.22 \text{ in}^2$) provided at spacing of 40 mm (1.6 in.). This was to avoid any potential local failure near the supports. The provided development length (l_p) of bottom bars with a 90 degree standard hooks sufficiently satisfied the requirements in ACI 318-08. For example, FNB-0.5-2 had l_p of 544 mm (21.4 in.), greater than l_{dh} of 222 mm (8.73 in.), where l_{dh} is the development length for a hooked bar required by ACI 318-08 (§12.5.2). Two D10 ($d_b = 10 \text{ mm}; 0.4 \text{ in.}$) top reinforcing bars were placed to engage the stirrups at the beam ends. Concrete clear cover used was 30 mm (1.2 in.) for both top and bottom reinforcement.

Table 4.2. Relations between Steel Fiber Dosage Rate and Volume Fraction (V_f)

lb/yd ³	kg/m ³	V_f (%)
75	44	0.55
100	59	0.74
125	74	0.92
150	89	1.10

Conversion: 1 lb/yd³ = 0.593 kg/m³

4.2.2 Material Properties

The concrete was made of Type I Portland cement (Table 4.3). Coarse aggregates used for the beams were expanded clay aggregates and crushed gravels with a maximum size of 19 mm (3/4 in.) (Table 4.4). Physical properties and chemical compositions of expanded clay aggregates are indicated in Tables 4.4 and 4.5, respectively. Fine aggregates used were natural river sands with a fineness modulus of

2.17 (Table 4.4). The unit weights of lightweight and normalweight concrete were 1,800 and 2,194 kg/m³ (112.5 and 137 lb/ft³), respectively.

Table 4.3. Physical Characteristics of Type I Portland Cement

Specific gravity	Fineness (cm ² /g)	Setting time (hour-minute)		Compressive strength (MPa; psi)		
		Start setting	End setting	3 days	7 days	28 days
3.14	3390	4-12	6-08	18.8 (2726)	26.2 (3799)	34.5 (5003)

Table 4.4. Physical Properties of Coarse and Fine Aggregates

Classification		FM	SG	ARA	Max diameter
Coarse aggregate	Expanded clay aggregate	6.6	1.34	9%	19 (mm); ¾ (in.)
	Crushed gravel aggregate	6.77	2.57	1.1%	19 (mm); ¾ (in.)
Fine aggregate: sand		2.17	2.56	1.51%	1.7 (mm); 0.07 (in.)

FM = Fineness modulus; Measurement of the coarseness or fineness of a given aggregate;
 SG = Specific gravity; ratio of the density of a given solid to the density of water;
 ARA = Absorption rate of aggregate; Rate of moisture absorption into the lightweight aggregate (per ASTM C127-04 [14]).

Table 4.5. Chemical Compositions of Expanded Clay Aggregate

SiO ₂ (%)	Al ₂ O ₃ (%)	Fe ₂ O ₃ (%)	TiO ₂ (%)	CaO (%)	MgO (%)	K ₂ O (%)	Na ₂ O (%)	Ig.loss (%)	Refract- oriness (SK)
57.8	18.4	8.81	0.96	0.65	1.00	2.82	0.63	8.2	10

Table 4.6. Physical Properties of High-Range Water Reducing Admixture

Type	Main ingredient	Solid content (%)	Specific gravity
EZCON	Polynaphtalene-sulfonate	41	2.6

Table 4.7. Physical Characteristics of SFRLC and SFRC Mixtures

Classification		LB-0	FLB-0.5	FLB-0.75	FNB-0.5
Quantity or fraction of elements	Cement (kg/m ³)	480	480	480	477
	Sand (kg/m ³)	560	560	560	602
	Lightweight aggregate (kg/m ³)	480	480	480	N/A
	Normalweight aggregate (kg/m ³)	N/A	N/A	N/A	909
	Silica fume (kg/m ³)	57.6	57.6	57.6	N/A
	HRWR (ℓ/m ³)	9.4	10	10.7	3.3
	Water cement ratio (%)	33	33	33	33
Slump (mm)		105	100	70	110

HRWR = High-Range Water Reducer;

Conversion: 1 kg/m³ = 1.667 lb/yd³, 1 ℓ = 0.001 m³ = 0.0353 ft³; 1 mm = 0.039 in.

A high-range water reducing admixture was used to obtain relatively high strength concrete properties ($f'_c = 39.6$ to 57.2 MPa; 5.7 to 8.3 ksi) (Table 4.6). Table 4.7 provides detailed mixture proportions for three aggregates and other elements used to

cast test beams. The water-to-cement ratio was 0.33 for all beams. Measured material properties of concrete mixes are summarized in Table 4.8.

Compressive and splitting tensile strengths (f'_c and f_{sp}) and modulus of elasticity (E_c) of concrete were obtained using 100 × 200 mm (4 × 8 in.) cylinders in accordance with ASTM C39/C39M [14] (Figure 4.2) and ASTM C496/C496M [14]. The modulus of rupture (f_r) was evaluated from three-point bending tests of 150 × 150 × 530 mm (6 × 6 × 20 in.) concrete prisms in accordance with ASTM C1609-C1609M [14] (Figure 4.3). The forms for all concrete specimens were stripped after 48 hours of curing, followed by moisture curing with burlaps. All cylinder, prism and beam specimens were tested at 28 days after casting.

A mid-span deflection (δ_{mid}) was not measured during the modulus of rupture testing since the testing program was undertaken before the inclusion of the ACI 318-08, §5.6.6.2 requirement where ASTM C1609-07 is referenced. According to this ACI 318 provision, SFRC should be considered acceptable for shear resistance, only if the prism flexural strength at $\delta_{mid} = L/300$ is neither less than 90% of the peak nor 90% of cracking moment (M_{cr}), and the strength at $\delta_{mid} = L/150$ is neither less than 75% of the peak nor $0.75M_{cr}$. Here, M_{cr} is calculated using the modulus of rupture ($f_r = 7.5\lambda\sqrt{f'_c}$) per §9.5.2.3 and λ is the ACI 318 modification factor accounting for the reduced mechanical properties of lightweight concrete relative to normalweight concrete with the same f'_c .

The flexural reinforcing bars (D16; No. 5) had an average yield strength of 442 MPa (64 ksi) and ultimate strength of 638 MPa (92.5 ksi), measured from three steel coupons (see Figure 4.4 and Table 4.9).

Steel fibers with hooked ends were used (Table 4.10 and Figure 4.5). As noted earlier, the bond performance of the hooked steel fibers in lightweight concrete was equivalent or superior to the paddle, crimped and plain shapes (Figure 4.5; Theodorakopoulos and

Swamy [11]; Swamy and Jojagha [8]). The nominal tensile strength of the steel fibers was 1,079 MPa or 156 ksi (provided by the manufacturer). The fiber factor (F) was 0.23 for $V_f = 0.5\%$ and 0.35 for $V_f = 0.75\%$, where F is equal to $(L_f/D_f)V_f d_f$ (see Figure 4.5 for notations) and d_f is the bond factor (= 0.5 for round fiber, 0.75 for crimped fiber, and 1 for indented fiber) (Narayanan and Darwish [31]; Ashour et al. [36]). The average fiber matrix interfacial bond strength for steel fibers was considered to be 4.15 MPa (0.6 ksi) (Swamy et al. [38]).

Table 4.8. Measured Material Properties of SFRLC and SFRC

Specimens	LB-0	FLB-0.5	FLB-0.75	FNB-0.5
Steel fiber volume fraction, V_f	0 %	0.5 %	0.75 %	0.5 %
Compressive strength, f'_c	39.6 MPa (5.7 ksi)	44.6 MPa (6.5 ksi)	47.7 MPa (6.9 ksi)	57.2 MPa (8.3 ksi)
Splitting tensile strength, f_{sp}	2.64 MPa (383 psi)	3.63 MPa (526 psi)	4.43 MPa (642 ksi)	4.86 MPa (705 ksi)
Modulus of rupture, f_r	5.33 MPa (773 psi)	7.36 MPa (1067 psi)	10.83 MPa (1570 psi)	8.38 MPa (1215 psi)
Modulus of elasticity, E_c	26.8 GPa (3886 ksi)	28.4 GPa (4118 ksi)	38.7 GPa (5612 ksi)	34.2 GPa (4959 ksi)

Table 4.9. Physical Properties of Flexural Reinforcing Bars

Classification	Yield strength	Ultimate strength	Percentage of elongation	Modulus of elasticity
D16 (No. 5)	442 MPa (64 ksi)	638 MPa (92.5 ksi)	19.5%	193 GPa (28,005 ksi)

Table 4.10. Physical Properties of Steel Fiber

Shape	Length	Diameter	Aspect ratio (L_f/D_f)	Specific gravity
Hooked	50 mm (2 in.)	0.8 mm (0.03 in.)	62.5	7.85

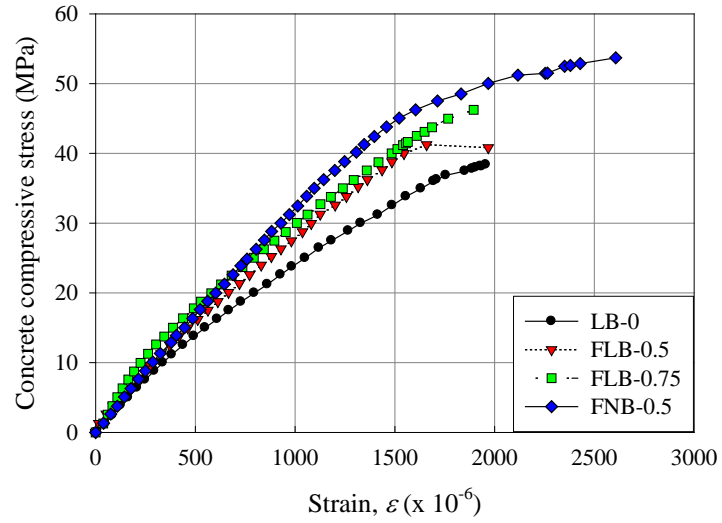


Figure 4.2. Concrete Compressive Stress-Strain Curve for All Specimens
(Conversion: 1 MPa = 145 psi)

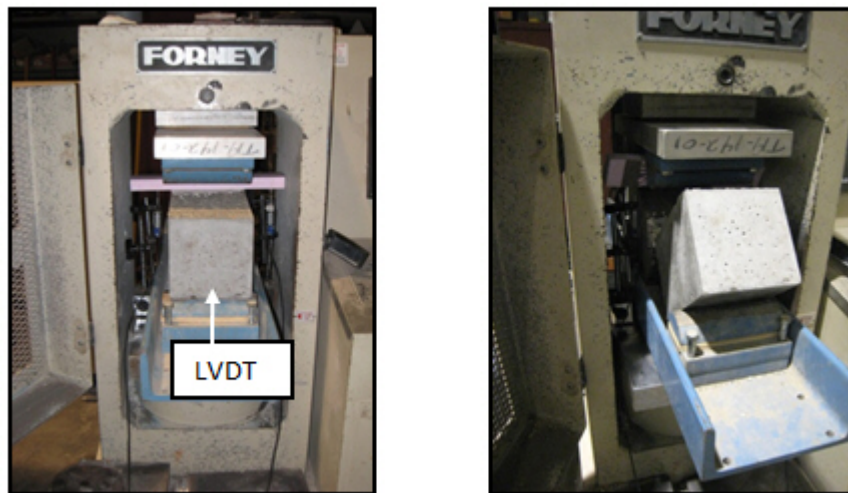


Figure 4.3. MOR Test



Figure 4.4. Tensile Strength Testing of Longitudinal Deformed Bar

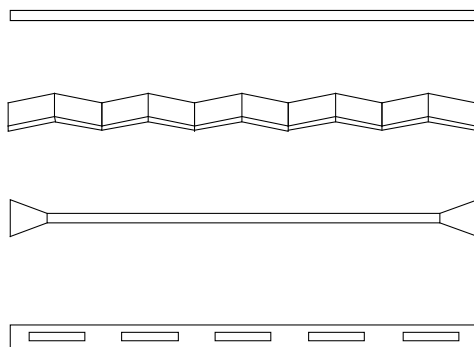
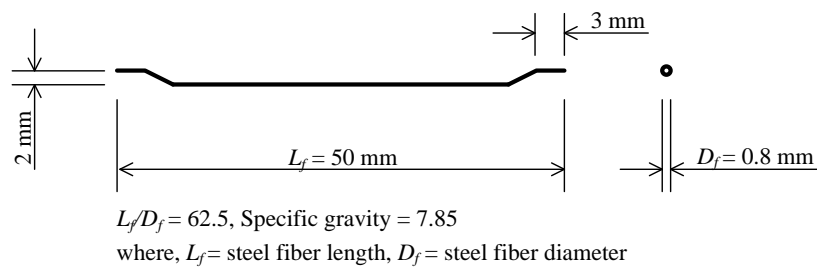


Figure 4.5. Details for Hooked Steel Fibers Used In This Study and Various Steel Fibers Shapes (Conversion: 1 Mm = 0.039 In.)

4.2.3 Testing and Instrumentation

In shear strength testing, the beams were simple-supported and subjected to two-point gravity loads. No shear forces were ideally applied inside the two loading points (Figure 4.1). Steel plates were installed to transfer the load from the spreader beam to the top surface of the beam to avoid local stress concentration. The vertical load was measured using a 50 ton (112 kips) capacity compression–tension load cell. An LVDT was mounted on the floor at mid-span of the beam to measure beam deflections during testing. In each loading step, crack width was measured using an eye gauge with a minimum resolution of 0.01 mm (0.0004 in.). To observe if the steel exceeded to the yield strain, two strain gauges per specimen were affixed on two reinforcing bars near the mid-span. Also at the mid-span, two concrete strain gauges were mounted on the side surface of each beam at 13 mm (0.5 in.) from the top and bottom surfaces.

4.3 OBSERVATIONS AND TEST RESULTS

In this section, the observed shear behavior and damage, along with experimental data obtained from twelve SFRC and SFRLC test specimens are described, with emphasis on the effects of lightweight concrete, steel fiber volume fraction and shear span-to-depth ratio on the shear strength.

4.3.1 Crack Patterns and Failure Modes

The sequential crack patterns of SFRLC specimens are shown in Figure 4.6. Flexural cracking and diagonal cracking occurred over the constant moment region and in the shear span region (between the loading point and the support), respectively. The degree of cracking and the crack width were reduced as the steel fiber volume fraction increased. This appeared to be due to the increased shear strength of SFRC and SFRLC beams. Three lightweight concrete beams without steel fibers (LB-0 series) and one SFRLC beam (FLB-0.5-4) did fail in brittle shear mode. On the other hand, most SFRC and SFRLC beams only failed in ductile flexure mode (Table 4.6). It is worthwhile to compare internal resultants measured for FLB-0.5-3 and FLB-0.5-4 which failed in

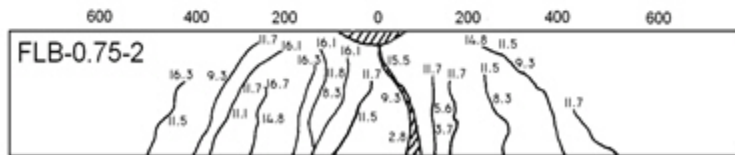
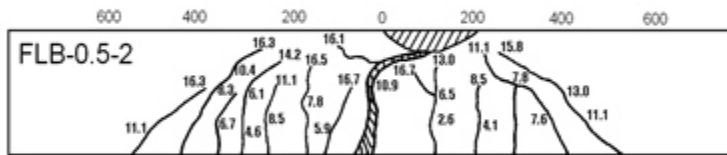
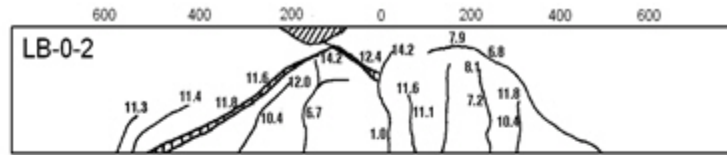
ductile and brittle modes, respectively, to assess the measured shear strength of SFRLC beams. This will be examined later in this chapter.

The FNB-0.5-2 and FLB-0.5-2 failed in flexure followed by shear failure, as summarized in Table 4.11. The more ductile behavior of FNB-0.5-2 versus FLB-0.5-2 indicates different shear capacities between SFRC and SFRLC beams. This result is consistent with the use of the multiplier (λ) that is applied to the shear strength of lightweight concrete members in ACI 318-08 (§11.2).

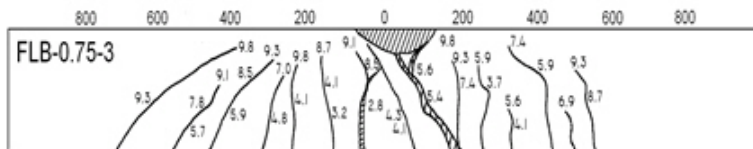
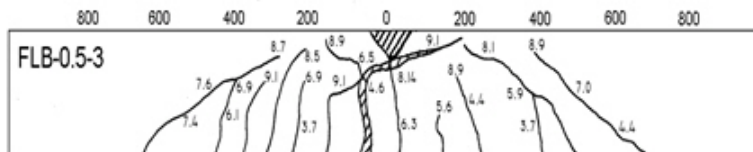
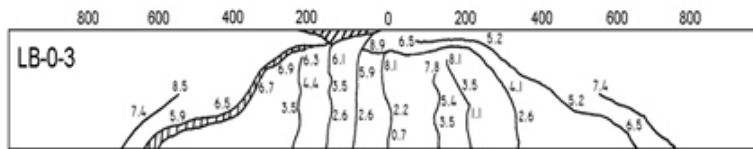
Table 4.11. Test Results and Failure Modes of Specimens

I.D.	Ultimate disp. (mm)	Shear force		Shear strength		Peak shear strength, ($\times\sqrt{f'_c}$)	Failure mode
		Diagonal cracking force, V_{cr} (kN)	Peak shear force, V_u (kN)	Diagonal cracking strength, v_{cr} (MPa)	Peak shear strength, v_u (MPa)		
LB-0-2	20.3	33.5	70.2	1.27	2.65	0.43	Shear
FLB-0.5-2	28.2	39.9	81.7	1.51	3.08	0.47	Flexure-Shear
FLB-0.75-2	46.3	45.6	83.1	1.72	3.14	0.46	Flexure
LB-0-3	18.6	25.4	45.1	0.96	1.70	0.28	Shear
FLB-0.5-3	47.4	34.5	45.4	1.3	1.71	0.26	Flexure
FLB-0.75-3	50.0	36.3	48.2	1.37	1.82	0.27	Flexure
LB-0-4	9.8	22.6	25.8	0.85	0.97	0.16	Shear
FLB-0.5-4	14.7	30.9	35.4	1.17	1.34	0.20	Shear
FLB-0.75-4	57.7	31.8	42.1	1.20	1.59	0.23	Flexure
FNB-0.5-2	34.3	40.7	77.2	1.54	2.91	0.39	Flexure-Shear
FNB-0.5-3	43.2	37.3	47.2	1.41	1.78	0.24	Flexure
FNB-0.5-4	77.8	34.5	39.5	1.30	1.49	0.20	Flexure

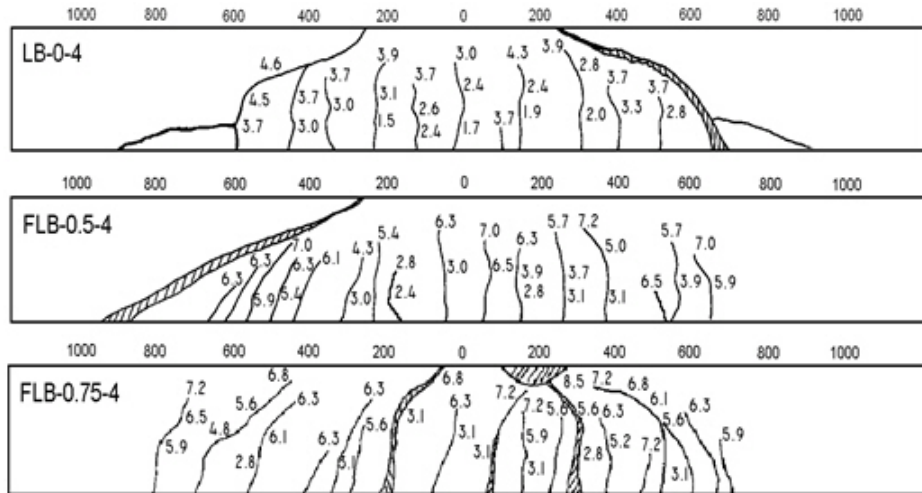
Note: The shear strength is estimated as applied shear divided by cross-sectional area of the beam. f'_c is in MPa. (Conversion: 1 MPa = 145 psi; 1 kN = 0.2248 kips)



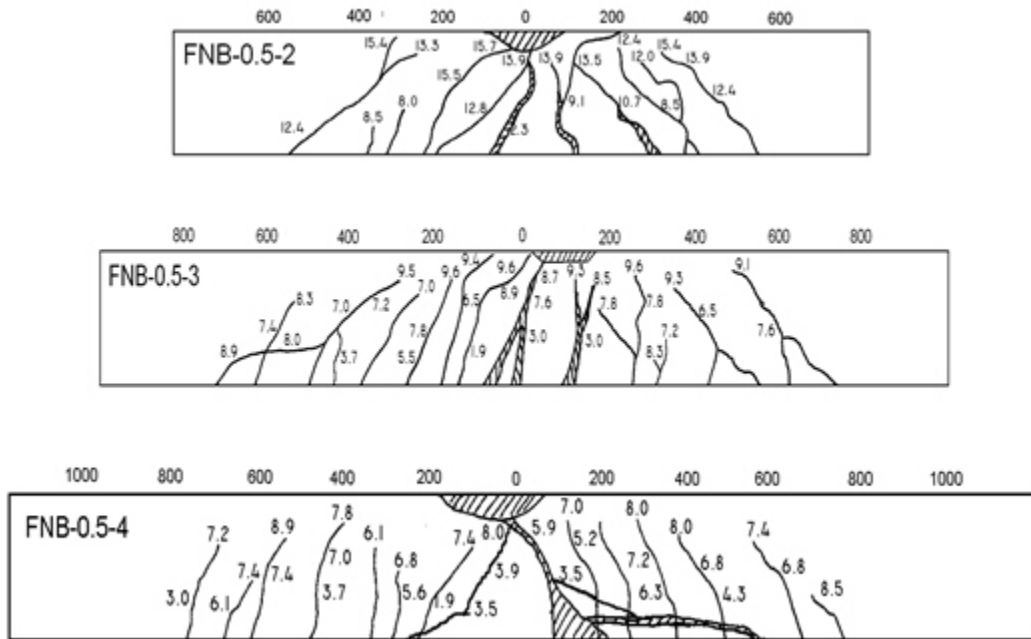
SFRLC with $(a/d) = 2$



SFRLC with $(a/d) = 3$



(c) SFRLC with $(a/d) = 4$



(d) SFRC with $V_f = 0.5\%$

Figure 4.6. Schematics of Sequential Crack Patterns (Numbers along the Beam: Distance from The Mid-Span [Mm]; Numbers On The Beam: Load [Tons]; Conversion: 1 Ton = 9.8 kN = 2.24 Kips)

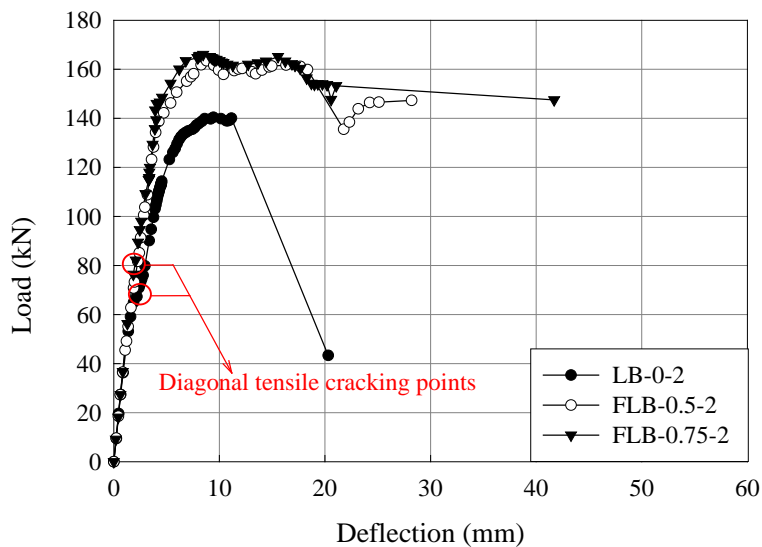
4.3.2 Load-Deflection Relations and Strain Gauge Measurements

Load versus deflection relations for beams with $a/d = 2$ are compared in Figure 4.7(a). The linear behavior of all specimens was represented up to diagonal tensile cracking, and subsequently nonlinear behavior was observed. A lightweight concrete beam without steel fibers (LB-0-2) exhibited brittle behavior, whereas SFRLC beams (FLB-0.5-2 and FLB-0.75-2) were characterized by more ductile behavior. The deflections of FLB-0.5-2 and FLB-0.75-2 at failure were 510% and 1250% of the deflections at first bar yielding (i.e., 2000 μ s as monitored by strain gauges), respectively. Similar behavior was noted for beams with $a/d = 3$ and 4 (Figures 4.7(b) and 4.8(c)). These results showed that shear failure did not occur prior to significant flexural yielding for SFRC and SFRLC beams with $a/d = 2$ to 3 (see Figures 4.7(a), 4.7(b), and 4.7(d)), due to increased shear strength provided by steel fibers. Note that the shear strength (24.1 to 32.4 kN; 5.4 to 7.3 kips) was calculated assuming that the absence of steel fibers was only 30% to 70% of the measured peak shear (Table 4.11).

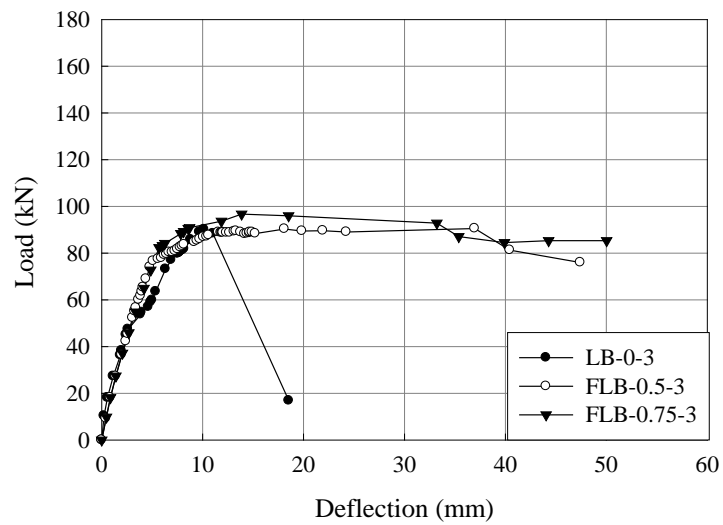
Figure 4.8 depicts comparisons between SFRC and SFRLC beams for different shear span-to-depth ratios but for a given $V_f = 0.5\%$. The failure modes for FNB-0.5-4 and FLB-0.5-4 were completely different when a/d of 4 was used. This observation gives a direct evidence of lower shear strength of SFRLC than SFRC under the same condition. The FNB-0.5-4, FNB-0.5-3, and FLB-0.5-3 did not fail in shear at $v_u = 0.20\sqrt{f'_c}$, $0.24\sqrt{f'_c}$ and $0.26\sqrt{f'_c}$ MPa ($2.4\sqrt{f'_c}$, $2.88\sqrt{f'_c}$ and $3.12\sqrt{f'_c}$ psi), respectively (Table 4.11); however, FLB-0.5-4 failed in shear at $v_u = 0.20\sqrt{f'_c}$ MPa ($2.4\sqrt{f'_c}$ psi). These results indicate that under relatively large bending moment (i.e., applied moment to shear ratio = 840 mm (33 in.); $a/d = 4$), the shear strength capacity (v_n) of SFRLC with $V_f = 0.5\%$ was about $0.20\sqrt{f'_c}$ MPa ($2.4\sqrt{f'_c}$ psi), whereas the v_n of SFRC with $V_f = 0.5\%$ was larger than $0.20\sqrt{f'_c}$ MPa ($2.4\sqrt{f'_c}$ psi). Under relatively small bending moment ($a/d = 2$), the ductility of the SFRC beam was better than the SFRLC beam (Figure 4.8), which also signals the higher shear strength of the SFRC beam. This result validates previous findings from the small-scale SFRLC material tests (Higashiyama and Banthia

[15]; Balaguru and Ramakrishnan [4]; Swamy and Jojagha [8]) that are reported earlier in this report. More detailed analysis on the shear strength of SFRLC beams will be discussed later.

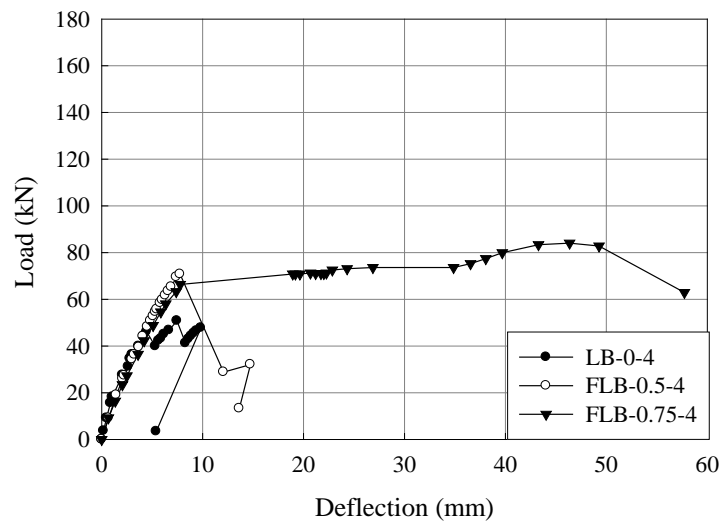
The presence of flexural yielding and strain hardening of reinforcing bars can be identified from load versus reinforcing bar strain relations, as shown in Figures 4.9 and 4.10. Here, two strain gauge values at the mid-span were averaged. For FLB-0.5-4, yielding of flexural reinforcing bars did not occur (Figure 4.10(a)). This was also noted from the observation that shear failure occurred with little ductility. Such a brittle shear failure, however, did not occur for FLB-0.75-4 with the same configuration except steel fiber volume fraction ($V_f = 0.75\%$) (Figure 4.10(b)). This observation gives a quantitative indication of the safe combination of shear span-to-depth ratio and steel fiber volume fraction that leads to the ductile design of SFRLC flexural members. Based on the results from this test program, the combination of either ($V_f = 0.75\%$ and $a/d = 4$) or ($V_f = 0.5\%$ and $a/d = 3$) is recommended for SFRLC beams. The effects of V_f and a/d on shear behavior are assessed more in detail in the following subsection.



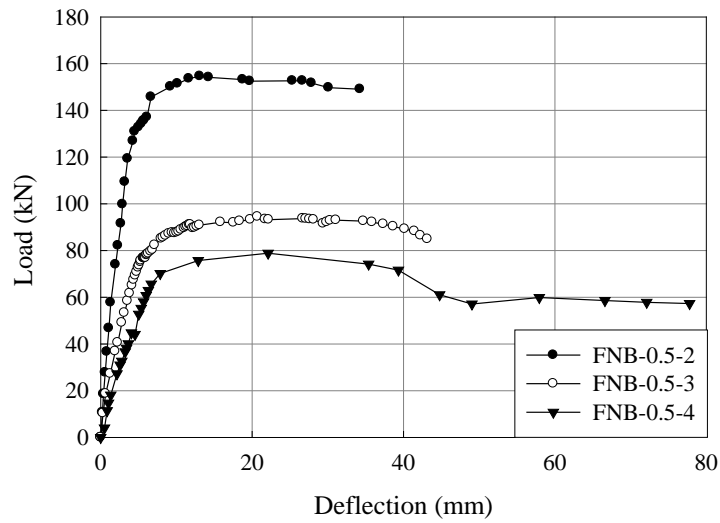
(a) Comparison between SFRLC Specimens with $a/d = 2$



(b) Comparison between SFRLC Specimens with $a/d = 3$



(c) Comparison between SFRLC Specimens with $a/d = 4$



(d) Comparison between SFRC Specimens with $V_f = 0.5\%$
Figure 4.7. Load-Deflection Relationships for SFRLC and SFRC
 (Conversion: 1 kN = 0.2248 kips; 1 mm = 0.039 in.)

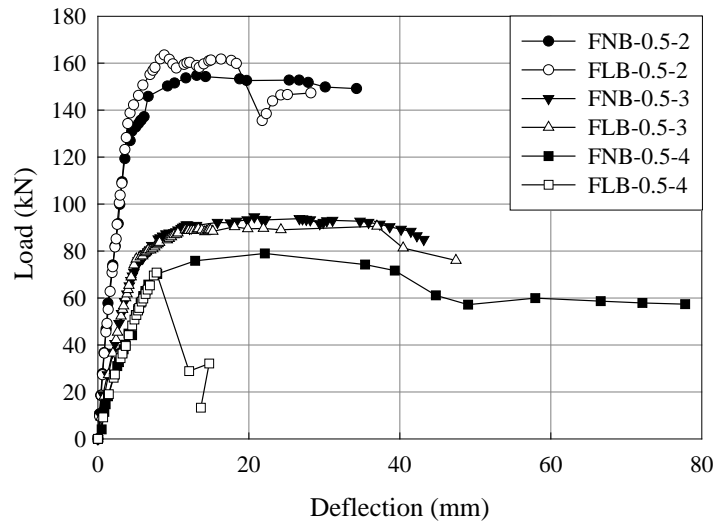
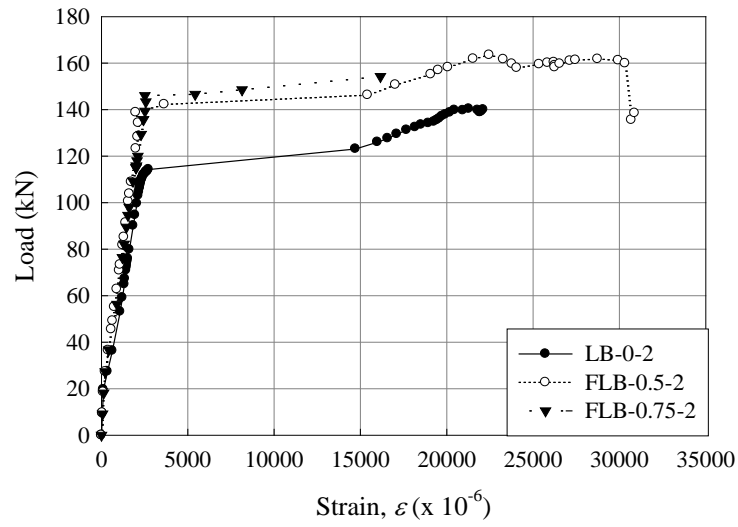
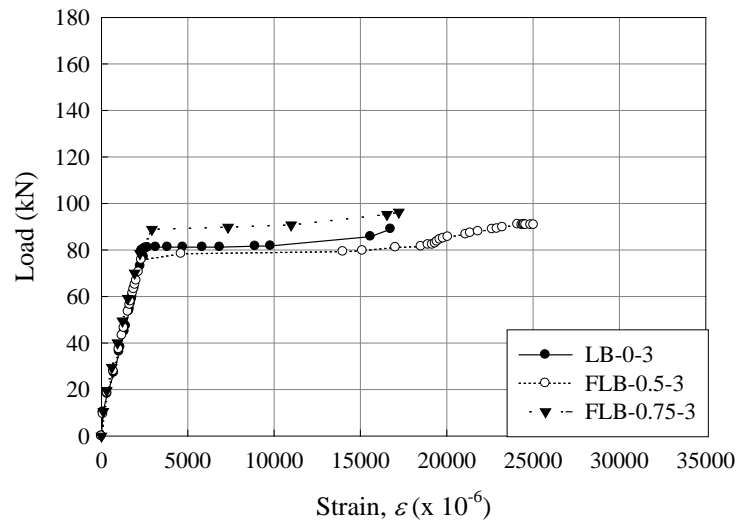


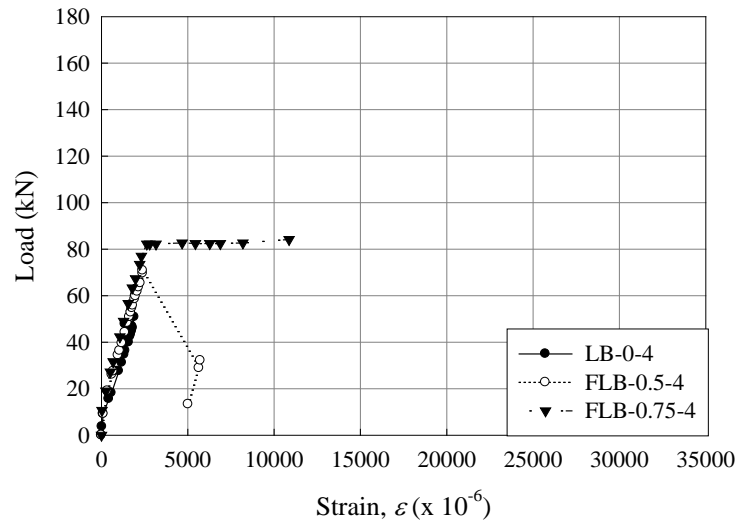
Figure 4.8. Comparison of Load-Deflection Relationships between SFRC and SFRLC
 with $V_f = 0.5\%$ (Conversion: 1 kN = 0.2248 Kips; 1 Mm = 0.039 In.)



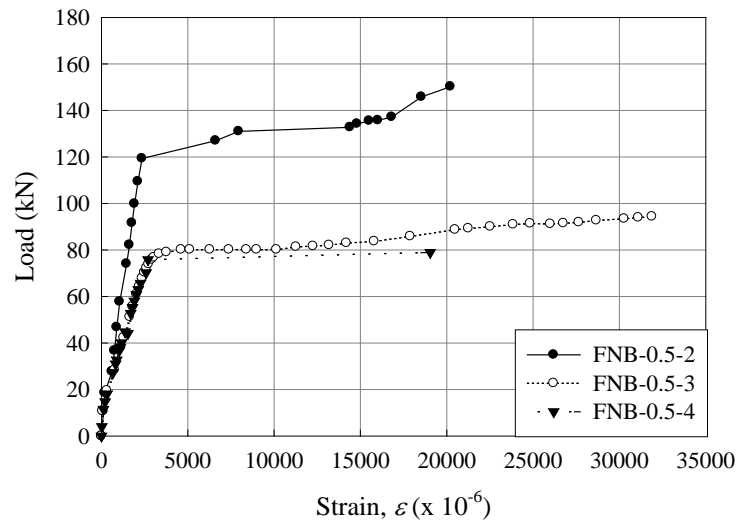
(a) Comparison between SFRLC Specimens with $a/d = 2$



(b) Comparison between SFRLC Specimens with $a/d = 3$



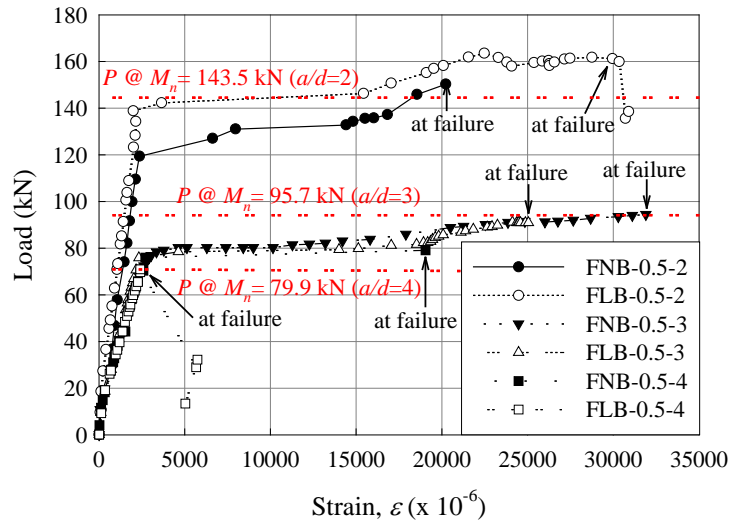
(c) Comparison between SFRLC Specimens with $a/d = 4$



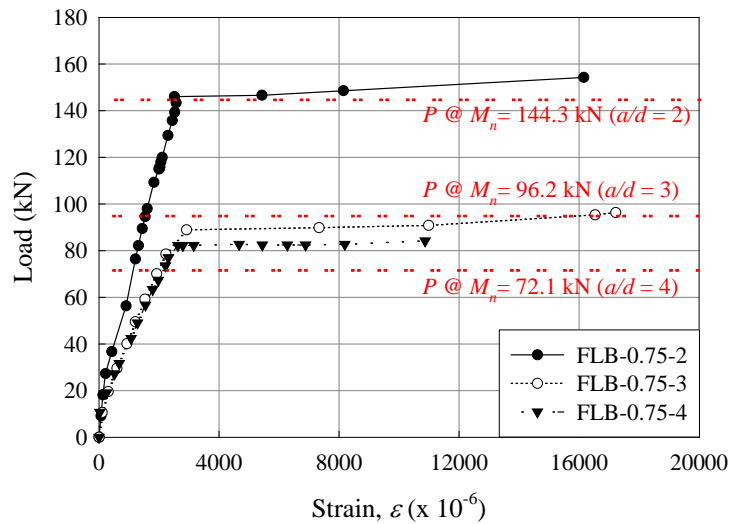
(d) Comparison between SFRC Specimens with $V_f = 0.5\%$

Figure 4.9. Load-Bar Strain Relationship for SFRLC and SFRC

(Conversion: 1 kN = 0.2248 kips)



(a) Comparison between SFRLC and SFRC with $V_f = 0.5\%$

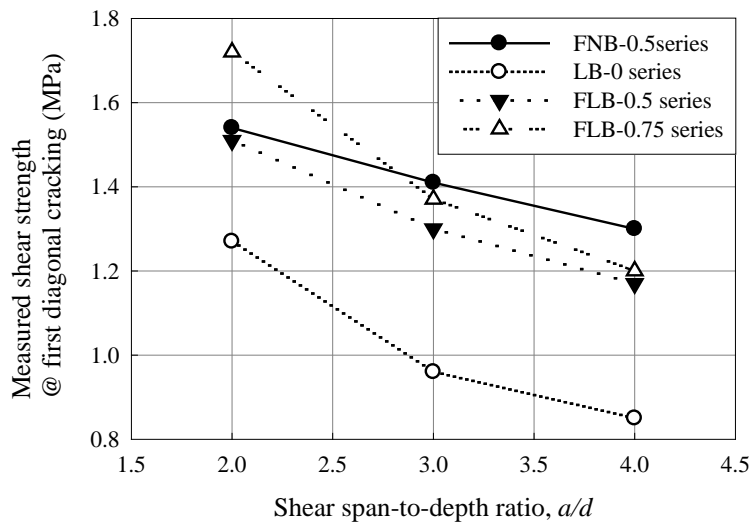


(b) Comparison SFRLC with $V_f = 0.75\%$

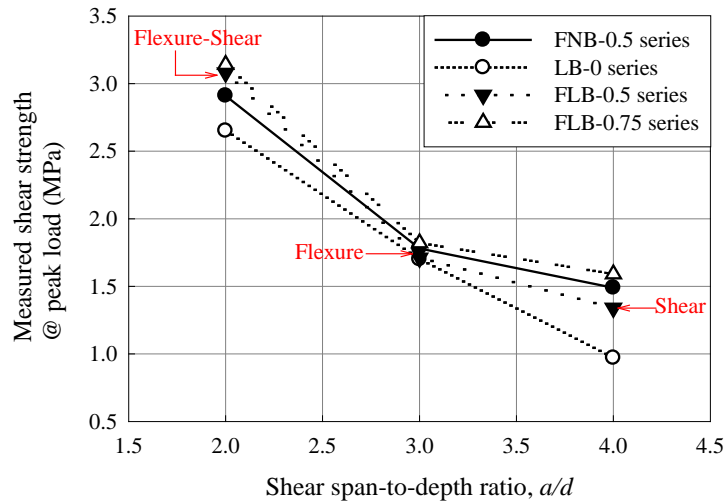
Figure 4.10. Comparison of Load-Bar Strain Relationships
(Conversion: 1 kN = 0.2248 kips)

4.3.3 Effects of Steel Fiber Volume Fraction and Shear Span-to-Depth Ratio

Figure 4.11(a) shows the relationship of measured shear strength (v_{cr}) at first diagonal cracking versus shear span-to-depth ratio (a/d). The v_{cr} values for SFRLC beams (FLB series) were larger than those for comparable lightweight concrete beams without steel fibers (LB-0 series) by 35% on average, likely due to the increased tensile splitting strength (f_{sp}) of SFRLC (see Table 4.8). The increased v_{cr} was the case for all a/d ratios. The v_{cr} was decreased as the a/d was increased due to the larger bending moment and associated principal stress. The delayed cracking (for lower a/d) eventually affected the ultimate shear behavior of the SFRLC beams. The FLB-0.5-2 and FLB-0.5-3 specimens exhibited ductile behavior, whereas FLB-0.5-4 did not achieve ductile flexural behavior. Figure 4.11(b) shows the relationship of measured shear strength (v_u) at peak load versus a/d . The shear strength at peak load for the FLB-0.5 series was increased by approximately 16%, 1%, and 38% for $a/d = 2, 3, \text{ and } 4$, respectively, compared with the LB-0 series. Similar results were found for the FLB-0.75 series. These results indicate that the shear strength capacity of SFRLC beams was increased with the addition of steel fibers. Moreover, the observed failure mode and beam ductility were significantly improved when steel fibers were added (see Table 4.11).



(a) Measured Shear Strength at First Diagonal Cracking versus Shear Span-to-Depth Ratio



(b) Measured Shear Strength at Peak Load Versus Shear Span-to-Depth Ratio
Figure 4.11. Measured Shear Strengths versus Shear Span-to-Depth Ratio (A/D)
 (Conversion: 1 MPa = 145 psi)

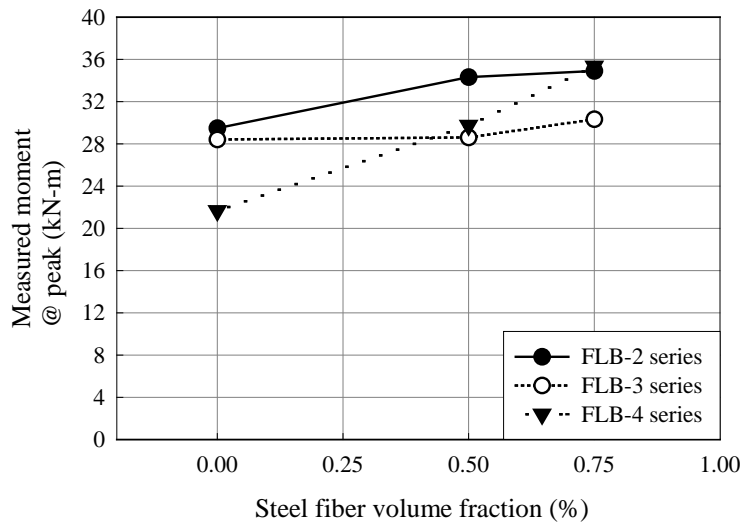


Figure 4.12. Measured Moment at Peak versus Steel Fiber Volume Fraction (V_f)

Figure 4.12 illustrates the effect of steel fiber volume fraction (V_f) on the flexural strength of the SFRLC beams. Only a 2% to 6% increase in flexural strength was noted when V_f was increased from 0.5% to 0.75% for the FLB-2 and FLB-3 series. This appeared to be due to the increased compressive and tensile strengths of SFRLC with larger V_f (see Table 4.8).

Though modest, this difference affected the applied shear at M_n and the associated shear strength at peak load. The modestly larger shear strengths at peak for FLB-0.75 series versus FLB-0.5 series (Figure 4.11(b)) were in part due to the increased flexural strength.

For $a/d = 4$, it is clear that the V_f affected the shear strength. The ductile failure mode was observed for FLB-0.5-4 versus FLB-0.75-4 (compare Figures 4.10(a) and 4.10(b)). For other a/d ratios (2 and 3), because the specimens failed in flexure the measured peak shear strengths were similar for both $V_f = 0.5\%$ and 0.75% (Figure 4.11(b)).

Although the larger V_f increased the beam ductility (see Figure 4.10(a)), both the V_f of 0.5% and 0.75% improved the shear strength sufficiently. The V_f values of 0.5% and 0.75% are equivalent to the steel fiber dosage rates of 45 to 60 kg/m³ (75 and 100 lb/yd³), respectively (see Table 4.2). The data in this study indicate that the ACI 318 minimum steel fiber dosage rate of 60 kg/m³ (100 lb/yd³) for shear resistance may be lowered to 45 kg/m³ (75 lb/yd³), which would improve the concrete workability tremendously. As noted, the workability problem with $V_f = 1\%$ was identified by Swamy and Jojagha [7] and practical engineers. Also as mentioned earlier, the only previous experimental study on large-scale SFRLC beams was conducted by Swamy et al. [10], where the value of $V_f = 1\%$ was used. Therefore, the finding in this study is of value in confirming the prior experimental hypotheses.

The effect of a/d on the ultimate shear strength of SFRLC beams needs to be assessed more carefully. It is common sense that, as the shear span-to-depth ratio becomes larger, the applied shear at which the beam moment strength (M_n) is reached becomes smaller. This was the main reason that the highest shear strength at peak was measured for $a/d=2$ (Figure 4.11(b)); however, if only the points representing the FLB-0.5 series are only compared, the effect of a/d on shear strength becomes more evident.

The measured shear forces for FLB-0.5-2 and FLB-0.5-3 were larger than FLB-0.5-4, but only FLB-0.5-4 experienced brittle shear failure. This result is one of the direct evidences to show that a moment-shear interaction is significant. Therefore, a term associated with the shear span-to-depth ratio should be included in the shear strength equation of SFRLC beams, as also seen in the shear strength equation (11-5) of ACI 318-08 for conventional concrete beams. Additionally, the validity of the shear strength equation should be evaluated using the data with various a/d values. This is done in the following section.

4.4 DESIGN SHEAR STRENGTH OF SFRLC BEAMS WITHOUT STIRRUPS

In the preceding sections, the observed behavior and the representative test data for twelve specimens were reported. In this section, the shear strength equations available for SFRC beams were evaluated as to whether or not they are also applicable to SFRLC beams, in consideration with the ACI 318 specified lightweight concrete factor (λ). Results from the current tests and the SFRLC beam tests conducted by Swamy et al. [10] were used for this evaluation to produce the best results. The test results of the companion SFRC beams were also used in the analysis. Note that the tests by Swamy et al. [10] are only previously reported.

The following three steps of the calibration approach were used. First, most available shear strength models for SFRC beams (not lightweight) were extracted from the

literature. Second, the lightweight concrete modification factor of λ ($= 0.75$) was accounted for by replacing f'_c with $\lambda^2 f'_c$ for SFRLC beams (this was not done for SFRC beams). This process is analogous to that in the ACI 318-08 code as shown in Equation (4.1).

$$\frac{v_c \text{ for lightweight concrete}}{v_c \text{ for normalweight concrete}} = \frac{\lambda \sqrt{f'_c}}{\sqrt{f'_c}} = \frac{\sqrt{\lambda^2 f'_c}}{\sqrt{f'_c}} \quad (4.1)$$

Finally, the ratio of measured peak shear strength to shear strength capacity calculated based on the existing model, except for the replacement of f'_c by $\lambda^2 f'_c$ for SFRLC beams, was determined for each specimen to make a direct comparison between the models. The mean, standard deviation, and minimum and maximum values of the ratios, as well as the slope of the linear regression lines were compared in this study (Tables 4.12 and 4.13).

The following list includes the available SFRC shear strength equations developed by other researchers:

(1) Narayanan and Darwish [31]

$$v_n = e \left[0.24 f_{sp} + 80 \rho \frac{d}{a} \right] + v_b \text{ (MPa)} \quad (4.2)$$

$$v_n = e \left[0.24 f_{sp} + 11600 \rho \frac{d}{a} \right] + v_b \text{ (psi)}$$

where f_{sp} = estimated using the splitting tensile strength of SFRC as shown in Equation (4.3);

$$f_{sp} = \frac{f_{cuf}}{(20 - \sqrt{F})} + 0.7 + 1.0 \sqrt{F} \text{ (MPa)} \quad (4.3)$$

$$f_{sp} = \frac{f_{cuf}}{(20 - \sqrt{F})} + 101.5 + 145 \sqrt{F} \text{ (psi)}$$

e = arch action factor = 1 for $a/d > 2.8$, and $e = 2.8d/a$ for $a/d \leq 2.8$;

a/d = shear span-to-depth ratio;

ρ = flexural reinforcement ratio;

F = fiber factor = $(L_f/D_f)V_f d_f$;

f_{cuf} = cube strength of fiber concrete = $1.2f'_c$ MPa (psi);

f'_c = concrete compressive strength, MPa (psi);

L_f = fiber length, mm (in.);

D_f = fiber diameter, mm (in.);

V_f = volume fraction of steel fibers;

d_f = bond factor = 0.5 for round fibers, 0.75 for crimped fibers, and 1 for indented fibers;

v_b = fiber pullout stress = $0.41\tau F$, MPa (psi); and

τ = average fiber matrix interface bond stress, taken as 4.15 MPa (600 psi), based on the recommendations of Swamy et al. [38].

(2) Ashour et al. [36]

Model 1 (modified Zsutty equation)

For $a/d \geq 2.5$,

$$v_n = \left(2.11\sqrt[3]{f'_c} + 7F\right) \left(\rho \frac{d}{a}\right)^{0.333} \text{ (MPa)} \quad (4.4)$$

$$v_n = \left(58.2\sqrt[3]{f'_c} + 1015F\right) \left(\rho \frac{d}{a}\right)^{0.333} \text{ (psi)}$$

For $a/d < 2.5$,

$$v_n = [\text{Eq. (4.4)}] \left(\frac{2.5}{a/d}\right) + v_b \left(2.5 - \frac{a}{d}\right) \text{ (MPa; psi)} \quad (4.5)$$

Model 2 (modified ACI equation)

$$v_n = \left(0.7\sqrt{f'_c} + 7F\right)\frac{d}{a} + 17.2\rho\frac{d}{a} \text{ (MPa)} \quad (4.6)$$

$$v_n = \left(8.4\sqrt{f'_c} + 1015F\right)\frac{d}{a} + 2494\rho\frac{d}{a} \text{ (psi)}$$

where f'_c = concrete compressive strength, MPa (psi);

a/d = shear span-to-depth ratio;

ρ = flexural reinforcement ratio;

F = fiber factor = $(L_f/D_f)V_f d_f$;

L_f = fiber length, mm (in.);

D_f = fiber diameter, mm (in.);

V_f = volume fraction of steel fibers;

d_f = bond factor = 0.5 for round fibers, 0.75 for crimped fibers, and 1 for indented fibers;

v_b = fiber pullout stress = $0.41\tau F$, MPa (psi); and

τ = average fiber matrix interface bond stress, taken as 4.15 MPa (600 psi), based on the recommendations of Swamy et al. [37].

(3) Kwak et al. [32]

$$v_n = 3.7e f_{sp}^{2/3} \left(\rho\frac{d}{a}\right)^{1/3} + 0.8v_b \text{ (MPa)} \quad (4.7)$$

$$v_n = 19.5e f_{sp}^{2/3} \left(\rho\frac{d}{a}\right)^{1/3} + 0.8v_b \text{ (psi)}$$

where e = arch action factor = 1 for $a/d > 3.4$; $e = 3.4d/a$ for $a/d \leq 3.4$;

f_{sp} = estimated using the splitting tensile strength of SFRC as shown in Equation (4.8);

$$f_{sp} = \frac{f_{cu}}{(20-\sqrt{F})} + 0.7 + 1.0\sqrt{F} \text{ (MPa)} \quad (4.8)$$

$$f_{sp} = \frac{f_{cuf}}{(20-\sqrt{F})} + 101.5 + 145\sqrt{F} \text{ (psi)}$$

a/d = shear span-to-depth ratio;

ρ = flexural reinforcement ratio;

F = fiber factor = $(L_f/D_f)V_f d_f$;

f_{cuf} = cube strength of fiber concrete = $1.2f'_c$, MPa (psi);

L_f = fiber length, mm (in.);

D_f = fiber diameter, mm (in.);

V_f = volume fraction of steel fibers;

d_f = bond factor = 0.5 for round fibers, 0.75 for crimped fibers, and 1 for indented fibers;

v_b = fiber pullout stress = $0.41\tau F$, MPa (psi); and

τ = average fiber matrix interface bond stress, taken as 4.15 MPa (600 psi), based on the recommendations of Swamy et al. [38].

(4) Khuntia et al. [33]

$$v_n = (0.167\alpha + 0.25F_1)\sqrt{f'_c} \text{ (MPa)} \quad (4.9)$$

$$v_n = (2\alpha + 3F_1)\sqrt{f'_c} \text{ (psi)}$$

where f'_c = concrete compressive strength, MPa (psi);

α = arch action factor = 1 for $a/d \geq 2.5$, and $\alpha = 2.5d/a \leq 3$ for $a/d < 2.5$;

F_1 = fiber factor = $\beta V_f (l_f/d_f)$;

L_f = fiber length, mm (in.);

D_f = fiber diameter, mm (in.);

V_f = volume fraction of steel fibers; and

β = factor for fiber shape and concrete type = 1 for hooked or crimped steel fibers, 2/3 for plain or round steel fibers with normal concrete, 3/4 for hooked or crimped steel fibers with lightweight concrete.

(5) Sharma [39]

$$v_n = kf'_t(d/a)^{0.25} \text{ (MPa)} \quad (4.10)$$

where a/d = shear span-to-depth ratio;

f'_t = tensile strength of concrete, MPa (psi);

$k = 1$ if f'_t is obtained by direct tension test;

$k = 2/3$ if f'_t is obtained by indirect tension test;

$k = 4/9$ if f'_t is obtained using modulus of rupture; or

$f'_t = 0.79(f'_c)^{0.5}$, MPa ($f'_t = 9.5(f'_c)^{0.5}$, psi); and

f'_c = concrete compressive strength, MPa (psi).

(6) Imam et al. [35]

$$v_n = 0.6\Psi^3\sqrt[3]{\omega} \left[(f'_c)^{0.44} + 275 \sqrt{\frac{\omega}{(a/d^5)}} \right] \text{ (MPa)} \quad (4.11)$$

$$v_n = 0.6\Psi^3\sqrt[3]{\omega} \left[16.2(f'_c)^{0.44} + 39875 \sqrt{\frac{\omega}{(a/d^5)}} \right] \text{ (psi)}$$

where f'_c = concrete compressive strength, MPa (psi);

a/d = shear span-to-depth ratio;

Ψ = size effect factor = $\frac{1+\sqrt{(5.08/d_a)}}{\sqrt{1+d/(25d_a)}}$, for mm $\frac{1+0.2\sqrt{(5.08/d_a)}}{\sqrt{1+d/(25d_a)}}$ for in.

ω = reinforcing factor = $\rho(1 + 4F)$;

F = fiber factor = $(L_f/D_f)V_f d_f$;

L_f = fiber length, mm (in.);

D_f = fiber diameter, mm (in.);

V_f = volume fraction of steel fibers; and

d_f = bond factor = 0.5 for smooth fibers, 0.9 for deformed fibers, and 1.0 for hooked fibers.

(7) Shin et al. [34]

For $a/d \geq 3.0$,

$$\begin{aligned}v_n &= 0.19f_{sp} + 93\rho \left(\frac{d}{a}\right) + 0.834v_b \text{ (MPa)} \\v_n &= 0.19f_{sp} + 13485\rho \left(\frac{d}{a}\right) + 0.834v_b \text{ (psi)}\end{aligned}\tag{4.12}$$

For $a/d < 3.0$,

$$\begin{aligned}v_n &= 0.22f_{sp} + 217\rho \left(\frac{d}{a}\right) + 0.834v_b \text{ (MPa)} \\v_n &= 0.22f_{sp} + 31465\rho \left(\frac{d}{a}\right) + 0.834v_b \text{ (psi)}\end{aligned}\tag{4.13}$$

where f_{sp} = estimated using the splitting tensile strength of SFRC as shown in Equation (4.14);

$$\begin{aligned}f_{sp} &= \frac{f_{cuf}}{(20-\sqrt{F})} + 0.7 + 1.0\sqrt{F} \text{ (MPa)} \\f_{sp} &= \frac{f_{cuf}}{(20-\sqrt{F})} + 101.5 + 145\sqrt{F} \text{ (psi)}\end{aligned}\tag{4.14}$$

a/d = shear span-to-depth ratio;

ρ = flexural reinforcement ratio;

F = fiber factor = $(L_f/D_f)V_f d_f$;

f_{cuf} = cube strength of fiber concrete = $1.2f'_c$, MPa (psi);

f'_c = concrete compressive strength, MPa (psi);

L_f = fiber length, mm (in.);

D_f = fiber diameter, mm (in.);

V_f = volume fraction of steel fibers;

d_f = bond factor = 0.5 for round fibers, 0.75 for crimped fibers, and 1 for indented fibers;

v_b = fiber pullout stress = $0.41\tau F$, MPa (psi); and

τ = average fiber matrix interface bond stress, taken as 4.15 MPa (600 psi), based on the recommendations of Swamy et al. [38].

(8) Li et al. [40]

For $a/d \geq 2.5$,

$$\begin{aligned}v_n &= 1.25 + 4.68 \left[(f_f f_t)^{3/4} \left(\rho \frac{d}{a} \right)^{1/3} d^{-(1/3)} \right] \text{ (MPa)} \\v_n &= 181 + 0.134 \left[(f_f f_t)^{3/4} \left(\rho \frac{d}{a} \right)^{1/3} d^{-(1/3)} \right] \text{ (psi)}\end{aligned} \quad (4.15)$$

For $a/d < 2.5$,

$$\begin{aligned}v_n &= 9.16 \left[(f_f)^{2/3} (\rho)^{1/3} (d/a) \right] \text{ (MPa)} \\v_n &= 48.3 \left[(f_f)^{2/3} (\rho)^{1/3} (d/a) \right] \text{ (psi)}\end{aligned} \quad (4.16)$$

where f_f = modulus of rupture = $2.5f_{cc}$, MPa (psi);

f_{cc} = tensile strength = $f_t(1 - V_f) + \alpha_1 \alpha_2 \tau V_f (L_f/D_f)$, MPa (psi);

f_t = tensile strength of concrete = $0.292\sqrt{f'_c}$, MPa ($3.5\sqrt{f'_c}$, psi) proposed by MacGregor et al. [41];

f'_c = concrete compressive strength, MPa (psi);

V_f = volume fraction of steel fibers;

L_f/D_f = steel fiber aspect ratio;

α_1 = coefficient representing the fraction of bond mobilized at first matrix cracking, taken as 0.5, based on the recommendation by Naaman and Reinhardt [42];

α_2 = efficient factor of fiber orientation in the uncracked state of the composite, taken as 0.1, based on the recommendation by Naaman and Reinhardt [42];

τ = average fiber matrix interface bond stress, taken as 4.15 MPa (600 psi), based on the recommendations of Swamy et al. [38];

a/d = shear span-to-depth ratio;

ρ = flexural reinforcement ratio; and d = beam depth, mm (in.).

The standard deviation or coefficient of variation is a good statistical indicator of consistent accuracy. The models by Narayanan and Darwish [31], by Ashour et al. [36], and by Shin et al. [34] showed lower standard deviations (average = 0.18) relative to other models (Table 4.12). The mean values of (v_u/v_n) indicate that the models by Ashour et al. [36] (model 1), and by Kwak et al. [32] have reasonable safety margins (about 25%), whereas the models by Ashour et al. [36] (model 2) and by Shin et al. [34] have small safety margins of 9%, on average. Particularly, for the model by Shin et al. [34], only one data point of (v_u/v_n) is much lower (0.84). Given the small number of data points, it is important that all 11 data points failing in shear or flexure-shear mode fall above the unity line. On the other hand, the models by Khuntia et al. [33] and by Sharma [39] are overly conservative or exhibit substantial scatter (Table 4.12).

The slope (steepness) of the linear regression line for (v_u/v_n) ratios is one statistical indicator to evaluate the sensitivity of the dependable variable (v_u/v_n) to each independent variable. Table 4.13 indicates that the models by Narayanan and Darwish [31], Ashour et al. [36] (model 1), Kwak et al. [32] and Shin et al. [34] are overall satisfactory in terms of sensitivity, and the model by Ashour et al. [36] (model 1) gives the best results (Table 4.13). Based on this review, the following design shear strength equation is proposed for SFRLC beams, which is the modified version of the SFRC equations developed by Ashour et al. [36] (model 1).

$$v_n = \left(2.11^3 \sqrt{\lambda^2 f'_c} + 7F\right)^3 \sqrt{\rho \frac{d}{a}} \text{ (MPa)} \quad \text{for } (a/d) \geq 2.5 \quad (4.17)$$

$$v_n = [\text{Eq. (1)}] \left(\frac{2.5}{a/d}\right) + v_b \left(2.5 - \frac{a}{d}\right) \text{ (MPa)} \quad \text{for } (a/d) < 2.5 \quad (4.18)$$

where f'_c is the cylinder concrete strength of SFRLC in MPa, ρ is the flexural reinforcement ratio, v_b is the fiber pullout stress ($= 0.41 \tau F$), and τ is taken as 4.15λ MPa (0.6λ ksi). The constant value of 4.15 was based on the recommendations by Li et al. [40], Swamy et al. [38], and Kwak et al. [32]. The fiber factor (F) was defined earlier in the report as equal to $(L_f/D_f)V_f d_f$ (see Figure 4.4 for notations), where d_f is the bond factor ($= 0.75$ for both crimped and hooked fibers that were used for the prior (Swamy et al. [10]) and current specimens, respectively). For psi units, the coefficients of 2.11 and 7 in Equation (4.17) are replaced by 58.1 and 1,015, respectively. The model of Equations (4.17) and (4.18) empirically considers the arch action, which tends to occur when (a/d) is less than about 2.5 to 3.4 for SFRC beams (Narayanan and Darwish [31]; Kwak et al. [32]; Shin et al. [34]; Li et al. [40]). For more details on the original SFRC model, the reader is referred to the paper by Ashour et al. [36]. The models by Narayanan and Darwish [31] and Kwak et al. [32], with a consideration of lightweight concrete effects, are also reasonable and acceptable.

Figure 4.13 illustrates the distributions of (v_u/v_n) ratios against four different independent variables, showing that the proposed model is not overly sensitive to the variation of these four main variables. Furthermore, Figure 4.13 depicts that the proposed model corresponds well to the current and prior data (Swamy et al. [10]) of SFRLC beams, in terms of the prediction (mean = 1.25), consistency (standard deviation = 0.12), safety (minimum = 1.06) and structural efficiency (maximum = 1.46).

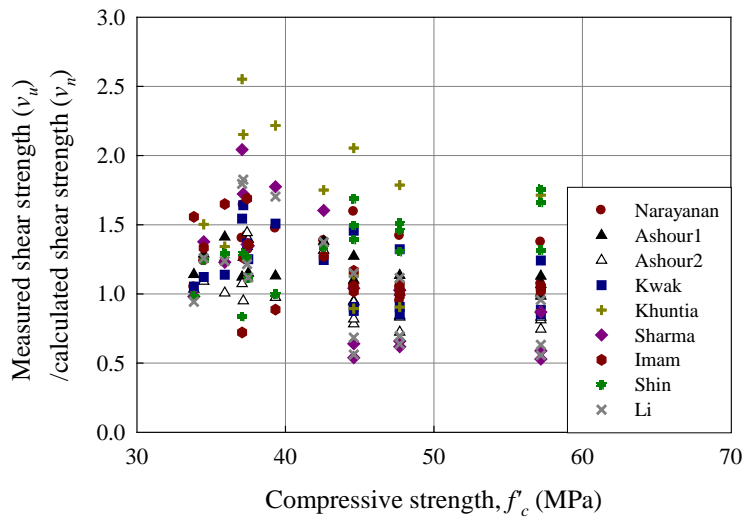
It is noted that the model developed in this final report is the earlier version of the model presented in the paper by Kang et al. [43], where more detailed information is provided.

Table 4.12. Comparisons of Measured Peak Shear Strengths and Shear Strength Capacities Calculated Based on The Available SFRC Shear Strength Models Except for the Replacement of f'_c by $\lambda^2 f'_c$ for SFRLC Beams

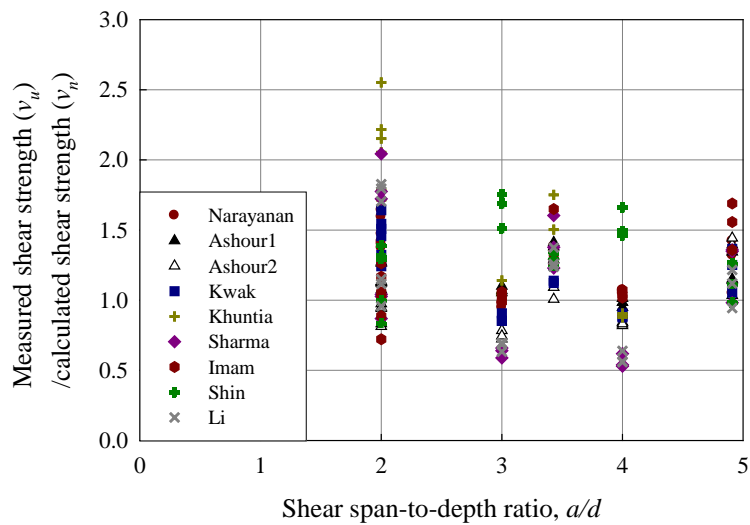
Specimen	FLB-0.5-2	FLB-0.75-2	FLB-0.5-3	FLB-0.75-3	FLB-0.5-4	FLB-0.75-4	1TLF-1	1TLF-2	1TLF-3	2TLF-1	2TLF-2	2TLF-3	3TLF-1	3TLF-2	3TLF-3	Mean	St. dev.	
	0.5	0.75	0.5	0.75	0.5	0.75	1.0	1.0	1.0	1.0	1.0	1.0	1.0	1.0	1.0	NA	NA	
Peak shear strength (MPa)	3.08	3.14	1.71	1.82	1.34	1.59	5.51	4.05	2.92	4.93	3.13	2.94	4.65	2.85	2.02	NA	NA	
Narayanan & Darwish (1987)																		
	1.77	1.57	1.18	1.07	1.21	1.18	1.40	1.38	1.32	1.47	1.24	1.42	1.64	1.23	1.05	1.34	0.21	
Ashour et al. (1992)																		
(1)	1.39	1.23	1.22	1.16	1.06	1.12	1.14	1.42	1.18	1.15	1.33	1.39	1.30	1.46	1.18	1.25	0.12	
(2)	1.06	0.93	0.90	0.82	0.94	0.96	1.09	1.35	1.44	1.00	1.13	1.50	0.98	1.05	1.08	1.08	0.20	
Kwak et al. (2002)																		
	1.66	1.49	1.04	0.97	1.01	1.03	1.54	1.24	1.25	1.51	1.12	1.37	1.64	1.14	1.05	1.27	0.24	
Khuntia et al. (1999)																		
	2.06	1.83	1.38	1.26	1.10	1.11	2.38	1.87	1.45	2.11	1.63	1.48	2.09	1.47	1.08	1.62	0.42	
Sharma (1986)																		
	1.24	1.22	0.78	0.80	0.66	0.76	2.13	1.72	1.46	1.89	1.49	1.48	1.87	1.35	1.08	1.33	0.46	
Imam et al. (1997)																		
	1.24	1.08	1.18	1.10	1.17	1.23	0.73	1.31	1.42	0.90	1.38	1.79	1.29	1.73	1.66	1.28	0.29	
Shin et al. (1994)																		
	1.19	1.13	1.30	1.22	1.13	1.16	0.84	1.37	1.15	1.01	1.29	1.32	1.32	1.35	1.03	1.19	0.15	
Li et al. (1992)																		
	1.05	1.04	0.95	0.99	0.77	0.90	1.24	1.93	1.52	1.28	1.68	1.62	1.51	1.62	1.20	1.29	0.34	

Table 4.12. Steepness (Slope) of the Linear Regression Line for the Ratio of Measured Peak Shear Strength (v_u) to Calculated Shear Strength (v_n), with the Consideration of Lightweight Concrete Factor ($\lambda = 0.75$)

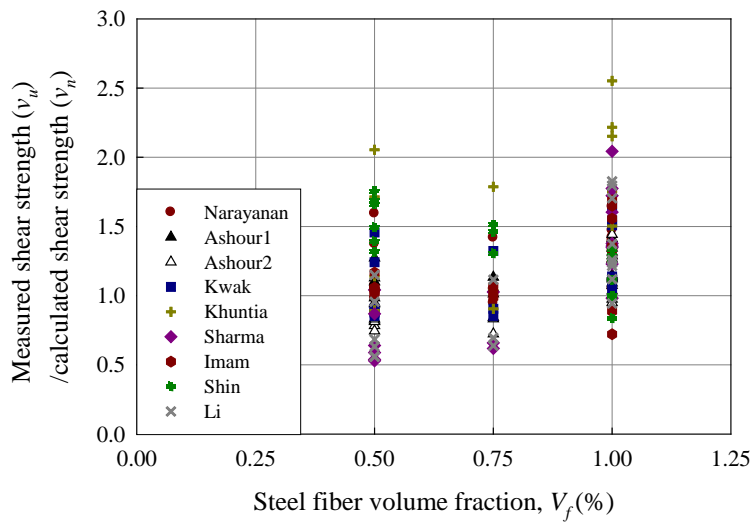
Independent variable		f'_c (MPa)	a/d	V_f (%)	ρ (%)	d (mm)
Narayanan and Darwish (1987)		0.0019	0.1129	0.0266	0.0188	0.0008
Ashour et al. (1992)		(1)	0.0073	0.0033	0.1621	0.0081
		(2)	0.0192	0.0954	0.5105	0.1245
Absolute slope of linear regression line for each (v_u/v_n) data set	Kwak et al. (2002)	0.0072	0.138	0.2228	0.0475	0.0008
	Khuntia et al. (1999)	0.0144	0.2859	0.5407	0.1542	0.0094
	Sharma (1986)	0.0529	0.1512	1.5893	0.2641	0.0179
	Imam et al. (1997)	0.0257	0.1857	0.397	0.0403	0.0050
	Shin et al. (1994)	0.0017	0.0244	0.0318	0.3568	0.0006
	Li et al. (1992)	0.0437	0.0511	1.2977	0.1791	0.0094



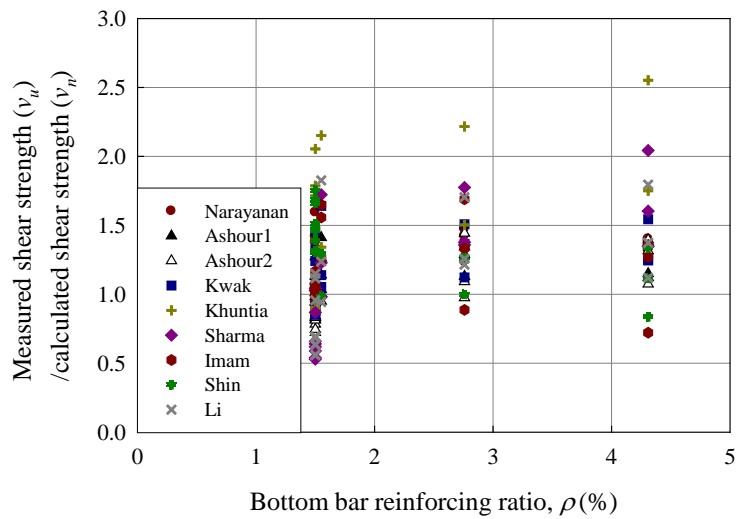
(a) Measured Shear Strength (v_u) / Calculated Shear Strength (v_n)
versus Compressive Stress (f'_c)



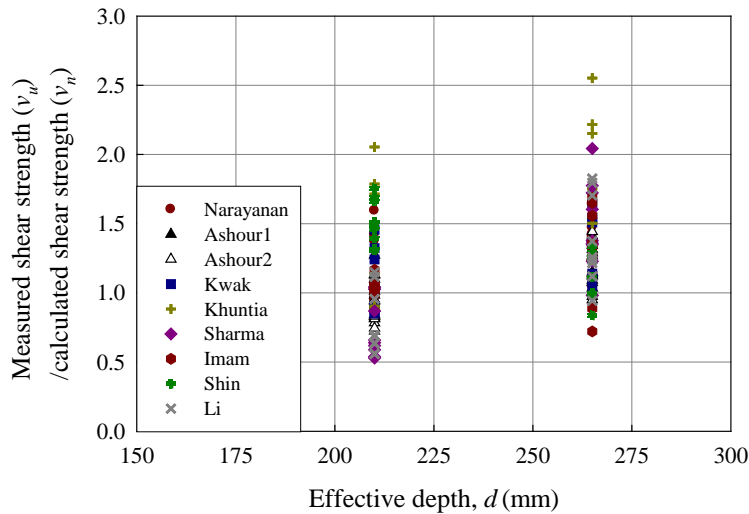
(b) Measured Shear Strength (v_u) / Calculated Shear Strength (v_n) versus Shear Span-to-Depth Ratio (a/d)



(c) Measured Shear Strength (v_u) / Calculated Shear Strength (v_n) versus Steel Fiber Volume Fraction (V_f)



(d) Measured Shear Strength (v_u) / Calculated Shear Strength (v_n) versus Bottom Bar Reinforcing Ratio (ρ)



(e) Measured Shear Strength (v_u) / Calculated Shear Strength (v_n) versus Effective Depth (d)

Figure 4.13. Measured Shear Strength (v_u) / Calculated Shear Strength (v_n) versus Main Parameters (Conversion: 1 MPa = 145 psi; 1 mm = 0.039 in.)

4.5 SUMMARY

To investigate the effect of steel fibers on the shear strength of lightweight concrete beams without web reinforcement, a total of 12 beams were tested under four point loads, including six SFRLC beams, three SFRC beams and three Lightweight RC beams. The primary variables included the shear span-to-depth ratio (2, 3, and 4), steel fiber volume fraction ($V_f = 0, 0.5, \text{ and } 0.75\%$) and type of concrete (lightweight vs. normalweight). The addition of steel fibers with V_f of 0.75% was found to increase the shear capacity by 30% and promote a ductility of 5.3 or higher. Test results also indicated that the shear span-to-depth ratio adversely affects the shear capacity. The beams with the combination of either ($V_f = 0.75\%$ and $a/d = 4$) or ($V_f = 0.5\%$ and $a/d = 3$) performed equally well. Finally, combining prior studies with this study led to the design of a shear strength equation for SFRLC beams which corresponded well to existing data with substantial precision and repeatability.

This Page Is Intentionally Blank

5. LARGE SCALE TESTING AND ANALYSIS OF PRESTRESSED SELF-CONSOLIDATING CONCRETE BEAMS

5.1 INTRODUCTION

Structural concrete is used for reinforced concrete and prestressed concrete. In the former, mild steel is embedded into the concrete, mainly to provide tension resistance, a property lacking in concrete. However, a very large section size is often required for normal reinforced concrete members to solve the issue of excessive deflection, which results in higher construction costs. More compact and cost-efficient structures were made possible through the development of prestressed concrete, which is the result of improvements in concrete compressive capacity and the application of high-strength steel. Additionally, Self-Consolidating-Concrete (SCC) is becoming an increasingly popular construction material due to reduced labor costs (i.e., vibration is not needed to settle the concrete) and its improved construction quality (Hwang et al. [44]).

Furthermore, lightweight aggregates and steel fibers are becoming popular materials for concrete construction. This study attempts to investigate these relatively recent technologies by studying the prestressed SCC members with and without steel fibers and/or lightweight aggregates.

In this study, a total of five prestressed concrete specimens consisting of four reduced-scale (about half-scale) SCC beams and a full-scale Type-II AASHTO (American Association of State Highway and Transportation Officials) SCC bridge girder are tested. Numerical modeling results produced by a team effort (Kim et al. [45]) are also compared with the experimental results.

5.2 EXPERIMENTAL PROGRAM AND RESULTS

5.2.1 Test Specimen Design

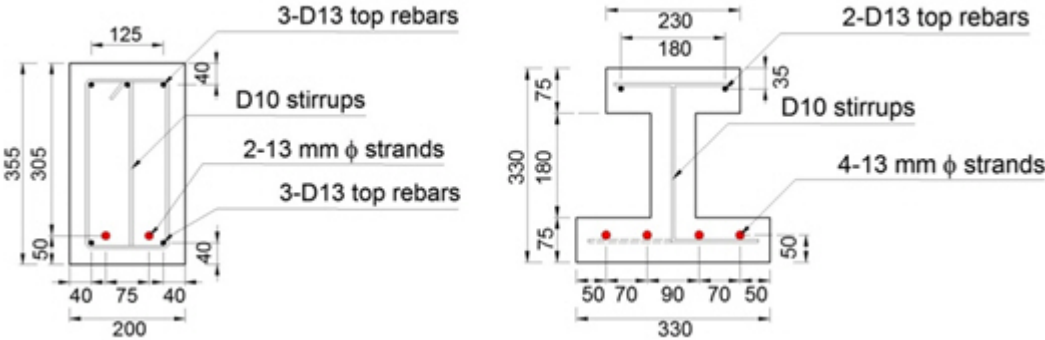
Five prestressed concrete members were designed in accordance with the ACI 318-08 building design code (ACI [17]) and AASHTO Load Resistance Factor Design (LRFD) Bridge Design Specification (AASHTO [46]). Of these, four lightweight concrete members ($R1$, $R2$, $I1$, $I2$) were reduced-scale, prestressed SCC beams, and one normalweight concrete member ($G1$) was a full-scale prestressed SCC girder (Figure 5.1). A rectangular section was used for members $R1$ and $R2$, whereas an I-shaped section was used for $I1$, $I2$ and $G1$. The girder $G1$ was a standard Type II AASHTO girder. Additionally, steel fibers were added to $R2$ and $I2$, with a dosage rate of 40 kg/m^3 (65 lbs/yd^3). To provide pre-compression to the concrete, Grade 270 low-relaxation seven-wire strands were pre-tensioned to the designed pre-stress level ($f_{pe} = \sim 0.7 f_{pu}$) prior to concrete casting. The design was then confirmed through preliminary computer simulations to achieve the desired level of flexural performance.

Each member section is indicated in Figure 5.1. A straight strand profile was used for all specimens. The span lengths of the reduced-scale and full-scale members were 5.2 m (17 ft) and 7.5 m (24.5 ft), respectively. Members $R1$ and $R2$ had nominally identical cross-sectional dimensions ($200 \times 355 \text{ mm}$; $8 \times 14 \text{ in.}$) and effective depths (320 mm ; 12.5 in.). The longitudinal reinforcement consisted of two 13 mm ($\frac{1}{2} \text{ in.}$) diameter seven-wire strands, two D13 or No. 4 (diameter = 13 mm; 0.5 in.) Grade 60 deformed bars (for tension reinforcement) and three D19 or No. 6 (diameter = 19 mm; 0.75 in.) Grade 60 deformed bars (for compression reinforcement). For $I1$ and $I2$, the longitudinal reinforcement consisted of four 13 mm ($\frac{1}{2} \text{ in.}$) diameter seven-wire strands (for tension reinforcement) and two D13 or No. 4 Grade 60 deformed bars (for compression reinforcement), as shown in Figures 5.1(a) and 5.1(b).

The cross-sectional view of member $G1$ is also shown in Figure 5.1(c). Ten 15 mm (0.6 in.) diameter seven-wire strands and two 15 mm (0.6 in.) diameter seven-wire strands

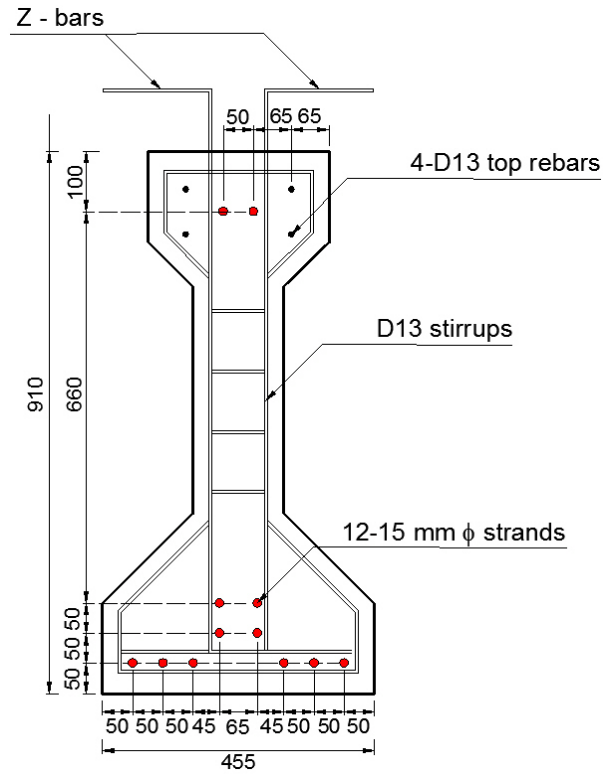
were provided in the bottom and top flanges, respectively. Four D13 or No. 4 Grade 60 deformed bars were placed at the top as additional compression steel.

D10 or No. 3 (diameter = 10 mm; 3/8 in.) stirrups were included, as shown in Figure 5.2, along the entire span of all specimens. The rectangular beams of *R1* and *R2* were designed to have a highly confined core unlike the I-shaped beams of *I1* and *I2*. Note that hooks are provided only for the stirrups of *R1* and *R2*. Note that hooks were provided only for the stirrups of *R1* and *R2*. The spacing of shear reinforcement varies along the length of the beam or girder, as shown in Figure 5.2.



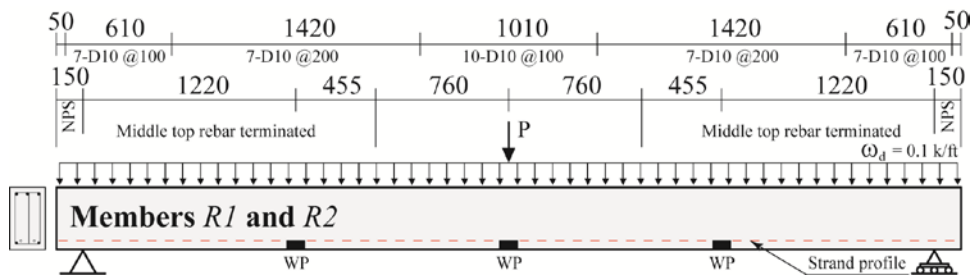
(a) *R1* and *R2* Specimen

(b) *I1* and *I2* Specimen

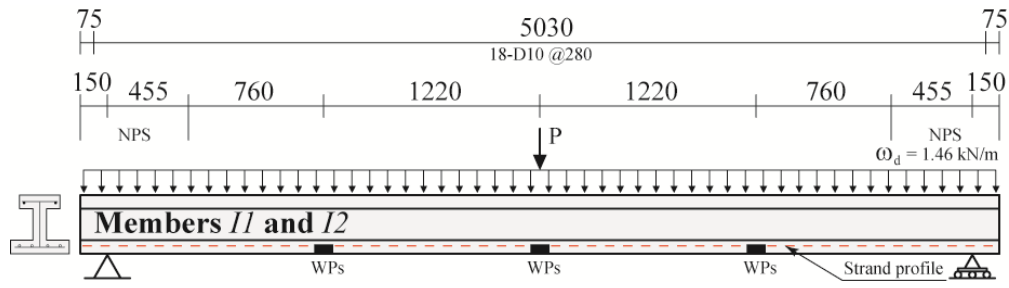


(c) G1 specimen

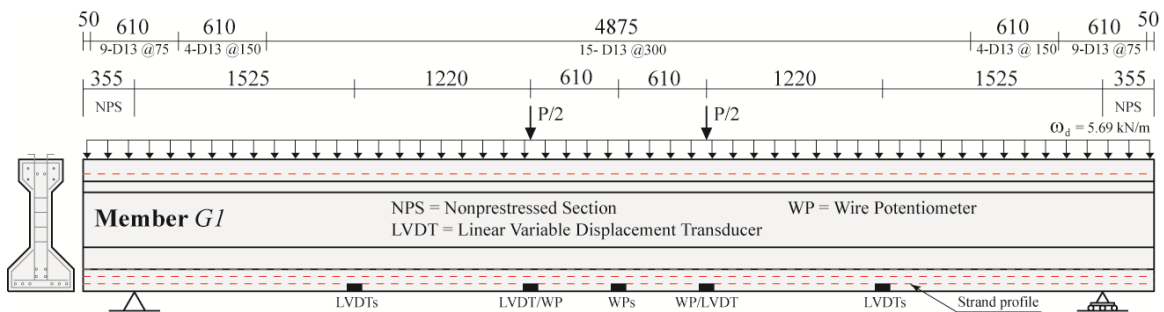
Figure 5.1. Details of Prestressed SCC Member Sections (Conversion: 1 mm = 0.039 in.)



(a) R1 and R2



(b) *I1 and I2*



(c) *G1*

Figure 5.2. Elevations of the Prestressed Members (Conversion: 1 mm = 0.039 in.)

5.2.2 Material and Mixture Properties

High early-strength cement (Type III) was used in the concrete mixtures. Two kinds of coarse aggregates were selected. The first was expanded shale lightweight aggregate used for the four reduced-scale prestressed lightweight SCC beams. The second was 13 mm (0.5 in.) nominal diameter stone used for the full-scale prestressed normalweight concrete girder. Washed river sands were used as fine aggregates for all specimens. The unit weights of lightweight and normalweight concrete were about 1,840 kg/m³ (115 pcf) and 2,400 kg/m³ (150 pcf), respectively.

Table 5.1 presents SCC mixture proportions. Chemical admixtures such as a High-Range Water-Reducing (HRWR) admixture and a Viscosity-Modifying Admixture (VMA)

or an Accelerating Admixture (AA) were used to control the fluidity and viscosity of the SCC mixes. The HRWR was used to increase concrete workability and help achieve high early compressive strengths. In order to optimize the mix to flow without segregation and bleeding, the VMA and AA were used for lightweight and normalweight concrete mixtures, respectively. Additionally, retarder was used for lightweight concrete to improve workability and reduce segregation. The workability of the SCC mixture was examined using a slump flow test (see Figure 5.3). The diameter of the slump flow for the SCC mixture ranged from 520 to 675 mm (20.5 to 26.5 in.).



Figure 5.3. Slump Flow Test

Table 5.1. SCC Mixture Proportions

Materials	<i>R1</i>	<i>R2</i>	<i>I1</i>	<i>I2</i>	<i>G1</i>
Cement, kg/m ³ (lb/yd ³)	474 (800)	474 (800)	474 (800)	474 (800)	553 (933)
Coarse aggregate (CA), kg/m ³ (lb/yd ³)	356 (600)	356 (600)	356 (600)	356 (600)	814 (1373)
Fine aggregate (FA), kg/m ³ (lb/yd ³)	842 (1420)	842 (1420)	842 (1420)	842 (1420)	873 (1473)
CA/FA ratio	0.42	0.42	0.42	0.42	0.93
Water-cement ratio (<i>w/c</i>)	0.31	0.31	0.31	0.31	0.28
HRWR [†] , mL/m ³ (fl oz/yd ³)	3120 (80)	3120 (80)	3120 (80)	3120 (80)	4290-5850 (110-150)
AA ^{††} , mL/m ³ (fl oz/yd ³)	0	0	0	0	351-1170 (9-30)
VMA, mL/m ³ (fl oz/yd ³)	936 (24)	936 (24)	936 (24)	936 (24)	0
Retarder [‡] , mL/m ³ (fl oz/yd ³)	312 (8)	312 (8)	312 (8)	312 (8)	0
Steel fiber, kg/m ³ (lb/yd ³)	0	40 (65) (<i>V_f</i> = 0.5%)	0	40 (65) (<i>V_f</i> = 0.5%)	0

[†]: Type F, ASTM C 494/C 494M-99; ^{††}: Type C, ASTM C 494/C 494M-99;

[‡]: Type B, ASTM C 494/C 494M-99;

Conversion: 1 kg/m³ = 1.667 lb/yd³; 1 mL/m³ = 0.0256 fl oz/yd³

Table 5.2 summarizes the measured properties of each concrete mix. The design material properties of the full-scale girder are reported, as the girder was obtained from the fabricator without preparation of material test coupons. For the reduced-scale beams, results from the test coupons are provided in Table 5.2. Concrete compressive strength (f'_c) was obtained using 150 × 300 mm (6 × 12 in.) cylinders in accordance with the American Society for Testing and Materials (ASTM) C39/C39M standards (ASTM [14]). The modulus of rupture (f_r) was evaluated from three-point bending tests of 150 × 150 × 530 mm (6 × 6 × 20 in.) concrete prisms in accordance with ASTM C78 (ASTM [14]). The specimen was loaded continuously at a rate of 6.67 to 9.33 kN/min (1500 to

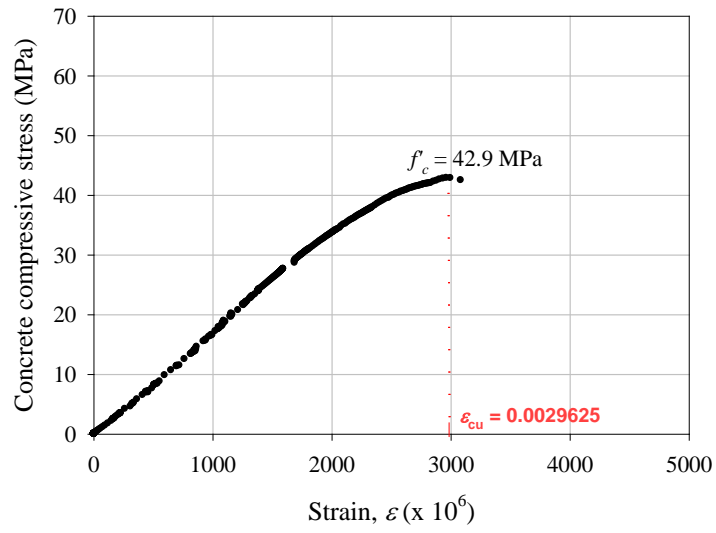
2100 lb/min) until a tensile failure occurred. All cylinder and prism specimens were tested at 28 days after casting (also just prior to structural testing).

The compressive strength (f'_c) and modulus of rupture (f_r) of the SCC with steel fibers were higher than those of the SCC without steel fibers by about 30% and 5%, respectively (see Figures 5.4 to 5.7).

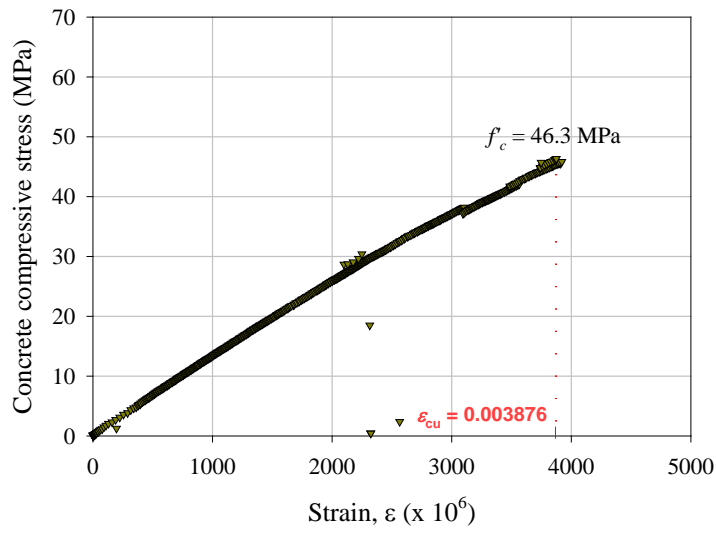
Table 5.2. Fresh and Hardened Concrete Properties for SCC Mixtures

Material properties	<i>R1</i>	<i>R2</i>	<i>I1</i>	<i>I2</i>	<i>G1</i>
Slump flow, mm (in.)	673 (26.5)	521 (20.5)	673 (26.5)	521 (20.5)	686 (27)
Early compressive strength (f'_{ci}), MPa (psi)	31.3 (4,538)	31.8 (4,616)	31.3 (4,538)	31.8 (4,616)	NA
Compressive strength (f'_c), MPa (psi)	41.1 (5,959)	54.1 (7,845)	41.1 (5,959)	54.1 (7,845)	41.4 (6,000)
Modulus of rupture (f_r), MPa (psi)	5.7 (826)	6 (872)	5.7 (826)	6 (872)	4 [†] (581)

[†]: $f_r = 0.6\sqrt{f'_c}$ (MPa); $f_r = 7.5\sqrt{f'_c}$ (psi); NA: Not Available

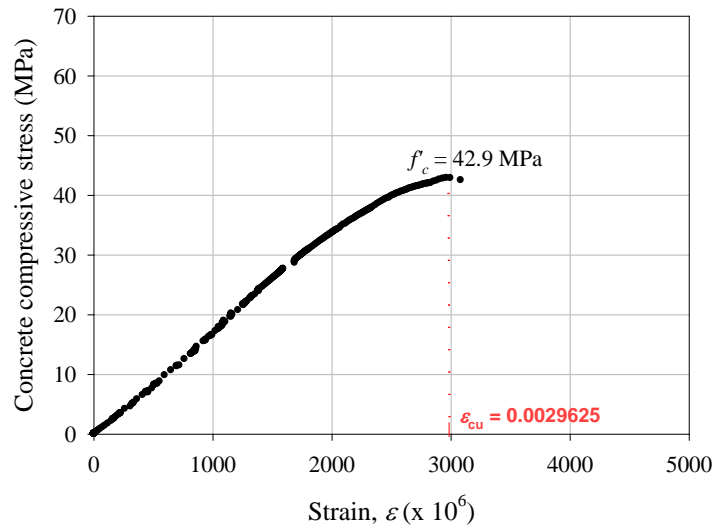


(a) Cylinder 1

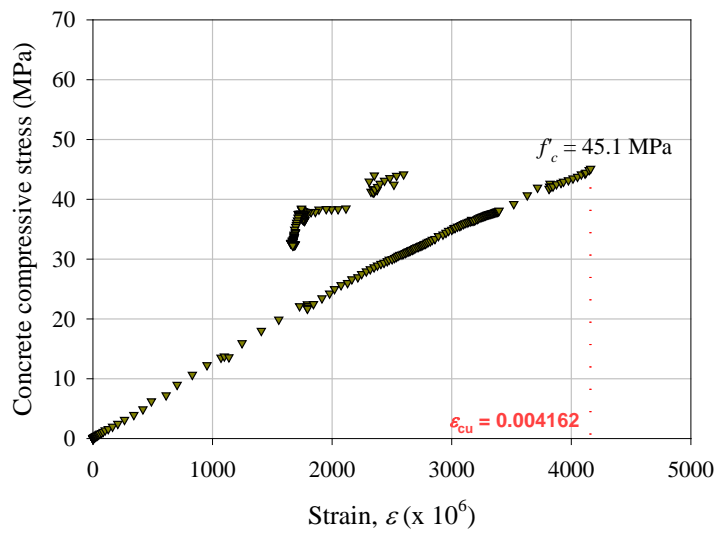


(b) Cylinder 2

Figure 5.4. Concrete Stress-Strain Curves for *R1* and *I1* (Conversion: 1 MPa = 145 psi)

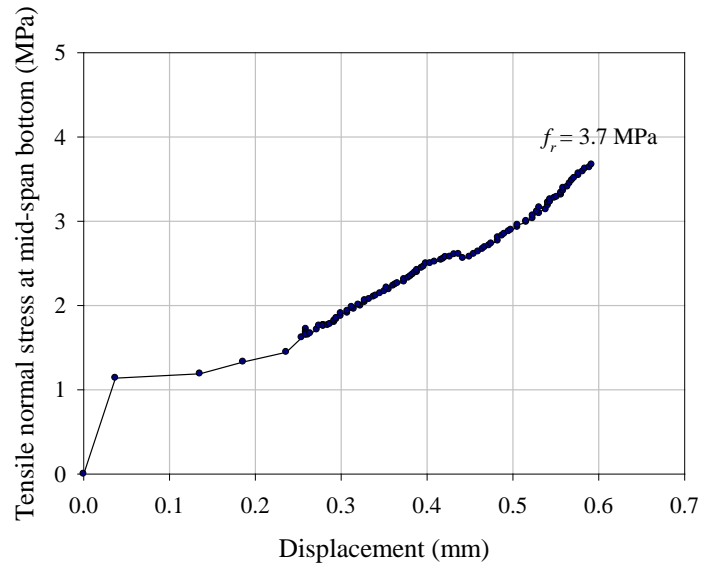


(a) Cylinder 1

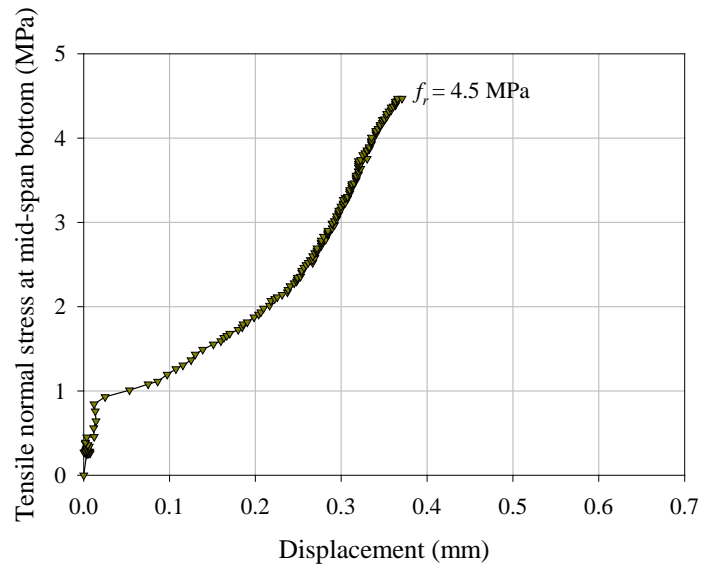


(b) Cylinder 2

Figure 5.5. Concrete Compressive Stress-Strain Curves for *R2* and *I2*
(Conversion: 1 MPa = 145 psi)



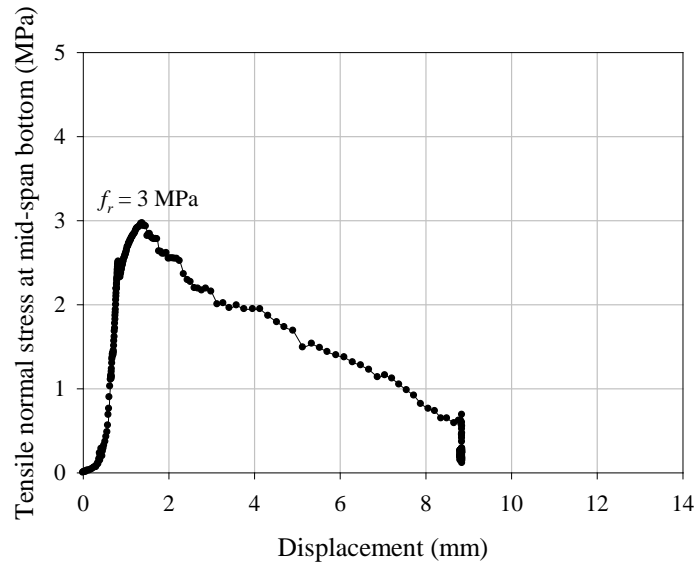
(a) Prism 1



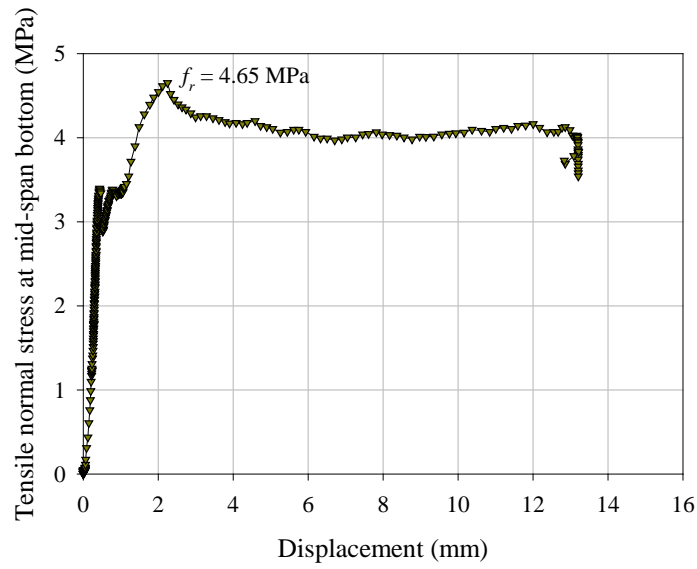
(b) Prism 2

Figure 5.6. Tensile Normal Stress at Mid-Span Bottom versus Prism Displacement Relationships for *R1* and *I1*

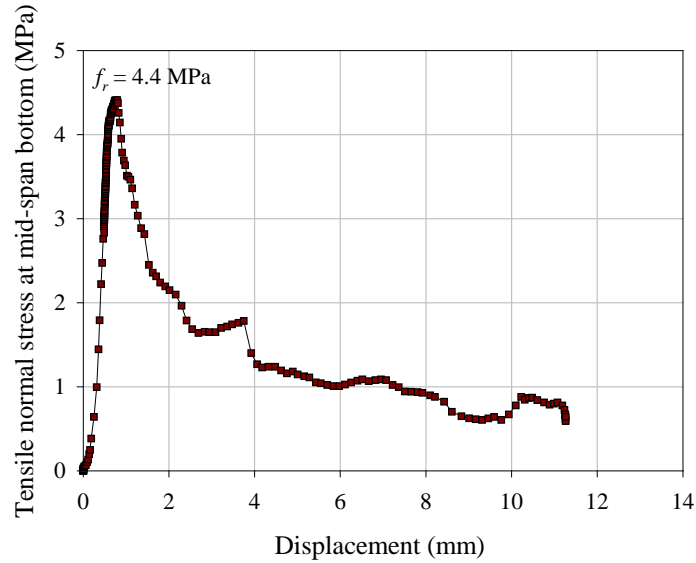
(Conversion: 1 MPa = 145 psi; 1 mm = 0.039 in.)



(a) Prism 1



(b) Prism 2

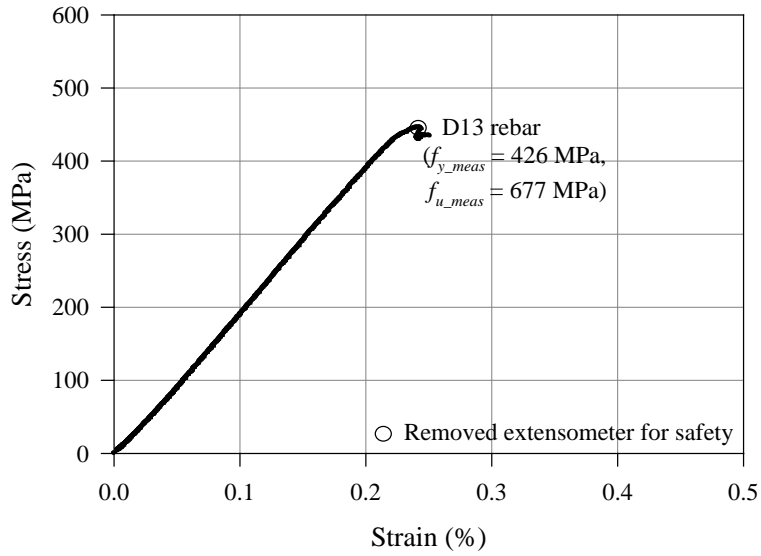


(c) Prism 3

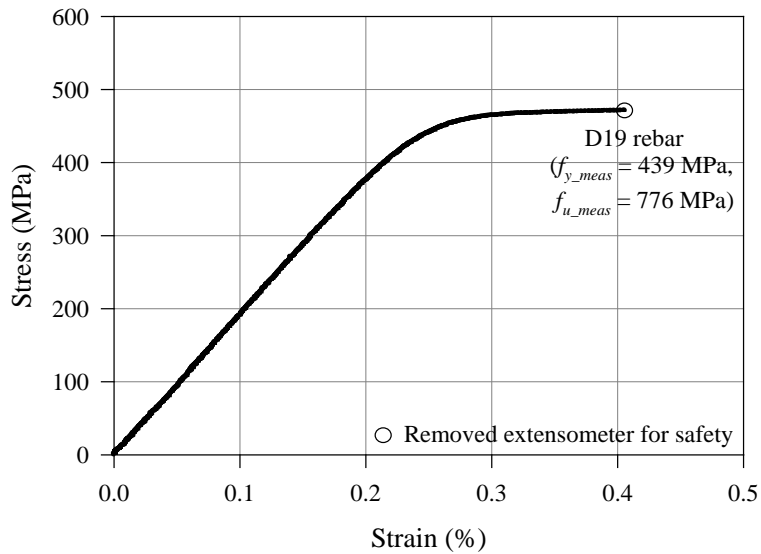
Figure 5.7. Tensile Normal Stress at the Mid-Span Bottom versus Prism Displacement Relationships for *R2* and *I2*

(Conversion: 1 MPa = 145 psi; 1 mm = 0.039 in.)

Because of construction constraints, steel material properties were available only for the reduced-scale beams. The D13 (No. 4) and D19 (No. 6) longitudinal deformed bars used for the reduced-scale beams had measured yield strengths (f_{y_meas}) of 426 MPa (61.8 ksi) and 439 MPa (63.7 ksi) and ultimate strengths (f_{u_meas}) of 677 MPa (98.1 ksi) and 776 MPa (112.5 ksi), respectively (see Figure 5.8). Two 13 mm (0.5 in.) diameter pre-stressing seven-wire strands for these specimens had measured tensile strengths (f_{pu_meas}) of 1847 MPa (267.8 ksi) and 1908 MPa (276.7 ksi), respectively (see Figure 5.9). Hooked steel fibers with a length of 60 mm (2.4 in.), diameter of 0.8 mm (0.03 in.) and specified tensile strength of 1035 MPa (150 ksi) were used for *R2* and *I2*.

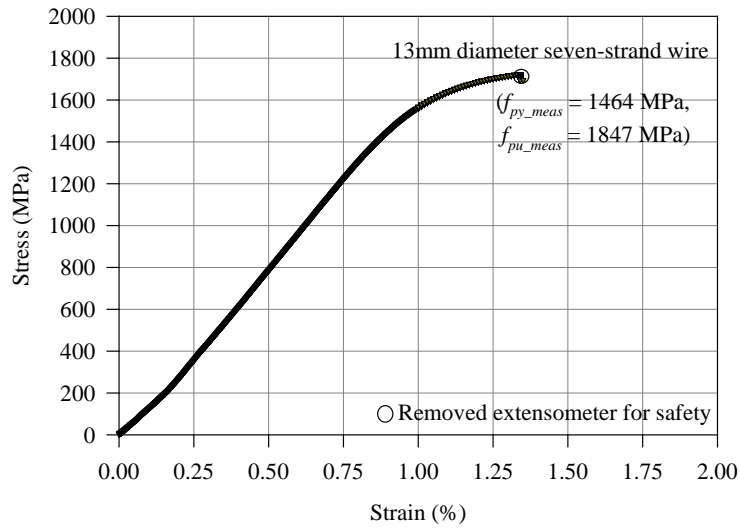


(a) Longitudinal Deformed Bar (D13; No. 4)

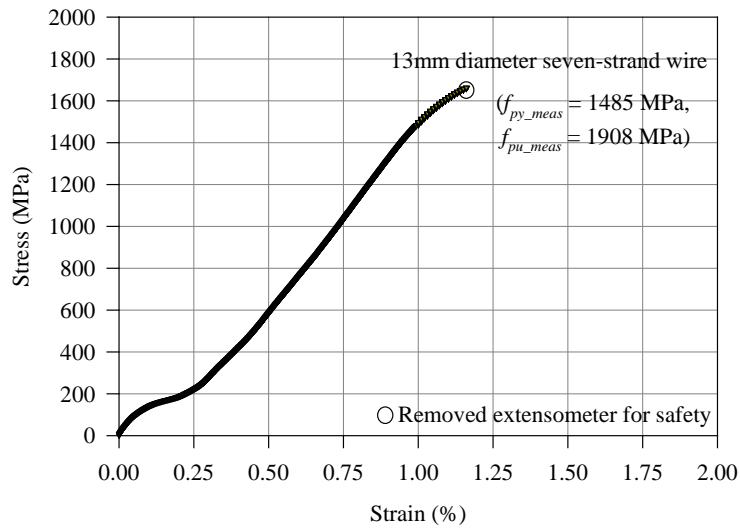


(b) LONGITUDINAL Deformed Bar (D19; No. 6)

Figure 5.8. Stress-Strain Relationships for Longitudinal Deformed Bars
 (Conversion: 1 MPa = 0.145 ksi)



(a) Prestressing Steel Strand 1



(b) Prestressing Steel Strand 2

Figure 5.9. Stress-Strain Relationships for Prestressing Steel Strands
 (Conversion: 1 MPa = 0.145 ksi)

5.2.3 Fabrication of Test Specimens

All test specimens were fabricated on parallel pre-stressing beds in a PCI (Precast/Prestressed Concrete Institute)-certified plant. After the side forms for each member were positioned, the pre-stressing strands were placed through the length of the members and prestressed using a hydraulic jack (see Figure 5.10). The stretching of the strands was monitored using a pressure gauge to determine exactly how far the strands were stretched. The SCC was cast without vibration. Before the pre-stressing strands were cut with an electric arc welder at each end of the member, three concrete cylinders per member were tested to verify that the concrete had achieved a compressive strength of 29 MPa (4200 psi), which was indicative that it could handle the pre-stressing stress that the strands would place on the member. After five days, the early compressive strength of the concrete (f'_{ci}) was 31.6 MPa (4580 psi) on average, which was just enough for the members to be removed from the pre-stressing bed (see Table 5.2).



(a) Prestressing of 13 mm ($\frac{1}{2}$ in.) Diameter Low Relaxation Strands with A Hydraulic Jack

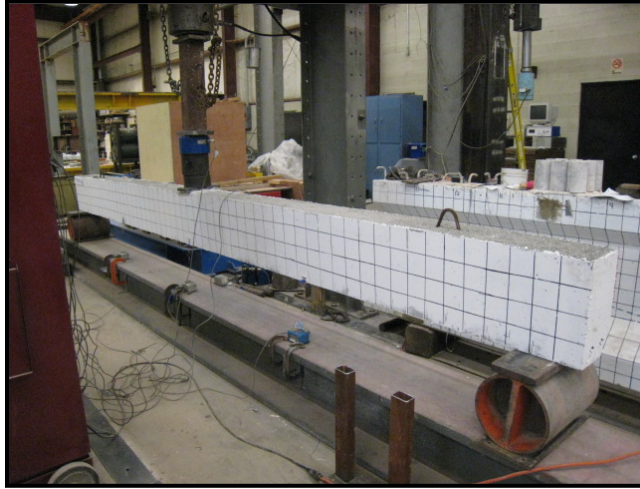


(b) Monitoring the Gauge Pressure of the Jack

Figure 5.10. Prestressing of 13 mm ($\frac{1}{2}$ in.) Diameter Low Relaxation Strands with a Hydraulic Jack at CORESLAB Structures, Inc., Oklahoma City, Oklahoma

5.2.4 Testing, Test Setup and Instrumentation

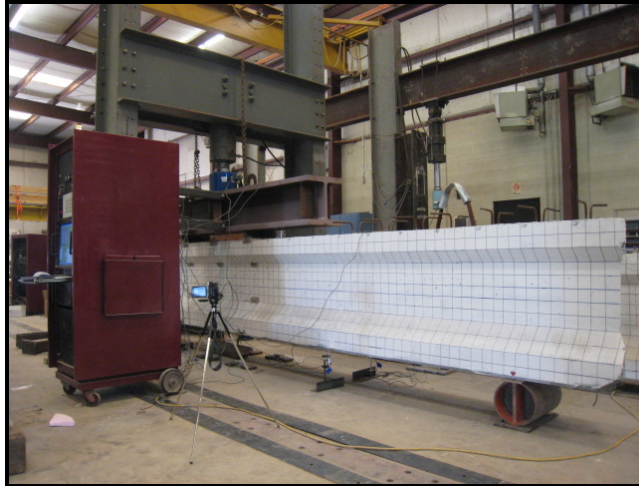
All the experimental simulations were conducted in the Donald G. Fears Structural Engineering Laboratory to investigate the nonlinear flexural behavior of prestressed concrete members made of SCC. Members *R1*, *R2*, *I1*, and *I2* were subjected to a three-point bending test, while a four-point bending test was applied to member *G1*. The experimental setup is shown in Figure 5.11. The simply supported method was adopted, and the center-to-center span lengths were 4.9 m and 6.7 m (16 and 22 ft) for the reduced-scale beams (*R1*, *R2*, *I1*, *I2*) and the full-scale girder (*G1*), respectively. Loading was applied through a hydraulic cylinder.



(a) *R1* Specimen



(b) *I1* Specimen



(c) *G1* Specimen

Figure 5.11. Test Setup at the Donald G. Fears Engineering Laboratory in OU

A compression-tension load cell was used to measure the applied loads, while Wire Potentiometers (WPs) and Linear Variable Differential Transducers (LVDTs) were used to measure deflections at several locations (see Figure 5.11). Data of the applied loads and deflections were collected using a data acquisition system at a 1-Hz sampling rate. The distance between the loading point and nearest support was 2.4 m (96 in.) for the reduced-scale beams, and 2.7 m (108 in.) for the full-scale girder.

5.2.5 Observations and Overall Test Results

No cracking was seen at the initial loading stage. With increased loading of the members, flexural cracks were observed in the tensile region (at the bottom-fibers). The load and center displacement corresponding to the occurrence of the first cracking are indicated in Table 5.3. The first cracking of *R1* and *R2* occurred at the loads of 56.7 kN (12.8 kips) and 64.5 kN (14.5 kips), respectively. For *I1* and *I2*, it occurred at the higher loads of 93 kN (21 kips) and 88.9 kN (20 kips), respectively. The load at first cracking for the full-scale girder *G1* was 854 kN (192 kips).

With increasing load, the flexural cracks propagated from the bottom to the top of the member (Figure 5.12(a) and 5.12(b)) and nonlinear behavior was observed. The members finally failed by concrete crushing at the top-fiber near the region of loading (see Figures 5.12(a) and 5.12(c)), except for *I1* where bond delamination occurred due to a lack of concrete cover for pre-stressing strands (Figure 5.12(b)). Applied loads at ultimate were recorded as 113, 121, 103 and 137 kN (25.4, 27.3, 23.2 and 30.8 kips) for *R1*, *R2*, *I1*, and *I2*, respectively. Their corresponding deflections were 105, 137, 38 and 51 mm (4.1, 5.4, 1.5 and 2 in.). The strength of *I1* was much lower than that of *I2* even with the same cross section, reinforcing and materials; this was likely due to early bond delamination. The addition of steel fibers in *R2* increased the flexural strength by about 8% compared with *R1* (Figure 5.13(a)). For *G1*, a load of about 1780 kN (400 kips), and its corresponding deflection of 38 mm (1.5 in.), were monitored at ultimate, exhibiting excellent ductility (Figure 5.13(b)).

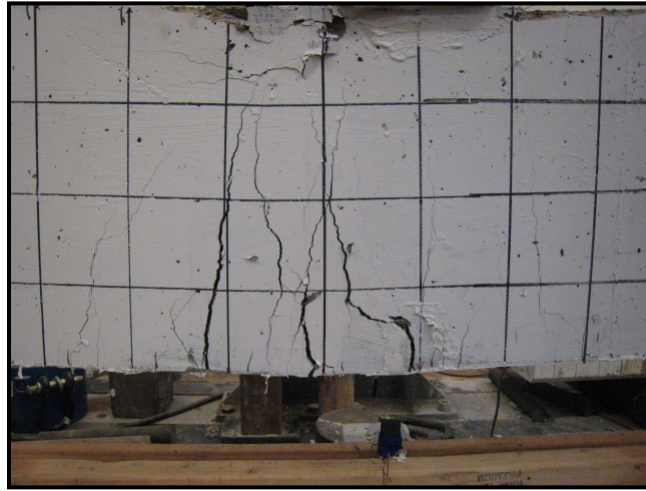
Table 5.3. Experimental Results of Prestressed SCC Members

I.D.	V_f (%)	First cracking displacement, mm (in.)	Displacement at ultimate force, mm (in.)	μ^\dagger	Force			$P_{u,meas} /$ $P_{u,calc}$
					First Cracking Force $P_{cr,meas}$, kN (kips)	Ultimate force $P_{u,meas}$, kN (kips)	Ultimate force $P_{u,calc}$, kN (kips)	
<i>R1</i>	0	9 (0.37)	105 (4.12)	3.7	56.7 (12.76)	113 (25.36)	106 (23.88)	1.06
<i>R2</i>	0.5	12 (0.48)	137 (5.41)	4.7	64.5 (14.53)	121 (27.33)	109 (24.62)	1.11
<i>I1</i>	0	17 (0.66)	39 (1.52)	3.6	93 (20.95)	103 (23.21)	143 (32.29)	0.72
<i>I2</i>	0.5	14 (0.55)	51 (2.01)	2.4	88.9 (20.02)	137 (30.84)	149 (33.46)	0.92
<i>G1</i>	0	9 (0.34)	37 (1.46)	3.9	854 (192.4)	1326 (298.7)	1309 (294.8)	1.01

\dagger : $\mu = (\Delta_u / \Delta_y)$; Δ_u = displacement at failure; Δ_y = yield displacement;

V_f = Steel fiber volume fraction;

Conversion: 1 mm = 0.039 in.; 1 kN = 0.2248 kips.



(a) R2 Specimen

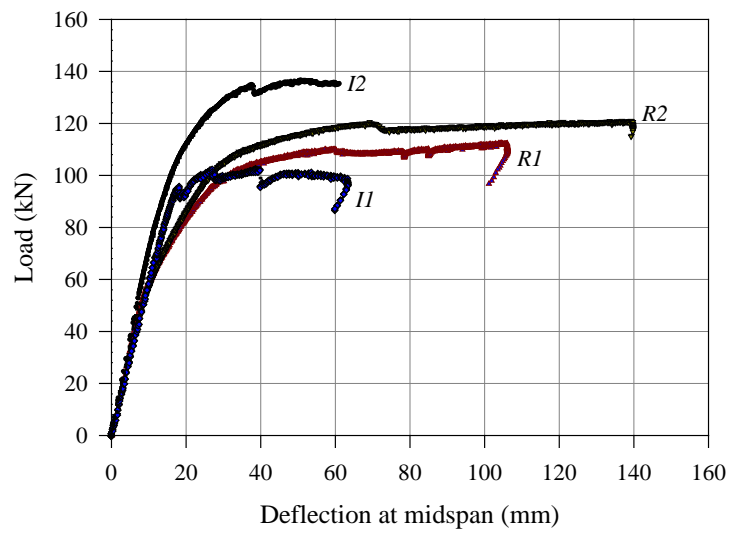


(b) I1 Specimen

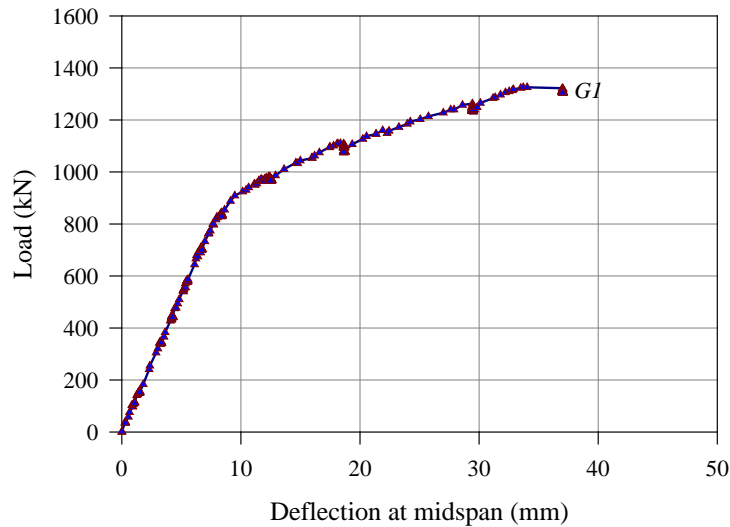


(c) G1 Specimen

Figure 5.12. Beam Failures and Cracking Patterns at Mid-Span



(a) R1, R2, I1, and I2 Specimens



(b) *G1* Specimen

Figure 5.13. Load-Deflection at Mid-Span Relationship
(Conversion: 1 kN = 0.2248 kips; 1 mm = 0.039 in.)

5.3 COMPARISON WITH NUMERICAL ANALYSIS RESULTS

The analysis was conducted as a team effort (Kim et al. [45]) using ANSYS (three-dimensional nonlinear modeling) and OpenSees (two-dimensional nonlinear modeling), which are nonlinear finite element analysis programs. The scope of work includes comparisons between the experimental data and the analysis performed using the aforementioned finite element programs to draw the best conclusions.

To numerically simulate the experiments described previously, a total of ten FE analyses for five beams were carried out under 2D and 3D modeling schemes. The material parameters used in the modeling are summarized in Table 5.4. The following section presents comparisons between experimental and numerical simulation results. More details for the numerical simulations are available in the paper by Kim et al. [45].

Table 5.4. Material Parameters Used 2D Modeling

Concrete (<i>Concrete02</i>)		Lightweight w/o SF	Lightweight w/ SF	Normalweight
		$\gamma_c = 1,840 \text{ kg/m}^3$ (Members <i>R1</i> & <i>I1</i>)	$\gamma_c = 1,840 \text{ kg/m}^3$ (Members <i>R2</i> & <i>I2</i>)	$\gamma_c = 2,400 \text{ kg/m}^3$ (Members <i>G1</i>)
Confined	$f'_{cc} = 1.3f'_c$	53.4 MPa (7.75 ksi)	70.3 MPa (10.2 ksi)	-
Concrete	$\varepsilon_{cc0} = 2f'_{cc}/E_c$	0.0064 mm/mm	0.0079 mm/mm	-
	$f_{ccu} = 0.2f'_{cc}$	10.7 MPa (1.55 ksi)	14.1 MPa (2 ksi)	-
	$\varepsilon_{ccu} = 5\varepsilon_{cc0}$	0.0322 mm/mm	0.0396 mm/mm	-
	E_c	16579 MPa (2404 ksi)	17772 MPa (2577 ksi)	-
	$f_r = 7.5\sqrt{f'_{cc}}$	4.6 MPa (0.66 ksi)	5.2 MPa (0.76 ksi)	-
Unconfined	f'_c	41.1 MPa (5.96 ksi)	54.1 MPa (7.85 ksi)	41.4 MPa (6 ksi)
Concrete	ε_{c0}	0.0034 mm/mm	0.0042 mm/mm	0.003 mm/mm
	$f_{cu} = 0.2f'_c$	8.2 MPa (1.19 ksi)	10.8 MPa (1.57 ksi)	8.3 MPa (1.2 ksi)
	$\varepsilon_{cu} = 5\varepsilon_{c0}$	0.01 mm/mm	0.01 mm/mm	0.01 mm/mm
	E_c	16579 MPa (2404 ksi)	17772 MPa (2577 ksi)	30448 MPa (4415 ksi)
	$f_r = 7.5\sqrt{f'_{cc}}$	4 MPa (0.58 ksi)	4.6 MPa (0.66 ksi)	5.8 MPa (0.84 ksi)
Non-prestressed reinforcement (<i>Steel02</i>)				
Grade 60	f_y	414 MPa (60 ksi)		
Steel	E_s	200,000 MPa (29,000 ksi)		
	α	0.005		
Prestressed reinforcement (<i>Steel02</i>)				
Seven-wire	f_{pu}	1862 MPa (270 ksi)		
low-	$f_{py} = 0.96f_{pu}$	1788 MPa (259.2 ksi)		
Relaxation	E_{ps}	196,552 MPa (28,500 ksi)		
Strand	α	0.005		

5.3.1 Comparison between Numerical and Experimental Results

Applied loads at cracking and concrete crushing (ultimate) stages and their associated deflections are summarized in Table 5.5. Both 2D and 3D numerical analysis results for histories of the applied loads vs. vertical mid-span deflections are shown in Figure 5.15, in comparison with experimental data. The experimental data are the average extracted from two WPs instrumented on both the front and back sides of the member at the mid-span (see Figure 5.2).

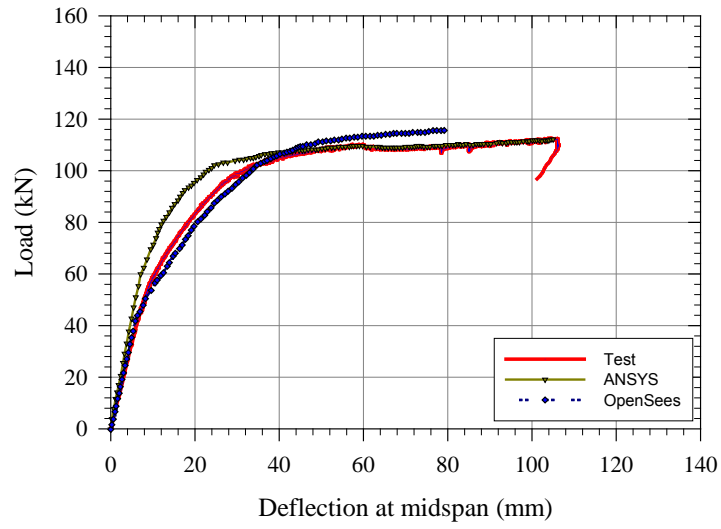
Overall, the predicted nonlinear behavior and ultimate loads (denoted as P_n) correlated well with their experimental counterparts, except for *I2* where little concrete cover appeared to be provided. Only the 2D modeling for *R1* and *R2* did not capture the histories from initial cracking to yielding of the steel. This was due to the fact that the *Concrete02* material implemented in the OpenSees source code (Mazzoni et al. [47]) assumed an initial constitutive stiffness of normalweight concrete, not lightweight concrete. However, the actual stiffness of the lightweight concrete was softer almost by half (see Table 5.4 for values). The discrepancy was much higher in the rectangular members, likely due to the inaccurate modeling of the confined lightweight concrete. Despite some discrepancies in the results, the numerical results were generally in good correspondence with the experimental data.

Based on the comparison analysis, it is generally concluded that the properties of self-consolidating-concrete (SCC) in prestressed concrete members are not so different from those of conventional concrete. Therefore, the use of SCC is a viable option for prestressed flexural members, and extensive further research in this area is evident.

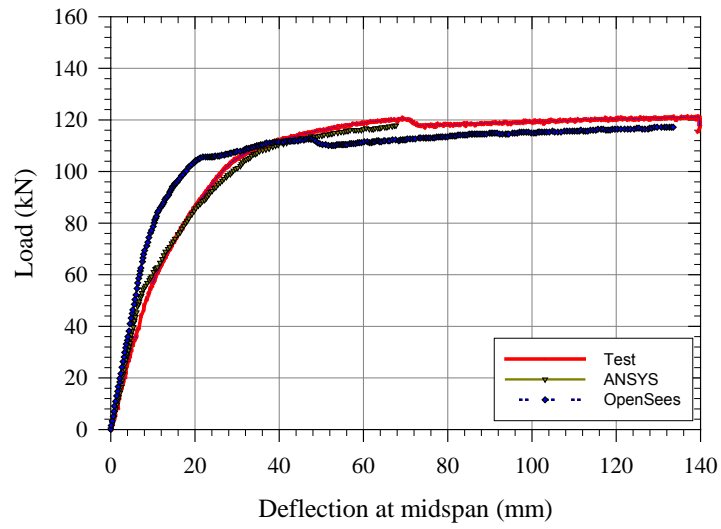
Table 5.5. Summary of Experimental and Numerical Simulation Results

I.D.		δ_i , mm (in.)	P_{cr} , kN (kips)	δ_{cr} , mm (in.)	P_n , kN (kips)	δ_n , mm (in.)
R1	Test	NA	56.7 (12.76)	9.4 (0.37)	112.6 (25.36)	104.6 (4.12)
	2D model	-2.8 (-0.11)	41.1 (9.26)	4.8 (0.19)	112.1 (25.24)	105.2 (4.14)
	3D model	-3.3 (-0.13)	44 (9.91)	6.35 (0.25)	115.4 (26)	79.8 (3.14)
R2	Test	NA	64.5 (14.53)	12.2 (0.48)	121.3 (27.33)	137.4 (5.41)
	2D model	-3 (-0.12)	47.2 (10.62)	5.1 (0.2)	116.1 (26.15)	133.4 (5.25)
	3D model	-3.6 (-0.14)	51.6 (11.62)	6.9 (0.27)	117.7 (26.5)	68.8 (2.71)
I1	Test	NA	93.2 (20.95)	16.8 (0.66)	103.2 (23.21)	38.6 (1.52)
	2D model	-8.9 (-0.35)	71.6 (16.13)	11.4 (0.45)	140.1 (31.56)	46.2 (1.82)
	3D model	-7.6 (-0.3)	75.5 (17)	14.5 (0.57)	110.3 (24.84)	32.3 (1.27)
I2	Test	NA	88.9 (20.02)	14 (0.55)	137 (30.84)	51.1 (2.01)
	2D model	-9.7 (-0.38)	82.7 (18.63)	12.4 (0.49)	145.3 (32.72)	50.8 (2)
	3D model	-7.9 (-0.31)	88.8 (20)	15.5 (0.61)	138.8 (31.25)	42.9 (1.69)
G1	Test	NA	854 (192.44)	8.6 (0.34)	1326 (298.68)	37.1 (1.46)
	2D model	-3.6 (-0.14)	813 (183.16)	7.1 (0.28)	1317 (296.06)	31 (1.22)
	3D model	-2.8 (-0.11)	746 (168.13)	7.1 (0.28)	1316 (296.45)	35.1 (1.38)

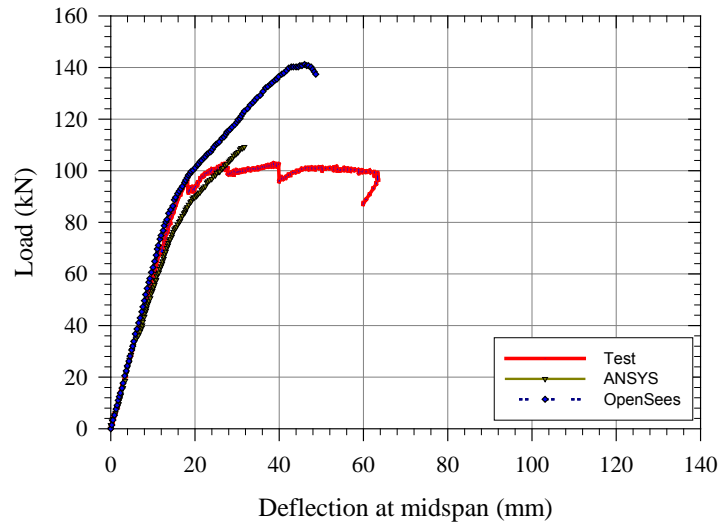
δ_i = Initial camber; P_{cr} = Force at cracking; δ_{cr} = Displacement at cracking; P_u = Force at ultimate; δ_u = Displacement at ultimate.



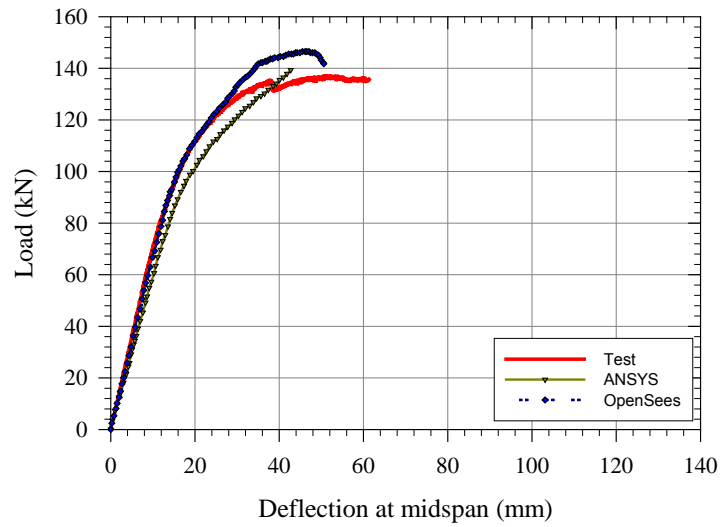
(a) R1 Specimen



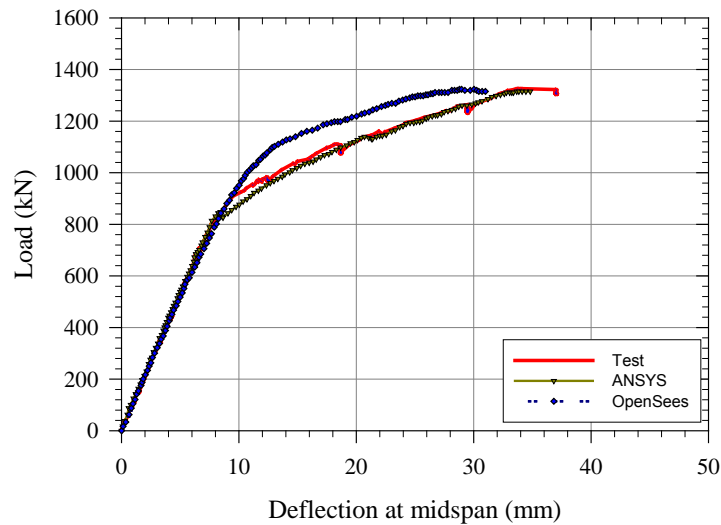
(b) R2 Specimen



(c) I1 Specimen



(d) I2 Specimen



(e) G1 Specimen

Figure 5.14. Load-Deflection at Mid-Span Relationship between Experimental and Numerical Results (Conversion: 1 kN = 0.2248 kips; 1 mm = 0.039 in.)

5.4 SUMMARY

A total of five prestressed concrete specimens consisting of four reduced-scale SCC beams and one full-scale Type-II AASHTO SCC bridge girder were experimentally examined. Subsequently, as a validation of the experimental simulation, nonlinear 2D and 3D FE analyses were carried out as a team effort (Kim et al. [45]).

The numerical simulations demonstrated their capability in simulating actual nonlinear behavior of prestressed concrete members. Overall, the predicted nonlinear behavior and ultimate loads (denoted as P_n) correlated well with their experimental counterparts. The results indicate that the properties of SCC in prestressed concrete members were not so different from those of conventional concrete.

This Page Is Intentionally Blank

6. LARGE SCALE TESTING AND ANALYSIS OF REINFORCED CONCRETE CONNECTIONS WITH HEADED BARS UNDER SEISMIC LOADS

6.1 INTRODUCTION

Given the strict restriction of headed bar clear spacing set forth by ACI 318-08, the current study investigates the applicability of closely-spaced headed bars in exterior beam-column connections that are part of earthquake-resistant structures. The following sections discuss details of test procedures and results from large-scale exterior beam-column connections with closely-spaced headed bars, subjected to earthquake-type loading. In particular, the seismic performance of the tested specimens was quantitatively assessed by adhering to the testing protocol of ACI 374.1-05: Acceptance Criteria for Moment Frames Based on Structural Testing and Commentary (ACI [48]).

6.2 EXPERIMENTAL PROGRAM

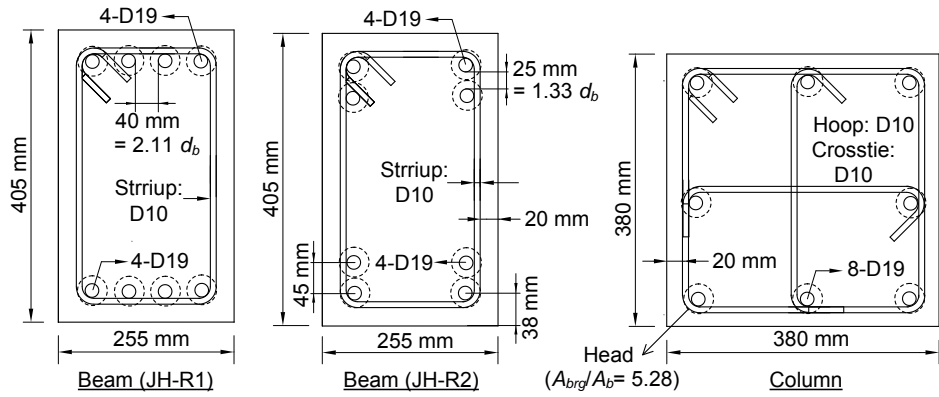
In this study, two beam-column subassemblies were tested: one with a single horizontal layer of closely-spaced headed bars and the other with two horizontal layers of headed bars with two vertically arranged heads touching each other. Each subassembly represented an exterior connection subjected to lateral earthquake loading, isolated at inflection points between floors and between column lines. Considering a prototype structure with a story height of 2.9 m (9.5 ft) and a span length of 4.5 m (14.8 ft), the specimens represent approximately 2/3-scale models.

6.2.1 Design of Test Specimens

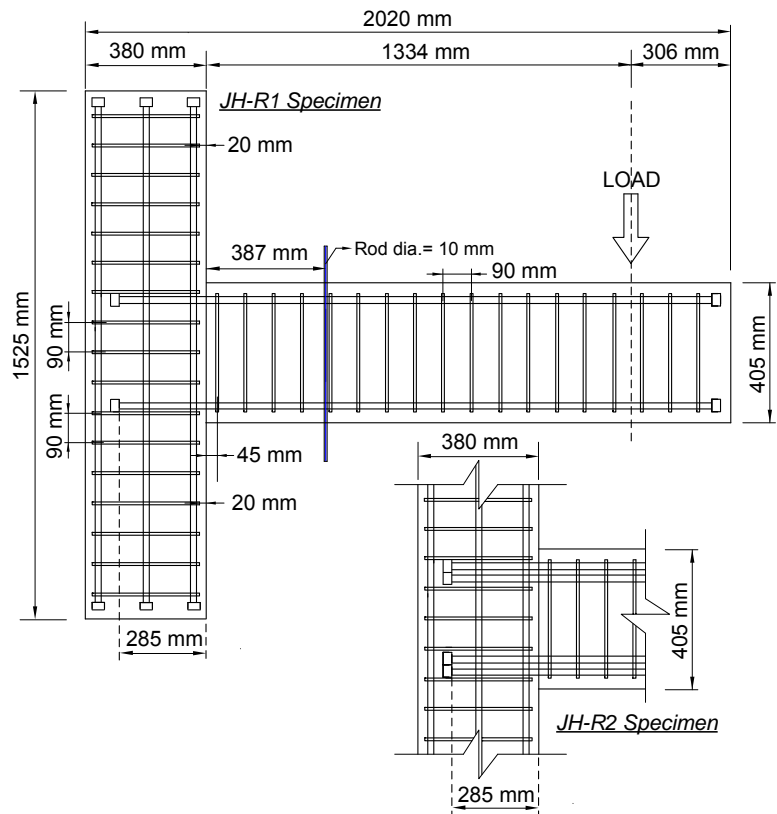
The specimens were designed and detailed in adherence to ACI seismic design requirements (ACI 318-08) and recommendations (ACI 352-02) applying to special moment frame members, except for a few design parameters that were the focus of this investigation. Those parameters are (1) the clear spacing between headed bars and (2)

the number of horizontal layers of headed bars. Section 12.6 of ACI 318-08 requires the minimum clear spacing of $4d_b$ between headed bars, so that it may be judged to implicitly prohibit the use of multiple layers of headed bars in beams.

Figure 6.1 illustrates member sections, elevation views, and reinforcing details for the two specimens JH-R1 (Joint with Headed-Reinforcement of 1 top or bottom layer) and JH-R2 (Joint with Headed-Reinforcement of 2 top or bottom layers). Each specimen consisted of a column and a beam framing into the column on one side. All beams and columns were reinforced with a single type of headed deformed bars, and one end of each beam bar was anchored in the connection. Figure 6.2 illustrates details and dimensions of the headed bars, also summarized in Table 6.1. The ratio of net bearing area of head (A_{brg}) to bar area (A_b) was 5.28 for all beam and column bars, which satisfies the minimum ratio of 4 required in ACI 318-08. Both specimens JH-R1 and JH-R2 had identical design details except for the reinforcing bar layout of the beam. JH-R1 had a single layer for both the top and bottom beam bars, while JH-R2 had two layers for each of them (see Figures 6.1(a) and 6.1(b)). Consequently, the spacing between the headed bars was also different in the two specimens; the clear bar spacing was $2.1d_b$ (horizontal) and $1.3d_b$ (vertical) in JH-R1 and JH-R2 respectively, which was much smaller than the minimum limit of $4d_b$ specified in ACI 318-08. The number and size of beam bars were the same in both specimens, achieving similar beam moment strengths and leading to similar overall lateral strengths of the connections with the development of beam hinging.



(a) Beam and Column Sections



(b) Reinforcement for Connection Subassemblies

Figure 6.1. Dimensions and Details for JH-R1 & JH-R2 (Conversion: 1 mm = 0.039 in.)



Figure 6.2. Heads and Threaded Connections (Conversion: 1 mm = 0.039 in.)

Table 6.1. Dimensions for Heads and Headed Bars

Type	d_b (mm; in.)	d_h (mm; in.)	t_h (mm; in.)	A_b (mm ² ; in ²)	$A_{nh} = A_{brg}$ (mm ² ; in ²)	A_{brg}/A_b
D19	19; 0.75	48; 1.89	29; 1.14	284; 0.44	1500; 2.32	5.28

d_b = bar diameter; A_b = bar area; d_h = head diameter; t_h = head thickness;

A_{nh} = net head area; A_{brg} = net bearing area of head.

In this study, $A_{brg} = A_{nh}$, as there is no obstruction (per ACI 318-08, §3.5.9).

The beam was 255 mm (10 in.) wide and 405 mm (16 in.) deep, reinforced with 4-D19 (4-No. 6) at both the top and bottom of the beam. The column was 380 mm (15 in.) by 380 mm (15 in.), reinforced with 8-D19 (8-No. 6) confined by a hoop (D10; No. 3) and two crossties (D10; No. 3) at a spacing of 90 mm (3.5 in.). A minimum concrete clear cover of 20 mm (0.75 in.) was provided in all members.

Table 6.2 summarizes the main design variables and other important parameters that are generally considered to govern the behavior of RC beam-column connections subjected to lateral cyclic loading. The specimens satisfied the ACI 318 seismic design provisions related to relative column versus beam flexural strength, confinement of the joint core, joint shear strength, and anchorage of reinforcement in the connection region. Thus, the specimens were intended to establish a beam hinging mechanism if the tested parameters (i.e., headed bar spacing and number of beam bar layer) would not induce an unfavorable premature failure. The column-to-beam moment strength ratios (M_r) in Table 6.2, computed using both specified and measured material properties, were all much larger than the minimum limit of 1.2. The following equations present the maximum joint shear demands determined using two different methods and the joint shear capacity defined by ACI 318-08 or ACI 352R-02 (Joint ACI-ASCE [23]).

$$V_{j,u_1} = \frac{M_{peak}}{0.9d} - V_{c,peak} \quad (6.1)$$

$$V_{j,u_2} = A_s f_{y_meas} - V_{c,peak} \quad (6.2)$$

$$V_{j,n} = 0.083\gamma\sqrt{f'_c}b_jh_c \text{ (MPa)} \quad (6.3)$$

$$V_{j,n} = \gamma\sqrt{f'_c}b_jh_c \text{ (psi)}$$

The maximum joint shear demands ($V_{j,u}$) were normalized by ($0.083\gamma\sqrt{f'_c}b_jh_c$ [MPa]; $\sqrt{f'_c}b_jh_c$ [psi]) as indicated in Table 6.2, so that the normalized joint shear demand is comparable to γ in Equation (6.3). Here, the effective joint width (b_j) was calculated following both ACI 318-08 and ACI 352R-02 (see superscripts “†” and “††” in Table 6.2). The superscripts “#” and “##” indicate the values normalized using V_{j,u_1} and V_{j,u_2} , respectively.

Table 6.2. Connection Design Parameters

Specimen		JH-R1	JH-R2
Moment strength ratio [±] , M_r	Based on f'_c and f_y	2.13	2.28
	Based on $f'_{c,meas}$ and $f_{y,meas}$	2.14	2.3
Joint shear demand, normalized by $(0.083\sqrt{f'_c}b_jh_c)$	ACI 318-08 [†]	8.1 [#] (6.7 ^{##})	7.9 [#] (6.8 ^{##})
	ACI 352R-02 ^{††}	9.8 [#] (8 ^{##})	9.5 [#] (8.2 ^{##})
Joint reinforcement [§] (A_{sh}),		213 mm ² at 90 mm	213 mm ² at 90 mm
Comparison of joint transverse reinforcement ratio	ρ_h/ρ_h^{ACI318}	1.07	1.07
	ρ_h/ρ_h^{ACI352}	1.07	1.07
Smallest spacing between beam bars		40 mm* or 2.11 d_b^*	25 mm** or 1.33 d_b^{**}
Number of layers of beam top or bottom bars		1	2

$$^{\pm}M_r = \sum M_n(\text{columns})/M_n(\text{beam});$$

[†] In ACI 318-08, $b_j = b_b + 2x$, x = smaller distance between beam and column edges (= b_c);

^{††} In ACI 352R-02, $b_j = b_b + \sum mh_c/2$, $m = 0.3$ when $e > 2b_c/8$, otherwise $m = 0.5$ (= $[b_b + b_c]/2$);

$$^{\#}V_j = \left(\frac{M_{peak}}{0.9d} - V_{c,peak}\right)/(0.083\sqrt{f'_c}b_jh_c); \quad ^{\#\#}V_j = (A_s f_{y,meas} - V_{c,peak})/(0.083\sqrt{f'_c}b_jh_c);$$

[§] A_{sh} = total area of horizontal joint reinforcement within layer in longitudinal direction;

* Horizontal spacing; ** Vertical spacing; $\rho_h = A_{sh}/(s_h h'')$ where s_h is the hoop spacing and h'' is the joint core width; ρ_h^{ACI318} and ρ_h^{ACI352} were computed in accordance with ACI 318-08 (Chapter 21) and ACI 352R-02 (Type 2 connection) minimum requirements, respectively.

Conversion: 1 mm = 0.039 in.

The normalized joint shear demands were quite smaller than the maximum of 12 specified by both ACI 318-08 and ACI 352R-02 based on the joint confinement level from adjoining members. Both specimens were reinforced with three layers of horizontal joint reinforcement between top and bottom beam bars; each layer consisted of a D10 (No. 3) hoop and two D10 (No. 3) crossties. This is approximately the minimum amount of joint reinforcement prescribed in ACI 318-08 and ACI 352R-02, as shown in Table 6.2.

An identical development length was provided for all beam bars terminating in the connections (see Figure 6.1). The provided development length was determined in comparison with the code-specified development length. The minimum development length for headed bars required in ACI 318-08, Section 12.6.2 ($l_{dt,318}$) and ACI 352R-02, Section 4.5.3 ($l_{dt,352}$) shall be determined as follows:

$$l_{dt,318} = \frac{f_y d_b (\text{MPa})}{5.2 \sqrt{f'_c (\text{MPa})}} \quad (6.4)$$

$$l_{dt,318} = \frac{f_y d_b (\text{psi})}{62 \sqrt{f'_c (\text{psi})}}$$

$$l_{dt,352} = \frac{f_y d_b (\text{MPa})}{5.6 \sqrt{f'_c (\text{MPa})}} \text{ for Type 1 connections} \quad (6.5)$$

$$l_{dt,352} = \frac{f_y d_b (\text{psi})}{62 \sqrt{f'_c (\text{psi})}} \text{ for Type 1 connections}$$

$$l_{dt,352} = \frac{f_y d_b (\text{MPa})}{6.6 \sqrt{f'_c (\text{MPa})}} \text{ for Type 2 connections} \quad (6.6)$$

$$l_{dt,352} = \frac{f_y d_b (\text{psi})}{79 \sqrt{f'_c (\text{psi})}} \text{ for Type 2 connections}$$

Here, a Type 1 connection is defined in ACI 352-02 as a connection designed on the basis of strength for members expected not to undergo significant inelastic deformation, whereas a Type 2 connection is defined as a connection intended to dissipate energy through reversals of deformations into the inelastic range. In Equation (6.6), a stress multiplier equal to 1.25 is incorporated to account for possible over-strength and strain hardening of the reinforcement. It should be noted that the locations of the critical section and development endpoint are defined separately for these three equations; for example, the critical section for Type 2 connections is different from that for Type 1 connections (refer to Figure 4.8 of ACI 352R-02). Table 6.3 summarizes required and provided development lengths for the beam headed bars per ACI 318-08 and ACI 352R-02. The intent of the design was to provide a development length similar to (per

ACI 318-08) or moderately larger than (per ACI 352R-02) the required value calculated with specified material properties.

Table 6.3. Provided and Required Development Lengths for Headed Beam Bars Used for Connection Subassemblies

	I.D.	Provided development length (mm)	Required development length [†] (mm)	Required development length ^{††} (mm)
ACI 318-08	JH-R1	285 or $15d_b$	285 or $15d_b$	335 or $17.67d_b$
	JH-R2	285 or $15d_b$	285 or $15d_b$	335 or $17.67d_b$
ACI 352R-02 Type 1 connection	JH-R1	315 or $16.53d_b$	270 or $14.13d_b$	318 or $16.67d_b$
	JH-R2	315 or $16.53d_b$	270 or $14.13d_b$	318 or $16.67d_b$
ACI 352R-02 Type 2 connection	JH-R1	295 or $15.5d_b$	240 or $12.67d_b$	283 or $14.8d_b$
	JH-R2	295 or $15.5d_b$	240 or $12.67d_b$	283 or $14.8d_b$

[†] Calculated based on specified values of f'_c and f_y ;

^{††} Calculated based on measured values of $f'_{c,meas}$ and $f_{y,meas}$.

Conversion: 1 mm = 0.039 in.

However, the required development length increased by about 10% due to higher yield strength of the reinforcement, so that the provided length was about 10% smaller than the required length calculated using measured material properties per ACI 318-08.

6.2.2 Construction and Material Properties

Figure 6.3 shows the progress of beam-column connection fabrication. For each test subassembly, all members were cast at one time, and the two specimens were constructed with the same batch of concrete on the same day. Concrete with a maximum aggregate size of 9.5 mm (0.35 in.) and a slump of 127 mm (5 in.) was used to accommodate any steel congestion in the connection region and the small clear cover of 20 mm (0.75 in.). The unit weight of normal-weight concrete was 2400 kg/m³ (150 lb/ft³) and the water-to-cement ratio was 0.51. The design compressive strength of concrete was 27.6 MPa (4 ksi), and the specified yield strength of reinforcing steel was 414 MPa (60 ksi). The ASTM C39 test method (ASTM) was applied to determine the unconfined compressive strength of cylinders. The test was conducted by applying a compressive axial load to molded cylinders. The compressive strength of the specimen was calculated by dividing the maximum load by the cross-sectional area of the specimen. The average value of concrete compressive strength was 30.1 MPa (4,371 psi) (Figure 6.4). The ASTM test C78 method was applied to determine the modulus of rupture (f_r) of concrete. Here, five 152 mm × 152 mm × 508 mm (6 × 6 × 20 in.) concrete prisms were tested in accordance with ASTM C78. The average value of f_r is 5.1 MPa (740 psi) (see Figure 6.5). Table 6.4 summarizes the fresh and hardened concrete properties including the compressive strength of concrete measured on the day of subassembly testing. Also, Table 6.5 lists the measured yield strength ($f_{y,meas}$), yield strain ($\varepsilon_{y,meas}$), ultimate strength ($f_{u,meas}$), and modulus of elasticity ($E_{s,meas}$) for the column and beam longitudinal reinforcement used (Figure 6.6).



Figure 6.3. Progress of Fabricating Specimens

Table 6.4. Fresh and Hardened Concrete Properties

Slump	Compressive strength [†] ($f'_{c,meas}$)	Modulus of rupture ^{††} (f_r)
127mm (5 in.)	30.1 MPa (4.4 ksi)	5.1 MPa (740 psi)

[†] Seven concrete cylinders were tested in accordance with ASTM C39;

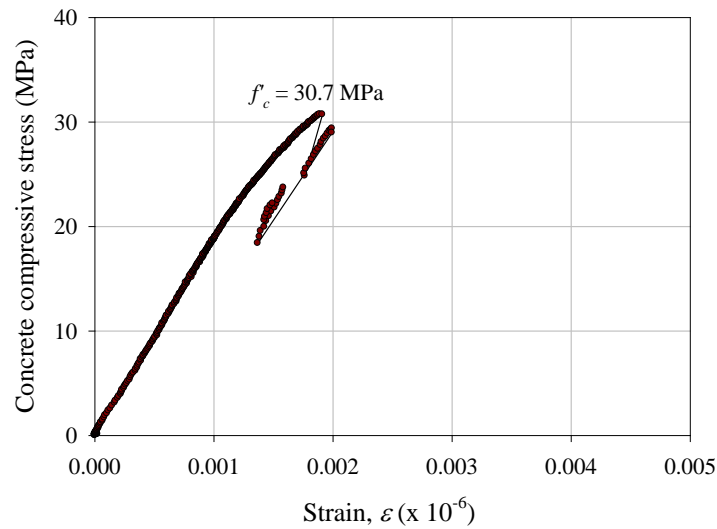
^{††} Five concrete prisms were tested in accordance with ASTM C78.

Table 6.5. Measured steel Material Properties

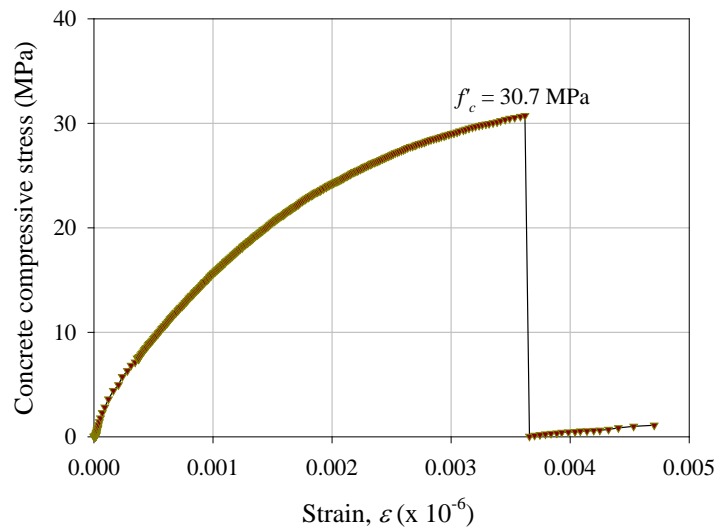
	d_b , mm (in.)	$E_{s,meas}$, GPa (ksi)	$f_{y,meas}$, MPa (ksi)	$\varepsilon_{y,meas}$	$f_{u,meas}$, MPa (ksi)
D19-JH	19 (0.75)	183.4 (26593)	479 (69.5)	0.0026	721 (104.5)

Two steel coupons were tested, and averaged per bar size.

$E_{s,meas}$ = measured modulus of elasticity of reinforcing steel; $f_{y,meas}$ = measured steel yield strength; $\varepsilon_{y,meas}$ = measured steel strain at $f_{y,meas}$; $f_{u,meas}$ = measured steel ultimate tensile strength.

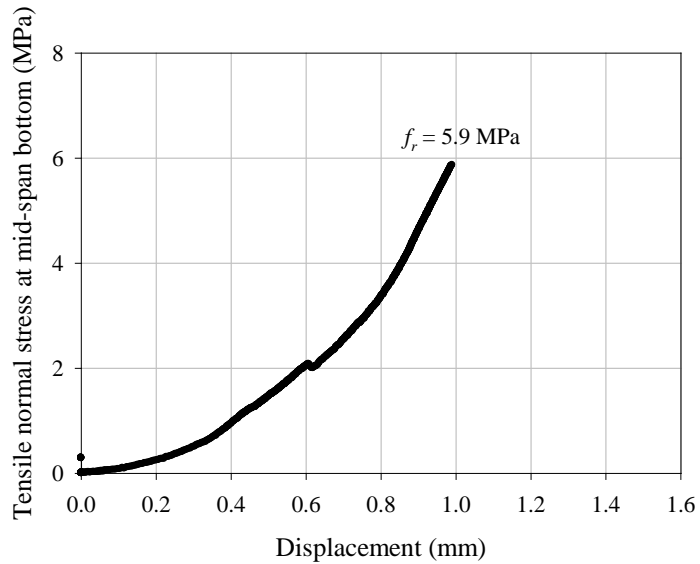


(a) Cylinder 1

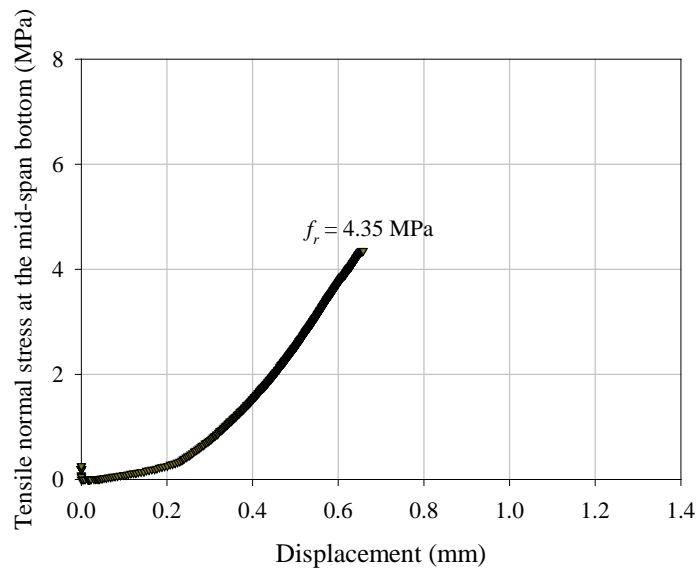


(b) Cylinder 2

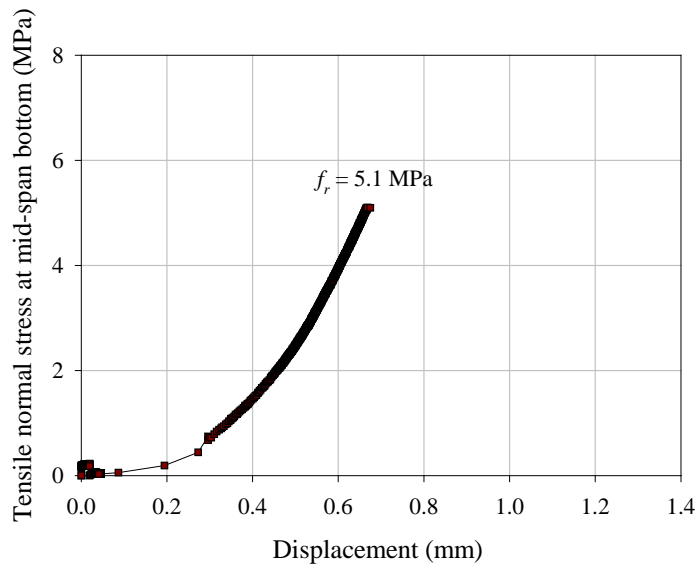
Figure 6.4. Stress vs. Strain Curve for Concrete Compressive Strength Tests
(Conversion: 1MPa = 145 psi)



(a) Prism 1



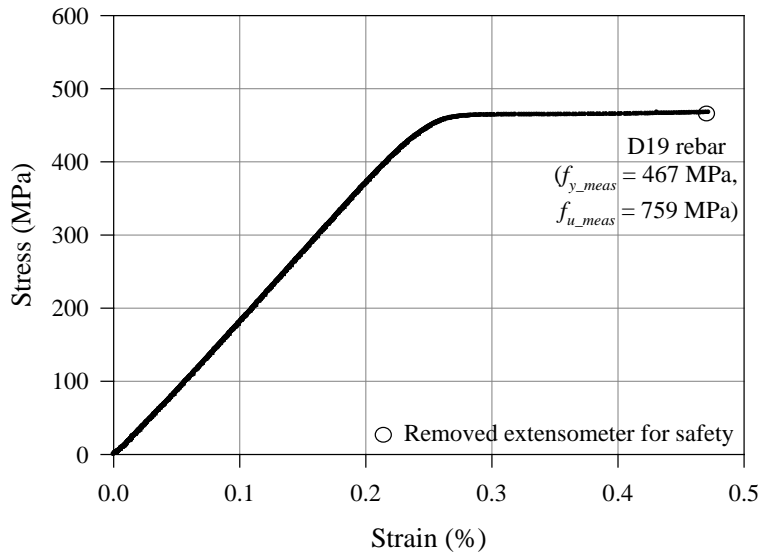
(b) Prism 2



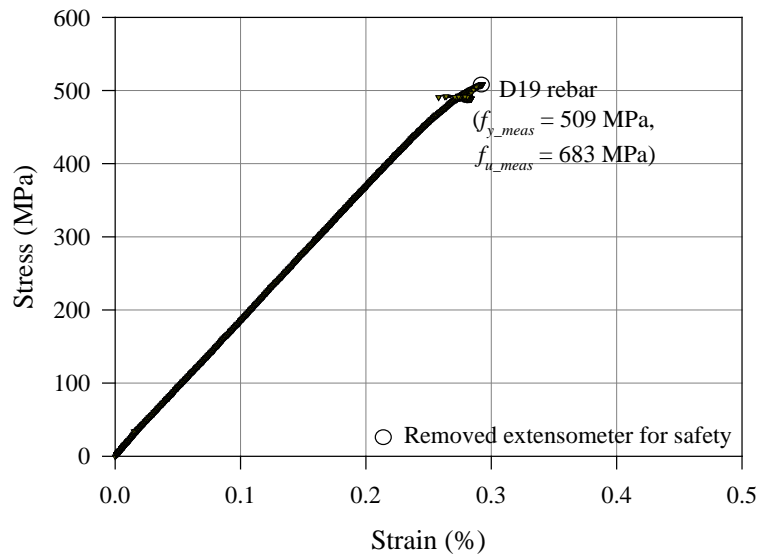
(c) Prism 3

Figure 6.5. Tensile Normal Stress at Mid-Span Bottom versus Displacement Relationship for MOR Tests

(Conversion: 1MPa = 145 psi; 1 mm = 0.039 in.)



Longitudinal Deformed Bar 1



(b) Longitudinal Deformed Bar 2

Figure 6.6. Stress-Strain Relationship for D19 (No. 6) Longitudinal Deformed Bars
 (Conversion: 1MPa = 145 psi)

6.2.3 Test Setup and Loading Sequence

Figures 6.7 and 6.8 illustrate the test setup with the specimen supports and other key components (e.g., LVDTs labeled). The specimens were tested in such a position that the column was placed horizontally. The column was linked to a universal hinge connector at each end (i.e., top and bottom), anchored to the strong floor. The end of the beam was linked to an actuator with a swivel connector. Thus, the end of the beam and the top and bottom of the column were all pin-connected in the loading plane, to simulate inflection points of a moment frame subjected to lateral earthquake loading. The column pin-to-pin story height (I_c) was 2057 mm (81 in.), while the beam length (I_b) between the loading point and the beam-joint interface was 1334 mm (52.5 in.).

Uni-axial reversed cyclic loading was statically applied at the end of the beam, parallel to the longitudinal direction of the column, by a hydraulic actuator with a +/- 245 kN (55 kips) loading capacity and a +/- 75 mm (3 in.) linear range. Positive and negative loading directions are indicated in Figure 6.8. No column axial load was applied conservatively in accordance with results of previous studies that found the presence of column compression could either slightly improve joint shear strength or have no apparent influence on it (Meinheit and Jirsa [49]).

Instrumentation used in each specimen is summarized in Table 6.6. Two LVDTs were used on each face of the connection to examine overall joint shear deformations. Four LVDTs were installed on the top and bottom of the beam to monitor beam plastic rotations in the vicinity of the beam-joint interface. A load cell was used to measure lateral loads, and eleven LVDTs and WPs were used to measure beam and column displacements at selected locations as shown in Figures 6.7 and 6.8.

Figure 6.9 shows the pattern of cyclic lateral displacements applied by the actuator during each test. A total of twenty-four displacement cycles were statically applied up to

5% drift ratio. Three consecutive same-drift cycles were tested to examine strength and stiffness degradations under reversed cyclic loading, and more specifically to evaluate the test results based on the performance acceptance criteria specified in ACI 374.1-05. In the following section, detailed analysis of test results of the two specimens JH-R1 and JH-R2 is presented.

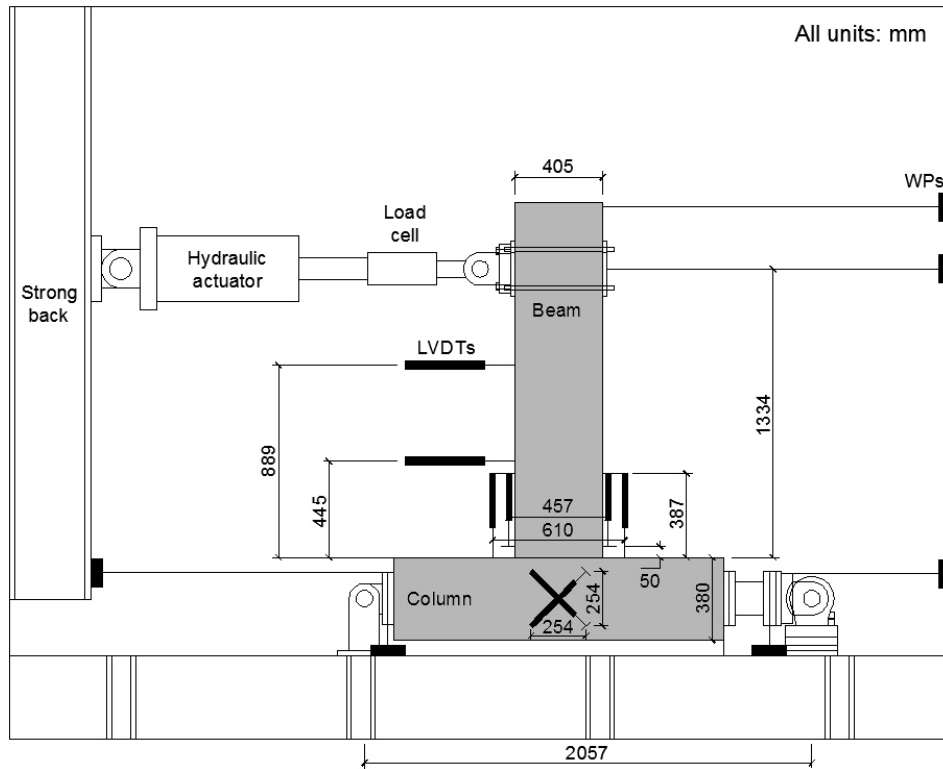


Figure 6.7. Test Setup and Dimensions for Instrumentation
(Conversion: 1 mm = 0.039 in.)

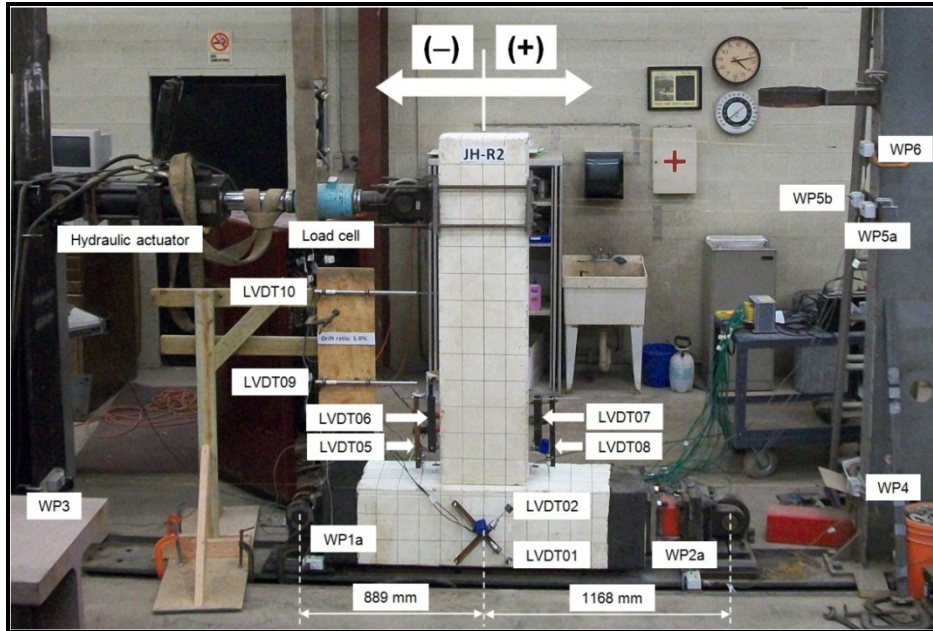


Figure 6.8. Overview of JH-R2 Test Specimen and Setup
(Conversion: 1 mm = 0.039 in.)

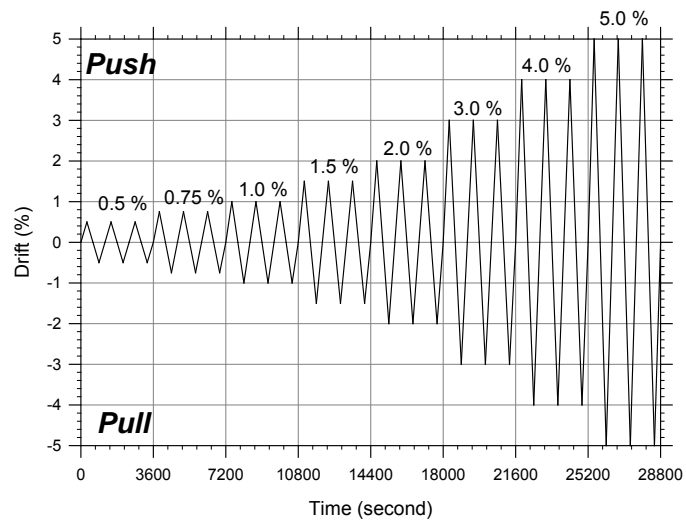


Figure 6.9. Loading History

Table 6.6. Instrumentation List

I.D.	Capacity	Type (or model)	Manufacturer
Hydraulic actuator	±244 kN (±55 kips) Stroke: 152 mm (6 in.)	Piston: 18.53 in ²	MTS Systems Corporation
Load cell	222 kN (50 kips)	T2P1	BLH Electronics
LVDT01*	±10.2 mm (±0.4 in.)	Sensotec sensor (S3C)	Honeywell
LVDT02	±10.2 mm (±0.4 in.)	Sensotec sensor (S3C)	Honeywell
LVDT03	±6.4 mm (± 0.25 in.)	Sensotec sensor (S2C-100)	Honeywell
LVDT04	±10.2 mm (±0.4 in.)	Sensotec sensor (S3C)	Honeywell
LVDT05	±10.2 mm (±0.4 in.)	Sensotec sensor (S3C)	Honeywell
LVDT06	±10.2 mm (±0.4 in.)	Sensotec sensor (S3C)	Honeywell
LVDT07	±10.2 mm (±0.4 in.)	Sensotec sensor (S3C)	Honeywell
LVDT08	±10.2 mm (±0.4 in.)	Sensotec sensor (S3C)	Honeywell
LVDT09	±102 mm (±4 in.)	Sensotec sensor (JEC-C)	Honeywell
LVDT10	±102 mm (±4 in.)	Sensotec sensor (JEC-C)	Honeywell
WP1a	±127 mm (± 5 in.)	PT101-0010-111-1110	Celesco
WP1b	±127 mm (± 5 in.)	PT101-0010-111-1110	Celesco
WP2a	±127 mm (± 5 in.)	PT101-0010-111-1110	Celesco
WP2b	±127 mm (± 5 in.)	PT101-0010-111-1110	Celesco
WP3*	±127 mm (± 5 in.)	PT101-0010-111-1110	Celesco
WP4	±127 mm (± 5 in.)	PT101-0010-111-1110	Celesco
WP5a	±127 mm (± 5 in.)	PT101-0010-111-1110	Celesco
WP5b	±127 mm (± 5 in.)	PT101-0010-111-1110	Celesco
WP6	±127 mm (± 5 in.)	PT101-0010-111-1110	Celesco
Strain gauge01 through	120.8 ±0.5 Ω	WFLA-6-11	Tokyo Sokki Kenkyujo Co., Ltd.
Strain gauge25	120.8 ±0.5 Ω	WFLA-6-11	Tokyo Sokki Kenkyujo Co., Ltd.

*LVDT01: Linear variable differential transducer01; * WP3: Wire potentiometer3

6.3 ANALYSIS OF TEST RESULTS

6.3.1 Load-Displacement Response

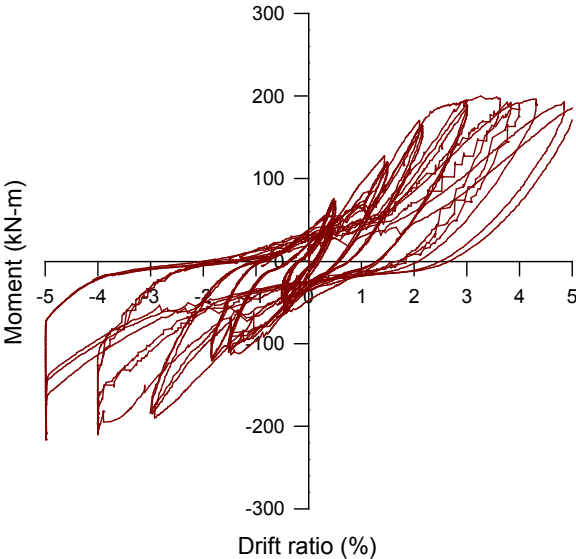
Figures 6.10 and 6.11 show the hysteretic response of beam moment (at the column face) vs. drift ratio (hereafter “load-displacement”) for Specimens JH-R1 and JH-R2, respectively. Also, Table 6.7 summarizes nominal beam moment strengths (M_n), peak beam moments reached (M_{peak}), and their corresponding drift ratios during testing. Here, the drift ratio (δ) was determined by dividing the beam end displacement by the beam length from the loading point to the column center. The hysteretic responses were

typical in that they exhibited pinching (the middle part of each hysteretic loop was relatively narrow), as well as stiffness and strength degradations during repeat same-drift cycles. These characteristics were attributed to concrete cracking, reinforcement bond slip around the connection region, and/or reinforcement yielding. Figure 6.12 compares the envelope load-displacement curves of the two specimens by connecting the peak drift point of each cycle. The specimens reached similar maximum loads in both loading directions (only slightly higher in JH-R1 due to the layout of beam bars), and also showed similar stiffness degradations under increasing drifts. On the other hand, JH-R2 showed less pinching than JH-R1, which was in accordance with the amount of dissipated energy per each cycle (see Table 6.8 for 4% drift ratio, which will be discussed later).

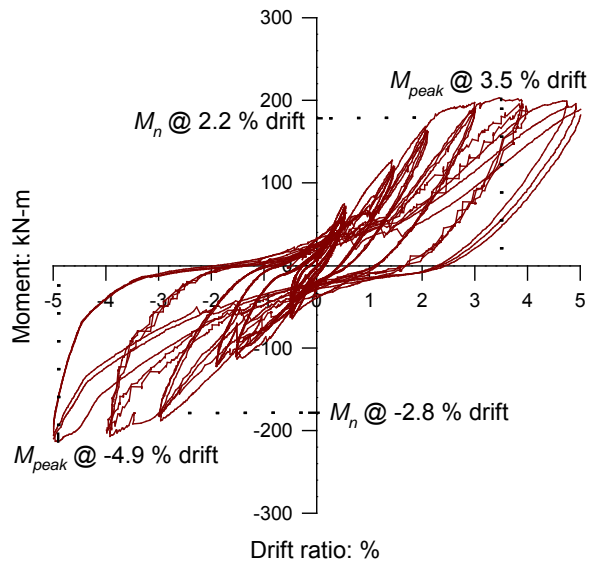
The connection failure mechanism was investigated first by observing the cracking pattern. With limited joint deterioration, extensive beam flexural cracks occurred at the beam-joint interface during 1.5% (for JH-R1) and 1% (for JH-R2) drift cycles. Flexural crack opening spread to half an effective-beam-depth away from the beam-joint interface by 3% drift ratio in both specimens. Also, the peak beam moment (M_{peak}) achieved during each test was about 15 to 20% larger than the nominal beam moment strength (M_n) calculated based on ACI 318-08, as indicated in Figures 6.10, 6.11 and 6.12 and also summarized in Table 6.7. Therefore, it was concluded that beam hinging fully developed adjacent to the beam-joint interface in both specimens. This conclusion is validated in the later section related to the beam plastic hinge development.

The specimens exhibited ductile load-displacement behavior (up to a displacement ductility of about 2.5, limited by the actuator stroke capacity) without showing notable strength drops by the end of the test (up to 5% drift ratio). Strength degradation of the specimens was examined by comparing story shear forces of consecutive same-drift cycles (reduction in story shear force during the second and third (repeat) cycles with respect to the first cycle). In both specimens, strength degradation remained low (roughly 5 ~ 8%) throughout testing. Considering that other mechanisms such as anchorage failure and excessive joint shear distress typically accompany large strength drops, it was concluded that the specimens did not undergo such failures. Therefore, it

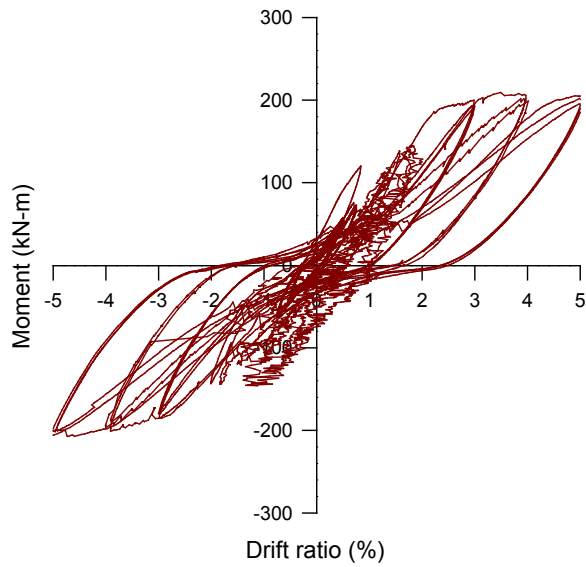
is noted that, even with a small headed bar spacing (in JH-R1) or with multiple layers of headed bars (in JH-R2), the specimens showed satisfactory performance under reversed cyclic lateral loading. This conclusion is validated in later sections.



(a) 0.44 m (17.5 in.) from Beam-Joint Interface



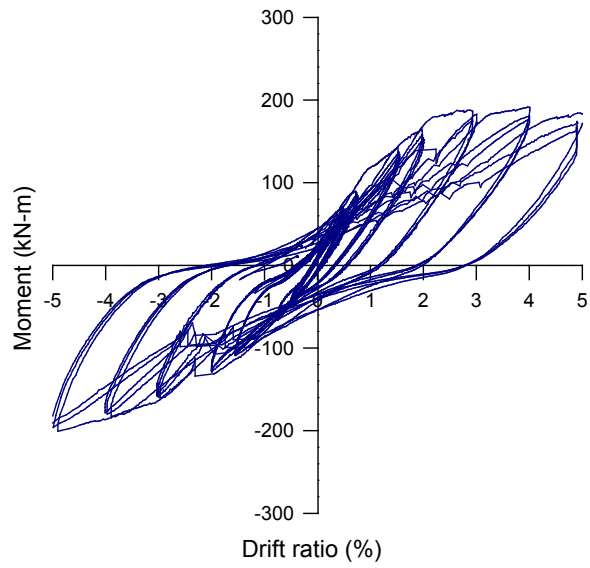
(b) 0.89 m (35 in.) from Beam-Joint Interface



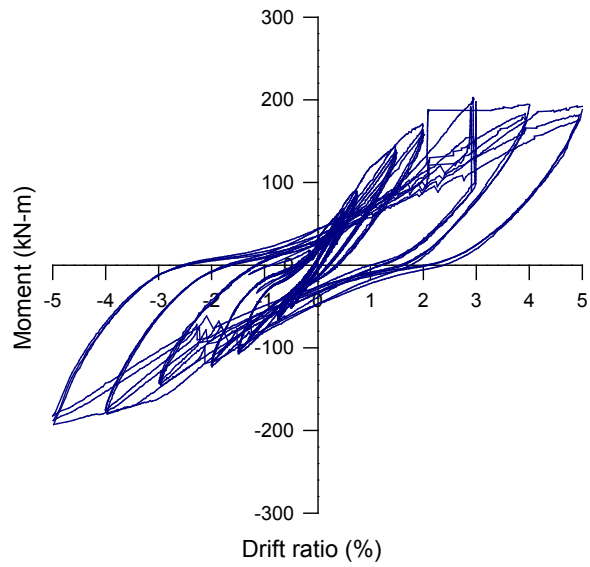
(c) 1.33 m (52.5 in.) from Beam-Joint Interface

Figure 6.10. Moment vs. Drift Ratio Relationships for JH-R1

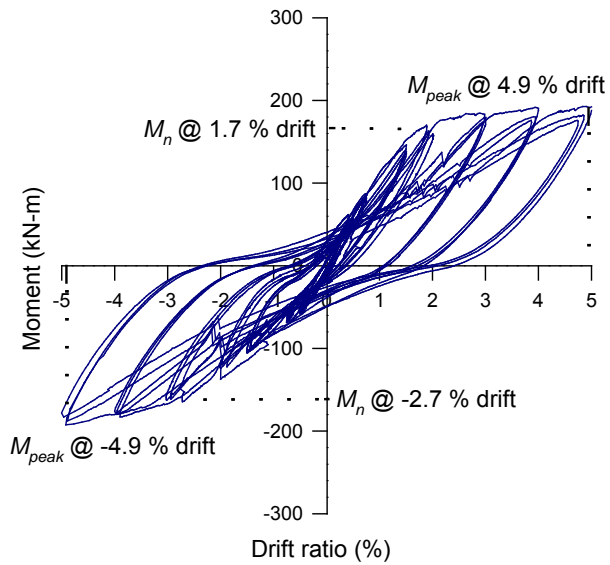
(Conversion: 1 kN-m = 8.85 kips-in.)



(a) 0.44 m (17.5 in.) from Beam-Joint Interface



(b) 0.89 m (35 in.) from Beam-Joint Interface



(c) 1.33 m (52.5 in.) from Beam-Joint Interface

Figure 6.11. Moment vs. Drift Ratio Relationships for JH-R2
(Conversion: 1 kN-m = 8.85 kips-in.)

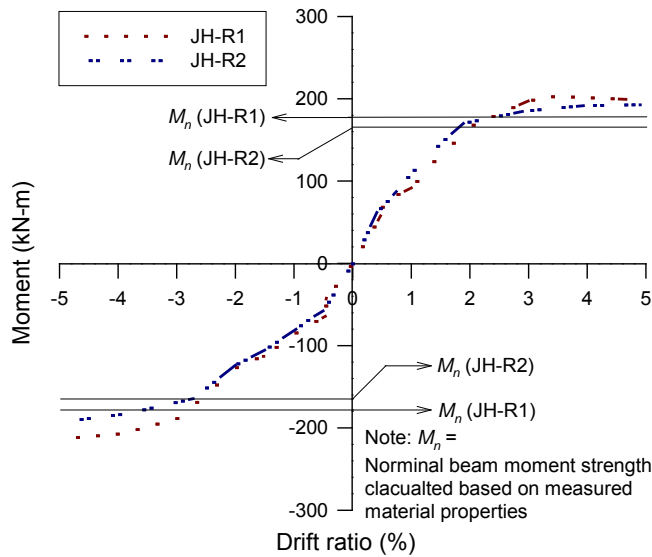


Figure 6.12. Backbone Envelopes of Lateral Load-Drift Relations
(Conversion: 1 kN-m = 8.85 kips-in.)

Table 6.7. Summary of Seismic Test Results of Moment and Drift

I.D.		M_n (kN-m)	M_{peak} (kN-m)	δ_{peak} (%)	M_y (kN-m)	δ_y (%)	$\delta_{0.75peak}$ (%)
JH-R1	+	178	203	3.5	153	1.9	N.A.
	-	178	213	4.9	160	2.4	N.A.
JH-R2	+	164	193	4.9	145	1.5	N.A.
	-	164	192	4.9	143	2.3	N.A.

M_n = nominal beam moment strength calculated based on measured material properties;

M_{peak} = measured peak beam moment;

δ_{peak} = drift ratio at M_{peak} ;

M_y = yield beam moment (assumed to be $0.75M_{peak}$ in this study);

δ_y = drift ratio at M_y ;

$\delta_{0.75peak}$ = drift ratio at 25% reduction from peak beam moment.

Conversion: 1 kN-m = 8.85 kips-in.

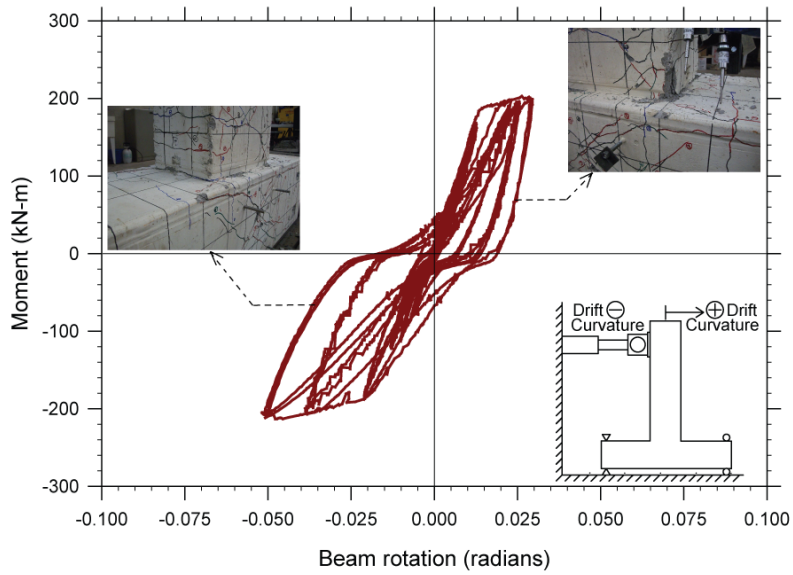
6.3.2 Beam Plastic Hinge Development

The rotational behavior of the beam around the beam-joint interface was monitored to investigate the development of a beam plastic hinge. In each specimen, four LVDTs were used to estimate beam rotations in the vicinity of the beam-joint interface as shown in Figures 6.7 and 6.8. One set of gauges (LVDT05 and LVDT08) monitored the relative displacement between the column face and the section one effective beam depth (387 mm; 15.25 in.) away from it, to where a plastic hinge region might extend. The beam rotation estimated with these gauges comprised both plastic hinge rotation and rigid beam-end rotation. Plastic hinge rotation was due to yielding of longitudinal beam bars in the beam plastic hinge zone. Rigid beam-end rotation was attributed to bond slip of reinforcing bars and opening of large flexural cracks at the beam-joint interface. The other set of gauges (LVDT06 and LVDT07) was installed between the section 50 mm (2 in.) away from the column face and the section approximately one effective beam depth (387 mm; 15.25 in.) away from the column face, so that it excluded beam rotations due to bond slip of beam bars. Beam rotations were

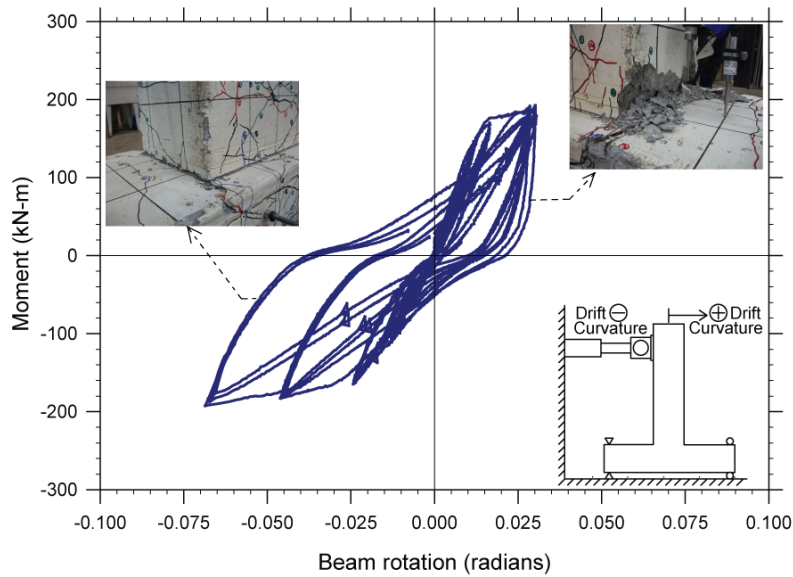
considered positive when the specimen was loaded in the positive direction (shown in Figure 6.8).

Figures 6.13(a) and 6.13(b) show the hysteretic response of beam moment vs. beam rotation in Specimens JH-R1 and JH-R2, in which the beam rotation was calculated by dividing the relative displacement estimated with LVDT05 and LVDT08 by the perpendicular distance between the two instruments. Both specimens reached a rotational ductility of more than two, showing similar beam rotations throughout testing in general. The beam rotation increased in an inelastic format from 2% drift ratio onward, while the beam moment did not increase significantly. This signified that beam hinging developed in the beam plastic hinge zone. The beam rotation was larger when the specimens were displaced in the negative direction, likely due to asymmetric locations of column end hinges with respect to the connection. Note that the hinge location was adjusted due to the pre-existing location of the anchor holes through which the subassembly was attached to the strong floor. Specimen JH-R2 exhibited slightly larger beam rotations under the negative loading, which was in accordance with the fact that slightly larger joint shear deformations were observed in Specimen JH-R1 (see Figures 6.14(a) vs. 6.14(b)).

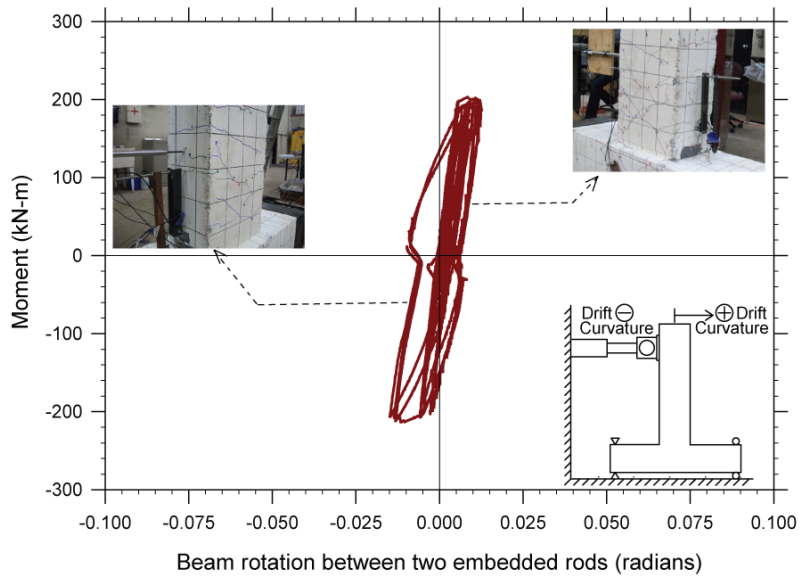
Figures 6.13(c) and 6.13(d) show the relationship of beam moment vs. beam rotation between the two rods embedded in the beam away from the beam-joint interface, in which the bond slip contribution was not included. The inelastic behavior and hysteretic energy dissipation were observed, indicating that the beam bar yielding also occurred relatively far from the interface (at least 50 mm (2 in.) away from the column).



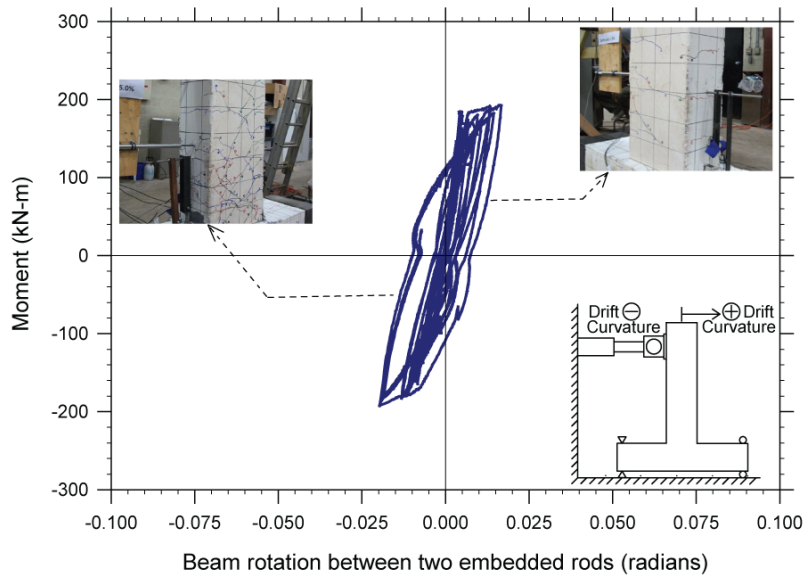
(a) JH-R1 (from LVDT05 and LVDT08)



(b) JH-R2 (from LVDT05 and LVDT08)

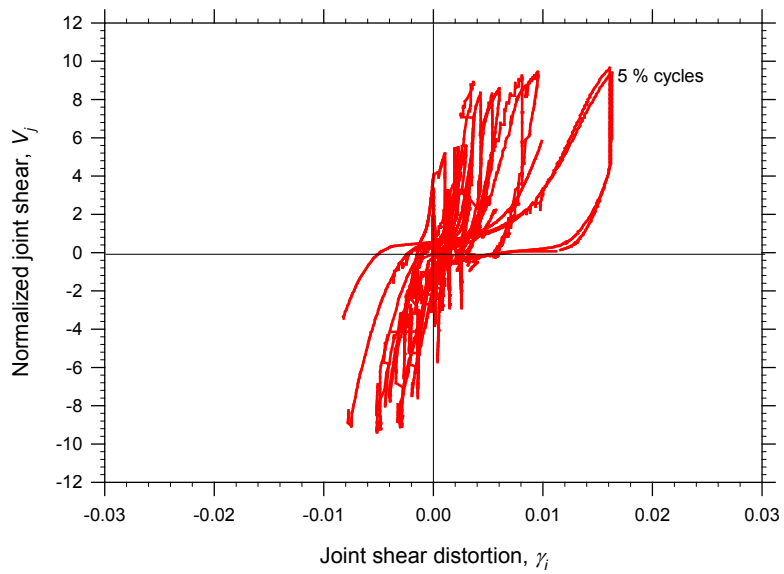


(c) JH-R1 (from LVDT06 and LVDT07)

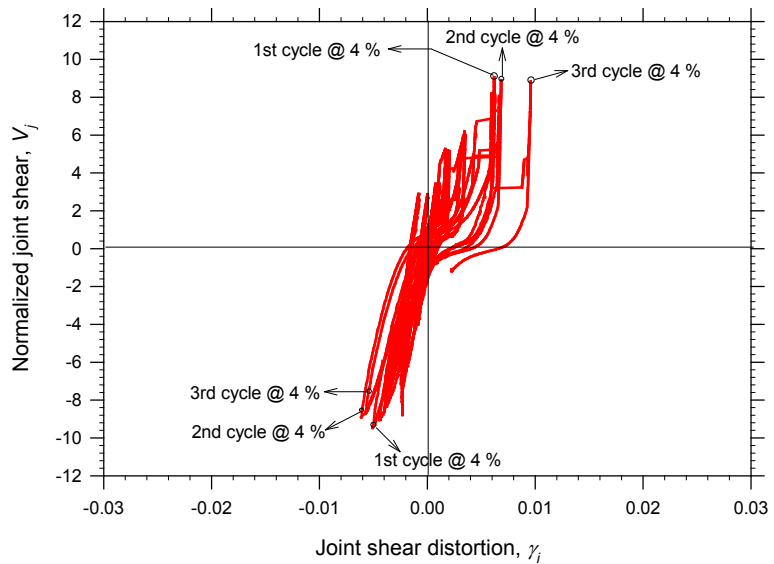


(d) JH-R2 (from LVDT06 and LVDT07)

Figure 6.13. Beam Moment vs. Beam Rotation Relationships for JH-R1 and JH-R2 Specimens (Conversion: 1 mm = 0.039 in.)



(a) JH-R1



(b) JH-R2

Figure 6.14. Normalized Joint Shear vs. Joint Shear Distortion Relationships for JH-R1 and JH-R2 Specimens

6.3.3 Limited Joint Shear Deformation

Joint shear cracks were diagonally inclined and intersected one another as shown in Figure 6.15, which was typical due to the reversed loading. Joint concrete damage was not significant by the end of testing in either specimen; little concrete spalling was observed at the end of testing. To monitor overall joint shear deformation, a set of two LVDTs crossing each other were installed at each face of the connection (see Figures 6.7 and 6.8). Using a total of four LVDTs on two sides of the connection in each specimen, angular changes were obtained at each measuring step, then the more reliable measurement of the two sides was taken as the joint shear deformation (γ_j), as detailed in Figure 6.14.

Figures 6.14(a) and 6.14(b) plot the hysteretic response of normalized joint shear vs. joint shear distortion in Specimens JH-R1 and JH-R2, respectively. Table 6.9 summarizes the maximum joint shear demands applied during testing ($V_{j,u-1}$ and $V_{j,u-2}$) and nominal joint shear strengths ($V_{j,n}$) of the specimens. The normalized joint shear (v_j) was determined as the measured joint shear force (V_j) divided by $(0.083\sqrt{f'_c}b_jh_c$ [MPa]; [psi]), where V_j was calculated as in Equation (6.1) along with the measured beam moment instead of the peak moment. The connections exhibited small joint shear deformations at a slow rate of increase up to about 3% drift ratio. However, the rate of increase in joint shear deformation (with respect to drift ratio) became relatively higher during 4% drift cycles without considerable increases in story shear, resulting in a joint shear deformation up to slightly less than 0.01 radians. However, the level of joint shear deformations exhibited in the specimens (roughly 0.016 radians maximum) was much lower than those in other connections found in the literature that failed by joint shear (Kang et al. [25]; Shin and LaFave [50]). The maximum normalized joint shear reached approximately 9.8 in the specimens, which was a little larger than the normalized joint shear demands (listed in Table 6.2) determined based on $f_{y,meas}$, but smaller than the γ factor (= 12) representing the ACI design joint shear capacity.

6.3.4 Performance Evaluation per ACI 374.1-05

The seismic performance of the tested connections was evaluated based on the acceptance criteria in ACI 374.1-05 (“Acceptance Criteria for Moment Frames Based on Structural Testing and Commentary”). To qualify as a moment frame having achieved satisfactory performance, the test results of the third complete cycle to a given drift ratio not less than 3.5% should meet the following criteria for both directions of response: (a) the peak force for a loading direction shall not be less than 75% of the maximum lateral resistance in the same loading direction; (b) the relative energy dissipation ratio shall not be less than 0.125; and (c) the stiffness around zero drift for a loading direction, which is estimated as the secant stiffness from a drift ratio of -0.35% to a drift ratio of 0.35%, shall not be less than 0.05 times the initial stiffness during the first cycle for the same direction. Note that the first cycle response should be essentially within the linear elastic range. Here, the relative energy dissipation ratio, β , is defined in Figure R2.4 of ACI 374.1-05, as the ratio of the area of the hysteresis loop for a given cycle to the area of the circumscribing parallelograms defined by the initial stiffness and the peak load during that cycle. The energy dissipation should be large enough to ensure adequate damping for weakening oscillations.

Table 6.8 summarizes the test results corresponding to the ACI 374.1-05 acceptance criteria. In this performance evaluation, the 4% drift cycles were used in a conservative sense, in that 3.5% drift cycles were not simulated in the tests; it should be noted that the response during the 5% drift cycles was similar to that for the 4% drift cycles. As shown in column [2] of Table 6.8, the drift ratio at the nominal strength ($\delta @ M_n$) was larger than the limiting initial drift ratio defined as $\Delta_a / \phi C_d$, which typically ranges between 0.3 and 0.5%. Here, Δ_a is the allowable story drift specified in the International Building Code, C_d is the displacement amplification factor, and ϕ is the strength reduction factor. However, considering that typical statically determinate test systems are much more flexible than real structures and that the tests were conducted up to the displacement ductility of about 2.5, the tests were judged valid for this evaluation.

By satisfying all acceptance criteria except for the limiting initial drift ratio, the performance of the two specimens was deemed satisfactory. In particular, the average strength degradation during the third cycle of the 4% drift in JH-R1 and JH-R2, respectively, was only 6 and 8%, with respect to the maximum load reached; this was similar during the 5% drift cycles. It is noted that JH-R2 with two layers of headed bars showed a higher energy dissipation ratio (β) as well as higher secant stiffness around zero drift (K_s/K) than JH-R1 for the 4% drift cycle (Table 6.8). It was likely because, at the beam-joint interface and inside the connection, the closer horizontal spacing accelerated the bond deterioration of JH-R1 where all the four beam bars were placed in a horizontal layer near the top or bottom beam surface, compared with JH-R2. Under inelastic bending reversals, the prying action of the headed beam bars appeared to slightly accelerate the loss of the concrete top or bottom cover. On the other hand, JH-R2 had no such problems with even the shorter (vertical) clear spacing between the bars. In both specimens, however, the side concrete cover was intact and no side-face blowout failure occurred throughout the testing. Overall, even after the bond deterioration, no severe concrete breakout was found (i.e., bearing capacity at the head was maintained) until 5% drift ratios in both specimens. Otherwise, the lateral load capacity of the connections would have dropped.

Table 6.8. Comparisons between Test Results and ACI 374.1-05 Acceptance Criteria

I.D.	[1]	Acceptance Criteria	JH-R1 (+)	JH-R1 (-)	JH-R2 (+)	JH-R2 (-)	
δ at M_n	[2]	$\leq 0.5\%$	2.2%	2.8%	1.7%	2.7%	
$\frac{M_{peak}}{M_n}$	[3]	≤ 1.25	1.14	1.2	1.17	1.17	
During third cycle of 4 % drift cycles	$\frac{M_{3rd}}{M_{peak}}$	[4]	≥ 0.75	0.95	0.92	0.91	0.93
	β	[5]	$\geq .125$	0.136		0.174	
	$\frac{K_s}{K}$	[6]	≥ 0.05	0.174	0.119	0.25	0.274

δ at M_n : Drift ratio (measured) at which M_n is reached;

M_n : Nominal beam moment strength (calculated based on measured material properties);

M_{peak} : Peak beam moment (measured);

M_{3rd} : Peak beam moment during 3rd cycle of 4 % drift (measured);

β : Relative energy dissipation ratio (ACI 374.1-05);

K_s (+): Secant stiffness for positive loading* from a drift ratio of -0.0035 to a drift ratio of +0.0035 (ACI 374.1-05);

K_s (-): Secant stiffness for negative loading** from a drift ratio of +0.0035 to a drift ratio of -0.0035 (ACI 374.1-05);

K : Initial stiffness for positive loading for first cycle (ACI 374.1-05);

K^{\wedge} : Initial stiffness for negative loading for first cycle (ACI 374.1-05);

Table 6.9. Comparison of Maximum Joint Shear Demands and Nominal Joint Shear Strengths

Specimen		JH-R1	JH-R2
V_{j,u_1} (kN; kips)		539; 121	524; 118
V_{j,u_2} (kN; kips)		440; 99	450; 101
$V_{j,n}$ (kN; kips)	ACI 318-08	Specified material properties	759; 171
		Measured material properties	795; 179
	ACI 352R-02	Specified material properties	631; 142
		Measured material properties	662; 149

$$V_{j,u_1} = \left(\frac{M_{peak}}{0.9d} - V_{c,peak} \right) \quad V_{j,u_2} = A_s f_{y,meas} - V_{c,peak}$$

$V_{c,peak}$ is the column shear force $\left(= \frac{F_{peak} \times l_b}{l_c} \right)$ at peak lateral force;

F_{peak} is the peak lateral force obtained from the test;

l_b is the distance between the loading point and beam-joint interface;

l_c is the column pin-to-pin story height;

d is the effective beam depth;

A_s is the area of tension longitudinal reinforcement;

$f_{y,meas}$ is the measured steel yield strength.

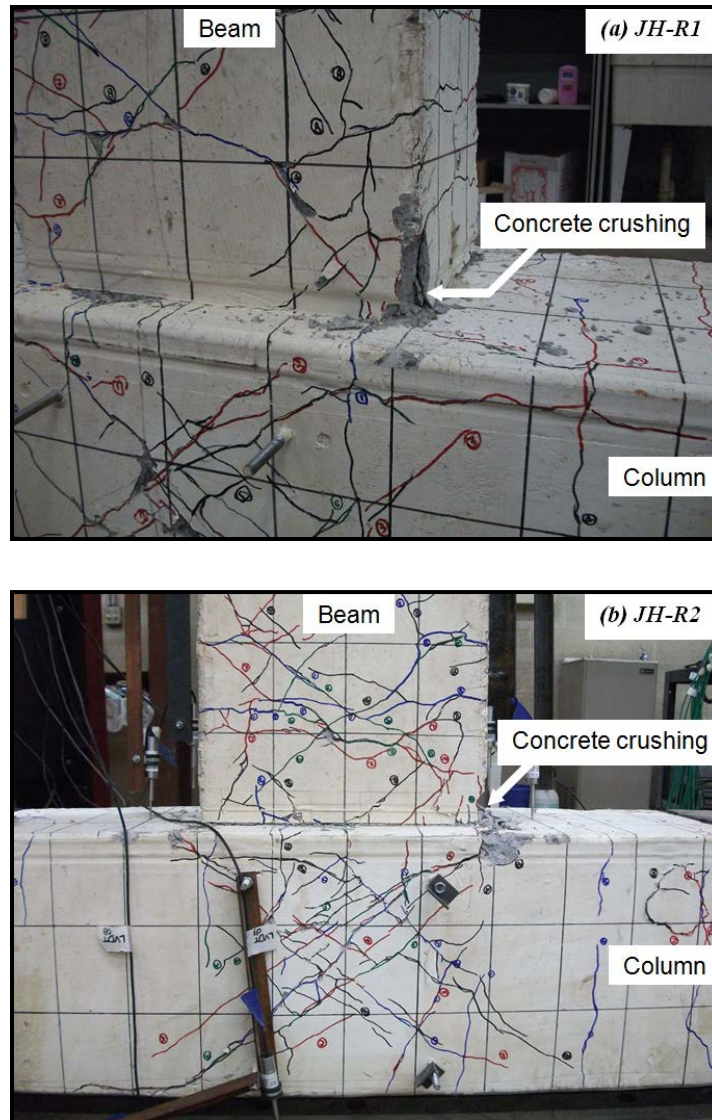


Figure 6.15. Crack Patterns at the End of Seismic Testing

6.4 SUMMARY

Given the strict requirements for clear headed bar spacing in ACI 318-08, this study discusses the applicability of the ACI 318 provisions to headed bars anchored in reinforced concrete beam-column connections that are part of earthquake-resistant structures. Two approximately 2/3-scale exterior beam-column subassemblies were tested under quasi-static cyclic lateral loading. The tests primarily explored the effect of

using (a) small clear spacings (less than $4d_b$) between headed bars, and (b) multiple layers of headed bars in the beam, on the seismic performance of exterior beam-column connections, both of which are currently prohibited by ACI 318-08. The seismic performance of the specimens was evaluated based on ACI 374.1-05 performance acceptance criteria in terms of overall strength and stiffness, beam plastic hinge development, strength degradation, energy dissipation, and pinching.

Based upon overall load displacement response, cracking patterns, beam rotation, joint shear deformation, and comparisons between nominal strength and measured peak moments, it was discovered that the beams exhibited ductile load displacement behavior with beam hinging adjacent to the beam-joint interface, with no unfavorable mechanisms accompanying notable strength drops. Similarly, both headed bar specimens complied with all performance criteria of ACI 374.1-05, except with respect to initial drift ratio. Both small headed bar spacing and multiple layered headed bars showed satisfactory performance under reversed cyclic lateral loading. Specimen JH-R2 with two layers of headed bars showed a higher energy, and a higher secant stiffness around zero, than JH-R1 with single layer headed bars for the 4% drift cycle. Overall, while both specimens achieved satisfactory performance with regard to the ACI 374.1-05 criteria, the specimen with two layers of headed bars at the top and bottom of the beam showed slightly superior behavior than the specimen with a single bar layer and a smaller horizontal spacing between headed bars. Based on the test results, it was concluded that the clear bar spacing of approximately $2d_b$ or the use of two bar layers fully meets the criteria for headed bars anchored in exterior beam-column connections (Kang et al. [51]).

This Page Is Intentionally Blank

7. CONCLUSION

In this final report, the analysis of experimental methodologies for steel congestion relief in concrete structures under monotonic and seismic loads has been discussed. The conclusions of the three studies conducted for the research are as follows:

- (1) The shear strength of the steel fiber-reinforced normalweight concrete beam is greater than that of the steel fiber-reinforced lightweight concrete beam. A lightweight concrete modification factor (λ) of 0.75 is applicable to use of fiber-reinforced beams.
- (2) The addition of steel fibers significantly improves the resistance to structural damage, strength at first diagonal cracking and ultimate shear strength. The steel fiber volume fractions (V_f) of both 0.5% and 0.75% increased the shear strength substantially.
- (3) The shear span-to-depth ratio adversely affects the shear strength of the lightweight fiber-reinforced beam. Thus, a term associated with the moment-shear interaction (e.g., a/d) should be included in the shear strength equation of SFRLC beams.
- (4) The beam with the combination of either ($V_f = 0.75\%$ and $a/d = 4$) or ($V_f = 0.5\%$ and $a/d = 3$) performed well, without any sign of brittle shear failure. This indicates that (upon further confirmation) the ACI 318 minimum requirement of $V_f = 0.75\%$ for shear resistance (§5.6.6.2(a)) could be reduced to improve concrete workability, if (a/d) of 2 to 3 is used.
- (5) Two design shear strength models for SFRLC beams with stirrups have been proposed based on available SFRC research and in accordance with the ACI 318-08 (§11.2) provision on the lightweight concrete modification factor ($\lambda = 0.75$). The results of the studies herein show that these models do correspond well to the existing data with reasonable precision and repeatability.
- (6) The predicted nonlinear behavior of and ultimate loads (denoted as P_n) of prestressed (conventional) concrete members correlated well with their experimental results. These results also indicate that the properties of SCC in prestressed members were not so different from those of conventional concrete.
- (7) The tested beam-column connections exhibited ductile load-displacement behavior with beam hinging fully developed adjacent to the beam-joint interface; no unfavorable mechanisms typically accompanying notable strength drops were found. These finding

were based on the overall load-displacement response, cracking pattern, beam rotation, joint shear deformation, and comparison between the nominal strength and measured peak moment of the beam.

(9) Both specimens of beam-column connections with headed bars conformed to all performance acceptance criteria set forth in ACI 374.1-05, except for the limiting initial drift ratio. Therefore, even with a small headed bar spacing (in JH-R1) or with multiple layers of headed bars (in JH-R2), the specimens showed satisfactory performance under reversed cyclic lateral loading. In particular, the strength degradation during the third cycle of the 4% drift ratio was only about 6% and 8% in JH-R1 and JH-R2 respectively, in comparison to the maximum load reached during the tests.

(10) Specimen JH-R2 with two layers of headed bars with heads touching each other showed a higher energy dissipation ratio as well as higher secant stiffness around zero drift than JH-R1 for the 4% drift cycle. This appeared to result from the closer horizontal spacing in JH-R1 slightly accelerating the bond deterioration of beam bars at the beam-joint interface and inside the connection, where all the four beam bars were placed in a horizontal layer near the top or bottom beam surface.

(11) Based on the test results, it was concluded that a clear bar spacing of approximately $2d_b$ or the use of two bar layers can be permitted for headed bars anchored in exterior RC beam-column connections subjected to earthquake-type loading.

While further, large-scale tests and analyses are recommended before broadly modifying any current code requirements, the studies herein show that the use of steel fibers, self-consolidating concrete (SCC) and headed bars can meet the necessary structural standards by producing significant improvements in steel congestion relief.

REFERENCES

1. Thompson, M. K.; Jirsa, J. O.; and Breen, J. E., "Behavior and Capacity of Headed Reinforcement," *ACI Structural Journal*, 103(4), July-Aug. 2006, pp. 522-530.
2. Lehman, D. E.; Gookin, S. E.; Nacamuli, A. M.; and Moehle, J. P., "Repair of Earthquake-Damaged Bridge Columns," *ACI Structural Journal*, 98(2), Mar.-Apr. 2001, pp. 233-242.
3. Yashinsky, M., and Karshenas, M. J., "Fundamentals of Seismic Protection for Bridges," Earthquake Engineering Research Institute, MNO-9, 2003.
4. Balaguru, P., and Ramakrishnan, V., "Properties of Lightweight Fiber Reinforced Concrete," *Fiber Reinforced Concrete Properties and Applications*, SP-105, American Concrete Institute, Detroit, Michigan, Dec. 1987, pp. 305-322.
5. Balaguru, P., and Dipsia, M. G., "Properties of Fiber Reinforced High-Strength Semilightweight Concrete," *ACI Structural Journal*, 90(5), Sep.-Oct. 1993, pp. 399-405.
6. Balaguru, P., and Foden, A., "Properties of Fiber Reinforced Structural Lightweight Concrete," *ACI Structural Journal*, 93(1), Jan.-Feb. 1996, pp. 62-78.
7. Swamy, R. N., and Jojagha, A. H., "Workability of Steel Fibre Reinforced Lightweight Aggregate Concrete," *International Journal of Cement Composites and Lightweight Concrete*, 4(2), May 1982, pp. 103-109.
8. Swamy, R. N., and Jojagha, A. H., "Impact Resistance of Steel Fibre Reinforced Lightweight Concrete," *International Journal of Cement Composites and Lightweight Concrete*, 4(4), Nov. 1982, pp. 209-220.
9. Kayali, O.; Haque, M. N.; and Zhu, B., "Drying Shrinkage of Fibre-Reinforced Lightweight Aggregate Concrete Containing Fly Ash," *Cement and Concrete Research*, 29(11), Nov. 1999, pp. 1835-1840.
10. Swamy, R. N.; Jones, R.; and Chiam, A. T. P., "Influence of Steel Fibers on the Shear Resistance of Lightweight Concrete I-Beams," *ACI Structural Journal*, 90(1), Jan.-Feb. 1993, pp. 103-114.
11. Theodorakopoulos, D. D., and Swamy, R. N., "Contribution of Steel Fibers to the Strength Characteristics of Lightweight Concrete Slab-Column Connections Failing

- in Punching Shear," *ACI Structural Journal*, 90(4), July-Aug. 1993, pp. 342-355.
12. Balaguru, P., and Dipsia, M., "Properties of fiber reinforced high-strength semilightweight concrete," *ACI Materials Journal*, 90(5), Sep-Oct. 1993, pp. 399-405.
 13. ASTM, "Concrete Mineral Aggregate," American Society for Testing Materials, West Conshohocken, PA, 1993.
 14. ASTM, "American Society for Testing and Materials Annual Book of ASTM Standards," V. 04.09, American Society for Testing Materials, West Conshohocken, PA, 2008.
 15. Higashiyama, H., and Banthia, N., "Correlating Flexural and Shear Toughness of Lightweight Fiber-Reinforced Concrete," *ACI Materials Journal*, 105(3), May-June 2008, pp. 251-257.
 16. ACI Committee 544, "Measurement of Properties of Fibre Reinforced Concrete," *ACI Journal, Proceedings*, 75(7), July 1978, pp. 283-290.
 17. ACI Committee 318, "Building Code Requirements for Structural Concrete (ACI 318-08) and Commentary," American Concrete Institute, Farmington Hills, MI, 2008, 473 pp.
 18. ASTM A970/A970M-07, "Standard Specification for Headed Steel Bars for Concrete Reinforcement," ASTM International, West Conshohocken, PA, 2007, 8 pp.
 19. DeVries, R. A.; Jirsa, J. O.; and Bashandy, T., "Anchorage Capacity in Concrete of Headed Reinforcement with Shallow Embedments," *ACI Structural Journal*, 96(5), Sept.-Oct. 1999, pp. 728-737.
 20. Bashandy, T. R., "Application of Headed Bars in Concrete Members", Ph.D. Dissertation, University of Texas at Austin, 1996
 21. Wright, J. L., and McCabe, S. L., "The Development Length and Anchorage Behavior of Headed Reinforcing Bars," SM Report No. 44, Structural Engineering and Engineering Materials, University of Kansas Center for Research, Lawrence, KS, Sept. 1997, 147 pp.
 22. Wallace, J. W.; McConnell, S. W.; Gupta, P.; and Cote, P. A., "Use of Headed Reinforcement in Beam-Column Joints Subjected to Earthquake Loads," *ACI Structural Journal*, 95(5), Sept.-Oct. 1998, pp. 590-606.
 23. Joint ACI-ASCE Committee 352, "Recommendations for Design of Beam-Column

- Connections in Monolithic Reinforced Concrete Structures (ACI 352R-02),” American Concrete Institute, Farmington Hills, MI, 2002, 37 pp.
24. ASTM A970/A970M-98, “Standard Specification for Headed Steel Bars for Concrete Reinforcement,” ASTM International, West Conshohocken, PA, 1998, 7 pp.
 25. Kang, T. H.-K.; Shin, M.; Mitra, N.; and Bonacci, J. F., “Seismic Design of Reinforced Beam-Column Joints with Headed Bars,” *ACI Structural Journal*, 106(6), Nov.-Dec. 2009, pp. 868-877.
 26. Chun, S. C.; Lee, S. H.; Kang, T. H.-K.; Oh, B.; and Wallace, J. W., “Mechanical Anchorage in Exterior Beam-Column Joints Subjected to Cyclic Loading,” *ACI Structural Journal*, 104(1), Jan.-Feb. 2007, pp. 102-113.
 27. Lee, H.-J., and Yu, S.-Y., “Cyclic Response of Exterior Beam-Column Joints with Different Anchorage Methods,” *ACI Structural Journal*, 106(3), May- June 2009, pp. 329-339.
 28. Kang, T. H.-K.; Ha, S.-S.; and Choi, D.-U., “Bar Pullout Tests and Seismic Tests of Small-Headed Bars in Beam-Column Joints,” *ACI Structural Journal*, 107(1), Jan.-Feb. 2010, pp. 32-42.
 29. Matsushima, M.; Kuramoto, H.; Maeda, M.; Shindo, K.; and Ozone, S., “Test on Corner Beam-Column Joint under Tri-Axial Loadings,” *Proceedings of the Architectural Institute of Japan*, Sept. 2000, pp. 861-863. (in Japanese)
 30. Ishida, Y.; Fujiwara, A.; Adachi, T.; Matsui, T.; and Kuramoto, H., “Structural Performance of Exterior Beam-Column Joint with Wide Width Beam Using Headed Bars,” *Proceedings of the Architectural Institute of Japan*, Aug. 2007, pp. 657-660. (in Japanese)
 31. Narayanan, R., and Darwish, I. Y. S., “Use of Steel Fibers as Shear Reinforcement,” *ACI Structural Journal*, 84(3), May-June 1987, pp. 216-227.
 32. Kwak, Y.-K.; Eberhard, M. O.; Kim, W.-S.; and Kim, J., “Shear Strength of Steel Fiber-Reinforced Concrete Beams without stirrups,” *ACI Structural Journal*, 99(4), July-Aug. 2002, pp. 530-538.
 33. Khuntia, M.; Stojadinovic, B.; and Goel, S. C., “Shear Strength of Normal and High-Strength Fiber Reinforced Concrete Beams without Stirrups,” *ACI Structural Journal*, 96(2), Mar.-Apr. 1999, pp. 282-289.

34. Shin, S.-W.; Oh, J.-K.; and Ghosh, S. K., "Shear Behavior of Laboratory-Sized High-Strength Concrete Beams Reinforced with Bars and Steel Fibers," *Fiber Reinforced Concrete Developments and Innovations*, SP-142, American Concrete Institute, Farmington Hills, MI, Jan. 1994, pp. 181-200.
35. Imam, M.; Vandewalle, L.; Mortelmans, F.; and Van Gemert. D., "Shear Domain of Fibre Reinforced High-Strength Concrete Beams," *Engineering Structures*, 19(9), Sept. 1997, pp. 738-747.
36. Ashour, S. A.; Hassanain, G. S.; and Wafa, F. F., "Shear Behavior of High-Strength Fiber-Reinforced Concrete Beams," *ACI Structural Journal*, 89(2), Mar.-Apr. 1992, pp. 176-184.
37. Choi, K.-K.; Park, H.-G.; and Wight, J. K., "Shear Strength of Steel Fiber-Reinforced Concrete Beams with Web Reinforcement," *ACI Structural Journal*, 104(1), Jan.-Feb. 2007, pp. 12-22.
38. Swamy, R. N.; Mangat, P. S.; and Rao, C. V. S. K., "The Mechanics of Fiber Reinforcement of Cement Matrices," *Fiber Reinforce Concrete*, SP-44, American Concrete Institute, Farmington Hills, MI, Jan. 1974, pp. 1-28.
39. Sharma, A. K., "Shear Strength of Steel Fiber Reinforced Concrete Beams," *ACI Journal, Proceedings*, 83(4), July-Aug. 1986, pp. 624-628.
40. Li, V.; Ward, R.; and Hamza, A. M., "Steel Synthetic Fibers as Shear Reinforcement," *ACI Materials Journal*, 89(5), Sept.-Oct. 1992, pp. 499-508.
41. MacGregor, J. G.; Sozen, M. A.; and Siess, C. P., "Strength and Behavior of Prestressed Concrete Beams with Web Reinforcement," *University of Illinois Civil Engineering Studies, Structural Research Series 210*, Urbana, IL, Aug. 1960.
42. Naaman, A. E., and Reinhardt, H. W., "High Performance Fiber Reinforced Cement Composites HPFRCC-4: International RILEM Workshop Ann Arbor, Michigan, June 16-18, 2003," *Materials and Structures/Materiaux et Constructions*, 36(264), Dec. 2003, pp. 710-712.
43. Kang, T. H.-K.; Kim, W.; Kwak, Y.-K.; and Hong, S.-G., "Shear Testing of Steel Fiber-Reinforced Lightweight Concrete Beams without Web Reinforcement," *ACI Structural Journal*, 108(5), Sept.-Oct. 2011, pp. 553-561.
44. Hwang, S.-D.; Khayat, K.H.; and Bonneau, O., "Performance-Based Specifications

- of Self-Consolidating Concrete Used in Structural Applications,” *ACI Materials Journal*, 103(2), Mar.-Apr. 2006, pp. 121-129.
45. Kim, W.; Piyawat, K.; Ramseyer, C.; and Kang, T. H.-K., “Experimental and Numerical Simulations of Prestressed Self-Consolidating-Concrete Structures Subjected to Non-Linear Deformations,” *International Journal of Theoretical and Applied Multiscale Mechanics*, 1(4), Dec. 2010, pp. 319-338.
46. AASHTO, “LRFD Bridge Design Specifications,” American Association of State Highway and Transportation Officials, Washington, DC, 2007.
47. Mazzoni, S.; McKenna, F.; Scott, M. H.; and Fenves, G.L., “Open System for Earthquake Engineering Simulation (OpenSees) User Command-Language Manual – Version 1.7.3,” University of California, Berkeley, CA, 2007.
48. ACI Committee 374, “Acceptance Criteria for Moment Frames Based on Structural Testing and Commentary (ACI 374.1-05),” American Concrete Institute, Farmington Hills, MI, 2005, 9 pp.
49. Meinheit, D. F., and Jirsa, J. O., “Shear Strength of R/C Beam-Column Connections,” *Journal of Structural Division, ASCE*, 107(11), Nov. 1981, pp. 2227-2244.
50. Shin, M., and LaFave, J. M., “Seismic Performance of Reinforced Concrete Eccentric Beam-Column Connections with Floor Slabs,” *ACI Structural Journal*, 101(3), May-June 2004, pp. 403-412.
51. Kang, T. H.-K.; Kim, W.; and Shin, M., “Cyclic Testing for Seismic Design Guide of Beam-Column Joints with Closely-Spaced Headed Bars,” *Journal of Earthquake Engineering*, 16(2), Feb. 2012, pp. 211-230.